EXTENDING THE APPLICATION RANGE OF Z-PINS IN COMPOSITES

By

Mudan Chen

Department of Aerospace Engineering

University of Bristol

This dissertation is submitted for the degree of Doctor of Philosophy

April 2023

Word count: 31998

ABSTRACT

This dissertation expands the scope of Z-pins' application in composites by investigating their unconventional uses. The mechanical behaviour, electrical performances, and magnetic properties of Z-pinned laminates are examined, respectively.

In addition to exploring the well-established fracture toughness and in-plane properties of Z-pinned flat panels, the study experimentally investigates the through-thickness tensile strength of Z-pinned curved laminates under four-point bending. The effects of Z-pins at different volume fractions on the strength and failure mode are analysed, comparing the results to unpinned specimens. High-fidelity finite element models of both unpinned and carbon-fiber Z-pinned specimens are developed in Abaqus/Explicit to provide insights into the experimental observations and different failure mechanisms introduced by Z-pins.

Moreover, the study investigates the electrical (and consequential thermal) behaviour of Z-pinned laminates under localised in-plane and through-thickness fault currents. The effects of Z-pin material and volume fraction on the current conducting path and temperature are discussed through experiments and micro-structural observations.

Furthermore, traditional fibre-reinforced composites are magnetically inert, which limits their potential applications in certain fields. Therefore, the study explores the influence of carbon-fibre and ferromagnetic Z-pins on the global magnetic properties of composites. The effects of pin material, misalignment, and volume fraction on the in-plane and through-thickness magnetic properties are experimentally studied, with further insights provided by numerical modelling conducted in COMSOL.

In conclusion, this dissertation contributes to the wider understanding and utilisation of Z-pins in composites, potentially enabling the development of novel and practical applications.

PUBLICATIONS

The author would like to acknowledge the following produced publications and attended conferences during the PhD period. Notably, Section 6 reuses work published in [1a], Section 3 and 4 contain some results from [3a] and [2a] respectively.

Journal Publications

[1a] M. Chen, B. Zhang, S. Friedemann, G. Allegri, S.R. Hallett, Effects of Ferromagnetic & Carbon-Fibre Z-Pins on the Magnetic Properties of Composites, Composites Science and Technology. (2021) 108749.

Conferences

[2a] M. Chen, B. Zhang, A.R. Melro, L.F. Varandas, G. Allegri, S.R. Hallett, Numerical investigation into the failure mechanisms of Z-pinned curved composite laminates under four-point bending, the 15th World Congress on Computational Mechanics (WCCM), August 2022, abstract and presentation.

[3a] M. Chen, B. Zhang, X. Xu, G. Allegri, S.R. Hallett, Experimental study on the mechanical behaviour of carbon-fibre Z-pin reinforced curved composite laminates under four-point bending, the 20th European Conference on Composite Materials (ECCM), June 2022, full paper and presentation.

[4a] M. Chen, B. Zhang, S. Friedemann, G. Allegri, S.R. Hallett, Effects of Ferromagnetic & Carbon-fibre Z-pins on the magnetic properties of composites, Bristol Composites Institute Postgraduate Research and Training Showcase, April 2021, poster and presentation.

ACKNOWLEDGEMENTS

The period of my doctoral studies was a precious and unforgettable experience in my life, albeit challenging due to the impact of COVID-19. The lockdown and feelings of homesickness presented several difficulties. However, amidst these challenges, I received tremendous support from various sources.

First and foremost, I would like to express my sincerest gratitude to my supervisors, particularly to Professor Stephen Hallett, who always provided me with clear guidance on my research and was incredibly helpful and supportive. I am also grateful to Dr. Bing Zhang for providing me with detailed instructions. Prof. Giuliano Allegri offered many valuable ideas, and Dr. Sven Friedemann made a significant contribution to part of my research. It has been a great honor for me to work with this esteemed group.

I would like to acknowledge the CDT for their support throughout my studies. Thanks to Prof. Paul Weaver, who accepted my PhD application, cheered me up when I was sick, and offered me a funding extension to finish the study. Thanks to CDT manager Sarah Hallworth, who witnessed my start and engaged in many important things in my PhD. I am also thankful for my amazing CDT 18 cohorts.

The lab technicians played an indispensable role in the completion of my work. Dr. Yusuf Mahadik, Katie Smith, Ian Chorley, Richard Van Gelder, Peter Whereat, Andy Brown, and others provided invaluable assistance to me. Dr. António R. Melro, Dr. Xiaodong Xu, Dr. Qicheng Zhang, Dr. Xiaochuan Sun, Dr. Luís F. Varandas, and Dr. Lihong Xie were also instrumental in helping me overcome challenges.

I would like to express my love and gratitude to my family. To my parents for giving me life and raising me, to my brother for his encouragement and for accompanying our family while I was abroad, to my grandmother for looking after me since I was born, and to my grandfather for giving me my name. I am also grateful to my partner, who always trusts and encourages me. His companionship and support are essential to my studies.

DECLARATION

I declare that the work in this dissertation was carried out in accordance with the requirements of the University's Regulations and Code of Practice for Research Degree Programmes and that it has not been submitted for any other academic award. Except where indicated by specific reference in the text, the work is the candidate's own work. Work done in collaboration with, or with the assistance of, others, is indicated as such. Any views expressed in the dissertation are those of the author.

Signed: 

Date: 20/04/2023

TABLE OF CONTENTS

LIST OF TABLES

LIST OF FIGURES

List of Abbreviations and Acronyms

CFRP	Carbon-fibre reinforced polymer
DCB	Double cantilever beam
ENF	End-notched flexure
FE	Finite element
FEA	Finite element analysis
FRP	Fibre reinforced polymer
QI	Quasi-isotropic
TTR	Through-thickness reinforcement
TTS	Through-thickness tensile strength
UAZ	Ultrasonically assisted Z-fiber
UD	Unidirectional

LIST OF APPENDICES

1 INTRODUCTION

1.1 Overview

Carbon fiber reinforced polymer (CFRP) composites, owing to their high strength, stiffness, and low density, are increasingly being used to create lightweight structures. Thanks to significant advancements in the understanding of fundamental mechanics and manufacturing processes, CFRP composites are now widely used in various fields, such as aviation, automotive and naval engineering, energy, and sports equipment. In modern civil passenger aircraft, advanced composites components account for 50% of the total structural weight in both the Airbus A350 XWB and Boeing B787 Dreamliner [1].

However, laminated fibre reinforced polymer composites often exhibit poor delamination resistance, primarily because of the low fracture toughness and strength of the polymer matrix phase, fibre-matrix interface, and the absence of through-thickness fibres. Delamination, which is the formation of interlaminar cracks, is a major failure mode that can result in a loss of component stiffness and strength, and potentially cause catastrophic failure.

To address this issue, numerous methods have been developed to improve the interlaminar properties of laminated composite, such as toughened resins, nanoparticle additions, interleaving, and surface treatment of fibres [2,3]. The through-thickness reinforcement (TTR) technologies, including stitching [4], 3D weaving [5], tufting [6], and Z-pinning [2,3] typically provide greater improvements to delamination resistance than other toughening methods.

Z-pinning is the primary technique used in prepreg constructions, involving inserting small-diameter rods or tubes through the thickness of the composites, either perpendicular or at an angle to the plane of the laminate. The pins act as interlayer reinforcements to prevent delamination propagation by forming a large bridging zone to dissipate the energy [2,3]. Other techniques above are used for textile laminates. Before the resin infusion, reinforcement across the thickness of dry fabrics is required [4,6].

Although the use of Z-pins in composites has been extensively studied experimentally and numerically [2,3,7,8], most of the research has focused on the interlaminar fracture toughness and in-plane properties of Z-pinned flat laminates. Only one published work [9] has reported the experimental study on the curved beam strength (CBS) of L-shape beams with Z-pins, and no relevant modelling work has been found, leaving a considerable knowledge gap regarding the effect of Z-pins on the through-thickness laminate properties.

In addition to their mechanical benefits, there is a growing interest in exploring the multifunctionality of Z-pins. Limited research [10–19] has been conducted on monitoring delamination, and enhancing electrical and thermal conductivities of Z-pinned laminates. However, much more work is required to characterise other performances of Z-pinned laminates and investigate their potential applications in other fields.

For instance, the high impedance of CFRP poses challenges in detecting fault currents within a CFRP structure. The presence of fault currents also results in Joule heating, which degrades the matrix and ultimately leads to structural failure. Therefore, it is crucial to enhance the electrical conductivity of CFRP through the

implementation of Z-pins and develop a comprehensive understanding of the internal current paths. Furthermore, CFRP composites exhibit magnetic inertness, which proves to be a significant drawback in various applications, compared to metals. To overcome this limitation, the utilisation of Z-pins becomes advantageous. Overall, by improving the electrical conductivity of CFRP with Z-pins and addressing the magnetic limitations of these composites, their performance can be enhanced, enabling broader application potential.

1.2 Research objectives

The aim of this PhD thesis is to explore a wider range of Z-pin applications in composites, with a particular focus on their unconventional uses. The study investigates different disciplines, including the mechanical behaviour, electrical, and magnetic properties of Z-pinned laminates mentioned above. The objectives of the research are:

- To experimentally investigate the through-thickness tensile strength (TTS) of Z-pinned laminates, using curved beam specimens under four-point bending with traditional carbon-fibre composites pins and metal (with surface coating) pins and analyse the effects of Z-pin material and volume fraction on the failure mode and strength. In contrast to the extensively studied ability of Z-pins to resist damage propagation and improve the interlaminar fracture toughness of flat laminates, this research aims to investigate whether Z-pins are effective in delaying the initiation of interlaminae cracks of a curved beam.
- To develop high-fidelity finite element (FE) models of unpinned and carbon-fibre Z-pinned curved specimens under four-point bending in Abaqus/Explicit to provide insights into the different failure mechanisms introduced by Z-pins.
- To investigate the electrical (and consequential thermal) behaviour of Z-pinned laminates under fault currents and analyse the influence of Z-pin

material (carbon-fibre and copper) and volume content on the current conducting path and temperature.

- To experimentally study the influence of traditional carbon-fibre composites pins and ferromagnetic pins on the global in-plane and through-thickness magnetic properties of composite laminates, and analyse the effects of pin misalignment and volume fraction with FE modelling in COMSOL.

This study aims to expand the scope of Z-pins' application in composites and contributes to the broader understanding and utilisation of this reinforcement technique. The findings of this study could enable the development of novel and practical applications of Z-pins in composites, addressing the limitations of traditional fibre-reinforced composites and opening new avenues for their use in various fields.

1.3 Thesis Structure

According to the research objectives set above, the thesis structure has been set out as follows:

- Chapter 2 presents a comprehensive literature review on Z-pinning, including the manufacturing process and induced microstructures, experimental and modeling works on the mechanical behaviour and multifunctional explorations of Z-pinned composites.
- Chapter 3 shows the experimental study of Z-pinned curved laminates under four-point bending, including the specimen design and manufacturing, test set-up, and results discussion.
- Chapter 4 describes the conducted numerical study for a better understanding of experimental phenomena observed in Chapter 3, consisting of the FE model set-up, definition, and result analysis.
- Chapter 5 investigates the electrical and resulting thermal response of unpinned and Z-pinned laminates under the in-plane and through-thickness

fault current conditions experimentally, with the current path created by Z-pins examined in detail.

- Chapter 6 characterises the global magnetic properties of unpinned and Z-pinned laminates experimentally and numerically in the in-plane and through-thickness directions respectively, with two pin materials used at two volume fractions.
- Chapter 7 draws conclusions from this study and offers suggestions for future works.

2 LITERATURE REVIEW

2.1 Z-pinning technology

2.1.1 Manufacturing of Z-pinned laminate

The earliest TTR technique similar to Z-pinning was introduced by Huang et al. [20] in the late 1970s. Z-pins were patented as 'Z-Fiber' by US-based company Foster-Miller Inc. in the 1990s [21,22].

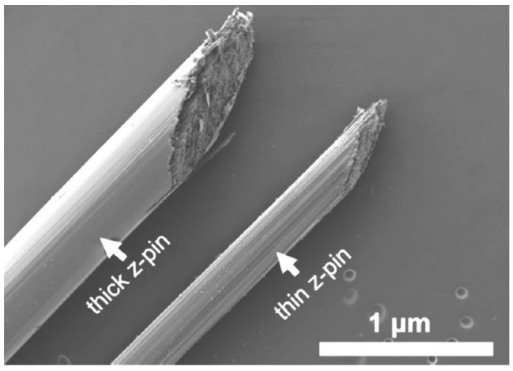

Figure 2.1: Images of thin (0.28 mm diameter) and thick (0.51 mm diameter) Z-pins made of carbon-fibre composite rod. From Mouritz [3].

Z-pins are very small metal or fiber rods, typically 0.1 to 1.0 mm in diameter. Unidirectional (UD) carbon fiber-polymer rods and high-strength alloy filaments are the most often used Z-pins, although practically any high-performance material

can be used. The widely explored Z-pins have diameters of 0.28 mm and 0.51 mm, with the areal densities ranging from 0.5% to 4% [2,3]. Typical carbon-fibre Z-pins are shown in Figure 2.1.

Inserting z-pins using the ultrasonically assisted Z-fiber (UAZ) technique is the most widely adopted approach [3]. Prepreg-based laminates are best suited for the UAZ process, which inserts Z-pins using ultrasonic vibrations before curing. The procedure begins by covering the prepreg laminate with a compressible polymer foam carrier. A grid pattern of Z-pins is arranged at the desired spacing within the foam carrier. High-frequency ultrasonic vibrations produced by a tool are transmitted to the foam carrier, causing it to collapse and pressing the Z-pins into the laminate, as illustrated in Figure 2.2(a). Z-pins are gradually introduced until they fully penetrate the laminate. Finally, the foam carrier and any extra protruding pin ends are machined off.

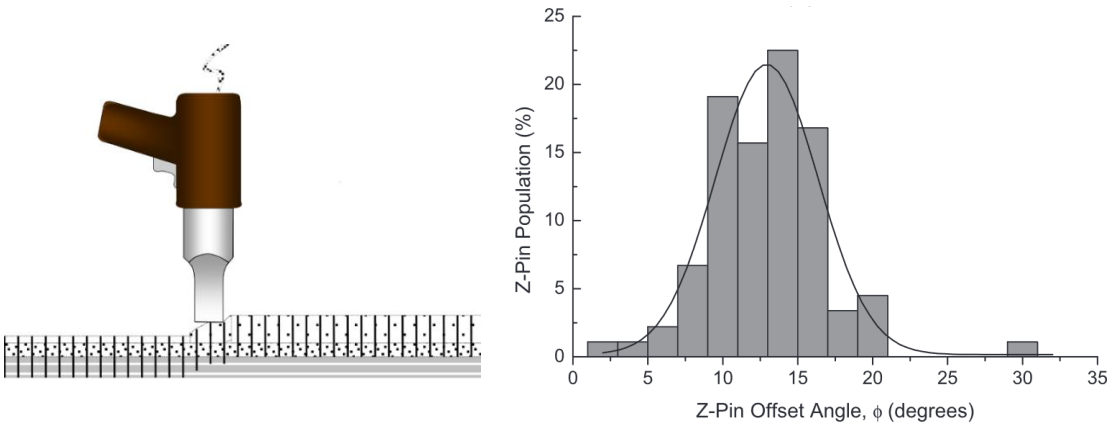

(a) (b)

Figure 2.2: (a) Schematic of one stage in the UAZ process, (b) measured distribution of Z-pin angles with UAZ method (pin diameter = 0.28 mm). From Mouritz [3].

However, the UAZ approach can cause the pins severely misaligned, up to 20-30° in the through-thickness direction, as shown in Figure 2.2(b). To optimize the Z-pinning process, various methods have been proposed.

Choi et al. created an automated Z-pinning technique to conduct the pinning during the curing process in an autoclave [23]. The upper fixture was equipped with

multiple guide pins installed perpendicular to its lower surface. Meanwhile, the lower fixture was machined with numerous holes that serve as placement locations for the Z-pins to be inserted into the laminates. The increased temperature reduces the viscosity of the prepreg resin. The pressure pushes the upper fixture towards the lower fixture, as illustrated in Figure 2.3(a). The Z-pins were guided much more effectively compared with the UAZ process. It also allows for the pinning of more complicated surfaces.

The vibrating hollow needle technique with a Z-pin inside was employed by Vazquez et al. [24] as shown in Figure 2.3(b). Although effective, this approach was unable to use Z-pins with small diameters, as it is currently limited to relatively large Z-pin diameters of 0.7 mm.

Through using a corresponding tool containing metallic rods to drive the pins into the laminates, an economical Z-pinning technology for dry textiles was created by Knaupp and Scharr as illustrated in Figure 2.3(c) [25]. The chamfered tips could be sheared off with this method.

A more automated method is illustrated in a UK patent [26] for inserting reinforcement rods into holes provided in composite structures using a rod insertion device. The rod is supplied with a feeding system, and the tension in the rod can be released between the supply system and the inserting device.

A manual insertion process with pre-drilled holes is frequently used for lab-based research [27–29]. The prepreg stack is placed on a heating pad to soften the laminate. A fine needle is used to make a hole, followed by manual insertion of the Z-pin into the drilled hole. Although this method is labour-intensive, it results in a much better pinning quality with small misalignment angles, as shown in Figure 2.3(d). Gong et al. [29] validated that the in-plane performance (tension and compression) loss due to Z-pinning has been significantly reduced compared to that of the UAZ method.

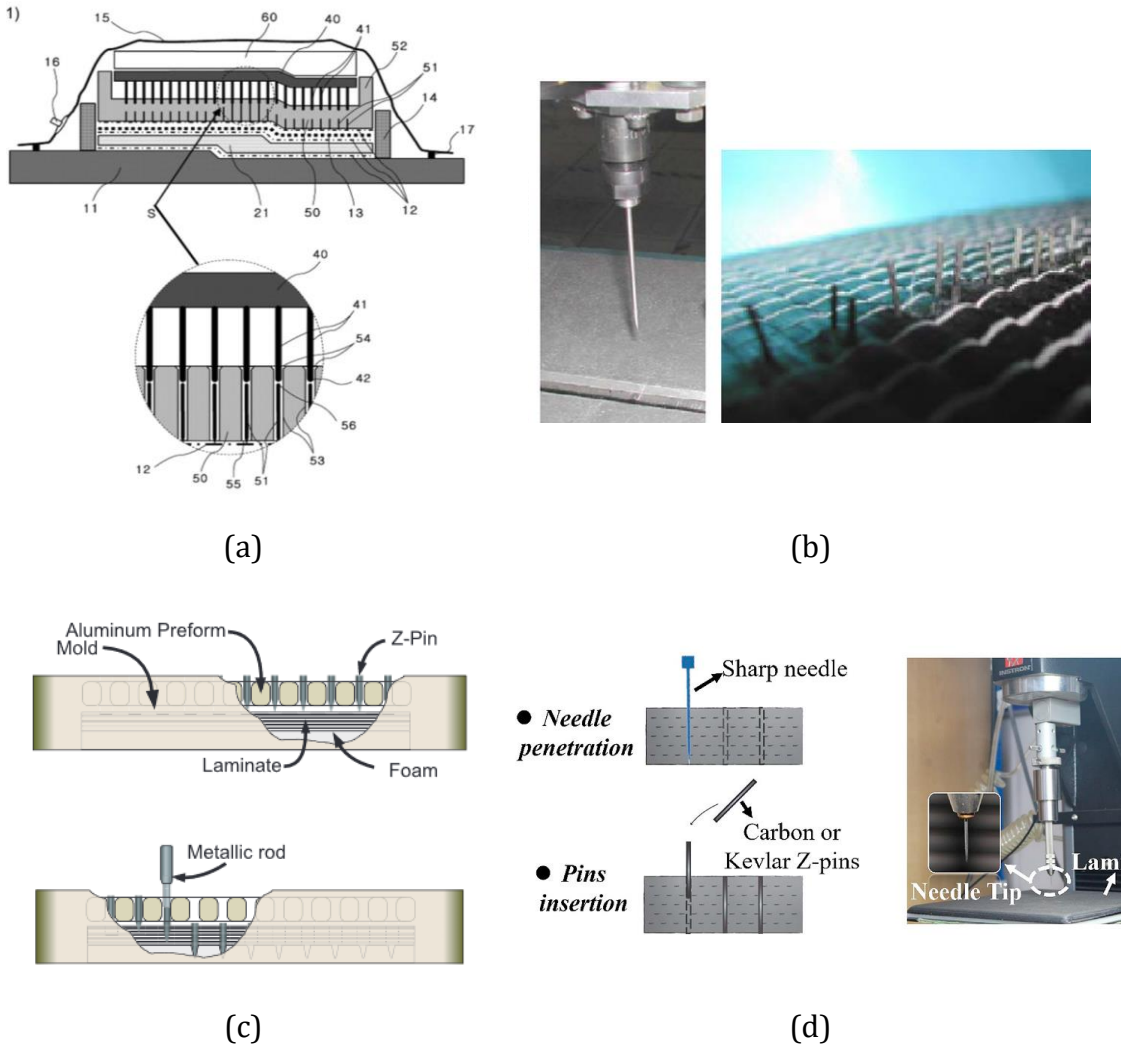

Figure 2.3: Z-pinning methods (a) from Choi et al. [23], (b) from Vazquez et al. [24], (c) from Knaupp and Scharr [25], (d) from Gong et al. [29].

2.1.2 Microstructure of Z-pinned laminate

When adding Z-pins, microstructural features/disruptions are introduced to the composite laminates, such as the waviness, crimp and breakage of fibres, resin-rich zones, and local swelling [2,3].

In localised regions around a Z-pin, the fibres are pushed aside by the pin, creating fiber waviness and forming a resin-rich zone that is eye-shaped, as shown in Figure 2.4(a). It has been demonstrated that the amount of in-plane fibre waviness is directly related to the Z-pin diameter and the pinning density [30]. The resin pockets formed by Z-pinning change the stress distribution and the Z-pin/laminate

adhesion, making the composite more prone to crack initiation from these areas. When the pin density is high (2% or greater) [30,31], it causes the resin pockets to connect and form a resin channel (Figure 2.4(b)).

Z-pin insertion may also lead to crimping of in-plane fibers through the thickness, as shown in Figure 2.4(c). The fibres under the Z-pins are pushed down during the insertion process, resulting in a higher level of crimp in UD laminates compared to multi-directional ones [32,33]. The amount of crimping is also correlated with the misalignment of Z-pins [33]. Moreover, Z-pins may also damage the neighbouring fibres.

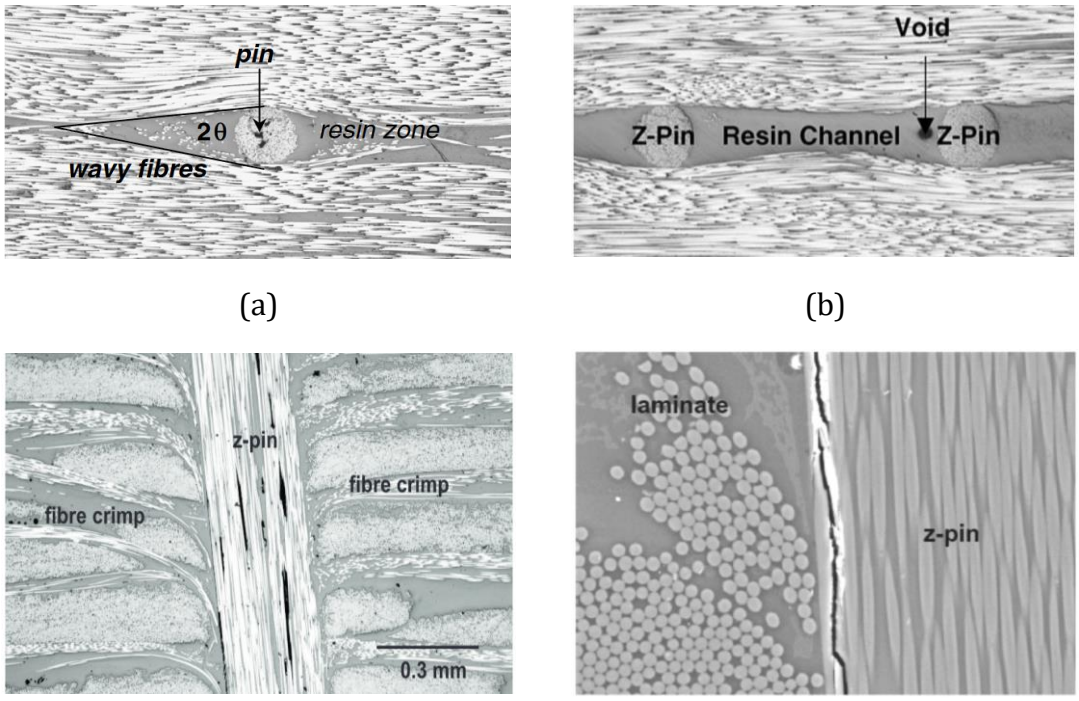

Figure 2.4: Microstructure features of Z-pinned laminates (a) wavy fibres and resin pocket, (b) resin channel, (c) fibre crimping (d) side view of interfacial cracking. (a, b) from Mouritz [2], (c, d) from Mouritz [3].

Interfacial cracking (Figure 2.4(d)) is another typical defect in Z-pinned laminates. Residual stress is generated during the cool-down process of cure, resulting in cracks at the interface between the Z-pin and host laminate. This is due to the difference in thermal expansion coefficients between the pin and host laminate.

The amount of residual stress depends on the Z-pin material, laminate stacking sequence and temperature of cure [27,34].

Z-pinning can cause the swelling of a laminate due to the space taken up by Z-pins and the displacement of the surrounding fibers. For example, a study found that the addition of Z-pins at a 4 vol% content led to an increase of over 15% in the thickness of a carbon/epoxy laminate [33].

2.2 Experimental study on mechanical behaviours of Z-pinned laminates

Z-pinning offers a wide range of benefits, with improved fracture toughness being one of the most significant advantages. As a result, extensive research has been conducted on the mode I, mode II, and mixed-mode I/II interlaminar toughness characteristics of Z-pinned laminates. Numerous experimental and theoretical studies have investigated how various factors related to Z-pinning affect delamination resistance. In this section, we will review published experimental studies on single-pin behaviour, as well as the interlaminar, in-plane and through-thickness properties of Z-pinned laminates.

2.2.1 Single pin response

The behaviour of an individual Z-pin has been studied under different loading conditions. The majority of studies have focused on carbon-fibre pins embedded in carbon-epoxy laminates. During loading, a pin's response includes elastic deformation, debonding, sliding, tensile fracture, subbing, and splitting. The failure mode and bridging behaviour of Z-pins depend on many factors, such as pin insertion angle [35,36], pin material [37], pin surface roughness [38,39], laminate thickness[40], stack sequences [34], etc. A thorough understanding of the behaviour of a single pin is critical for foreseeing the mechanical response of Z-pinned laminates.

For Mode I dominated loading, the pin debonds from the laminate after the stretching period, and then is gradually pulled out in a non-linear stage. There are

two possible failure modes of the pin: debonding followed by pull-out, and rupture without pull-out, as shown in Figure 2.5.

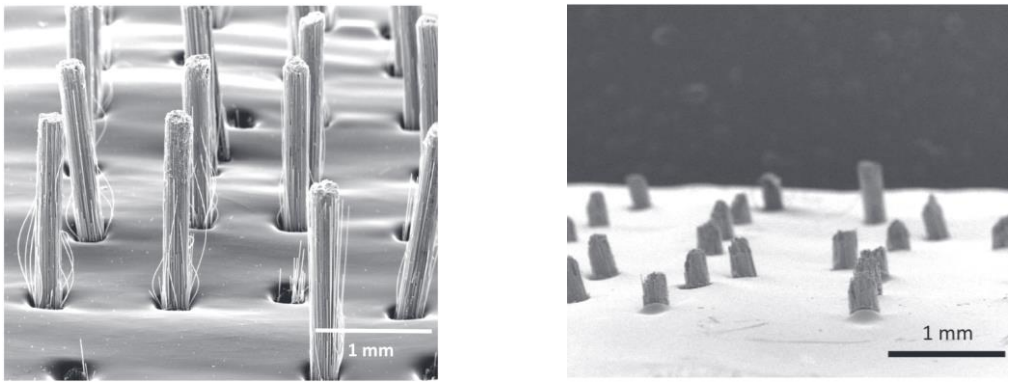

(a) (b)

Figure 2.5: Mode I Z-pin failures (a) pull-out, (b) tensile fracture. From Mouritz [3].

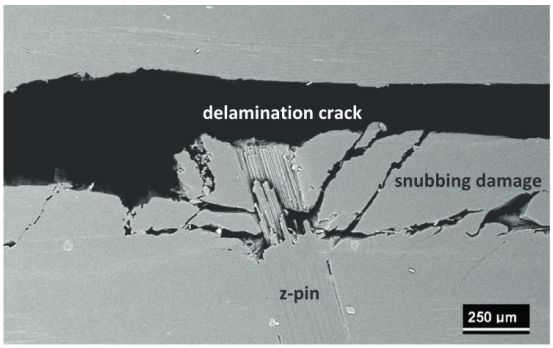

(a)

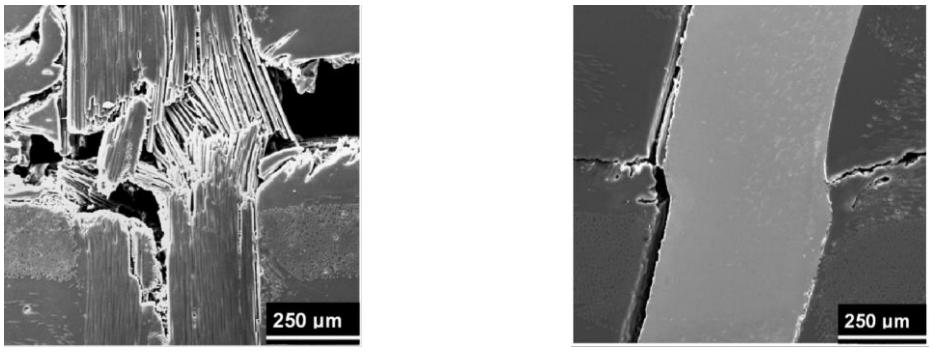

(b) (c)

Figure 2.6: (a) Snubbing induced damage, (b) mode II carbon-fibre pin failure, (c) metal pin within mode II bridging zone. From Mouritz [3].

In mode II dominated loading, the pin deforms locally until it eventually fails. The shear force also causes snubbing damage to the laminate, as shown in Figure 2.6(a). Figure 2.6(b, c) present the rupture of a carbon-fibre pin under transverse shear and the shear deformation of a metal pin. Mixed-mode loading leads to a combination of mode I pull-out and mode II shear rupture, with a transitional behaviour between the two modes.

The anisotropic contraction in UD laminates results in reduced residual stresses, which increases the initial peak load. The residual stresses are higher in multidirectional laminates due to the additional constraint provided by the fibres in the lateral direction. Consequently, the initial high peak load is reduced or eliminated in the mode I bridging-traction curves due to early pin debonding, as depicted in Figure 2.7(a).

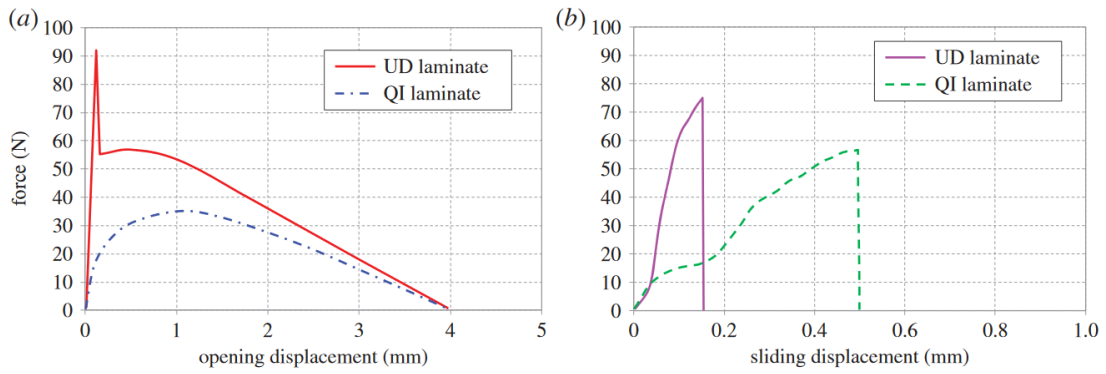

Figure 2.7: Schematic load-displacement curves of (a) mode I, (b) mode II. From Partridge and Hallett [34].

With regards to the influence of pin material, Figure 2.8(a) shows that the carbon-fibre pin has the highest mode I peak traction load due to its better bonding with the laminate [37]. The other metal pins (except copper) and carbon-fibre pin all experience debonding from the laminate, resulting in a load drop before gradually being pulled out from the laminate. In contrast, the copper pin undergoes plastic deformation, necking, and then rupturing, leading to low fracture toughness.

The surface roughness of the pin also affects the mode I bridging behaviour. Figure 2.8(b) compares the load-displacement curves of carbon-fibre pins with different notch depths [38]. The results show an evident improvement in the peak load with

the presence of notches. The behaviour of notched and unnotched pins after debonding differs. The peak load increased by up to 87% with the smallest notch depth, and the dissipated energy increased by 12%. Additionally, Ref. [39] demonstrated a significant increase in the pull-out strength with threaded metal pins.

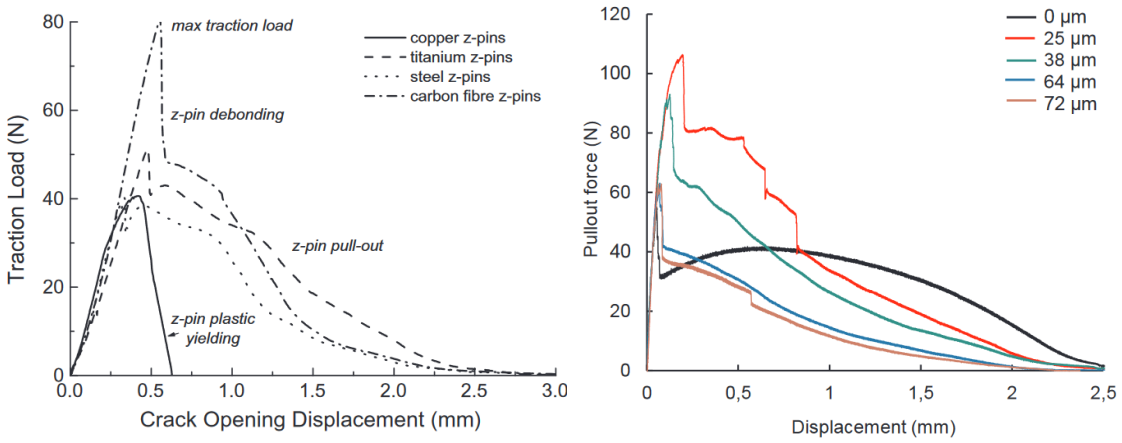

(a) (b)

Figure 2.8: Mode I bridging curves (a) effects of pin material, from Pingkarawat and Mouritz [37], (b) effects of pin surface roughness, from Hoffmann et al. [38].

M'membe et al. investigated the influence of insertion angles on fracture toughness in modes I and mode II [35]. Using 45° inclined stainless-steel Z-pins, the mode I absorbed energy was significantly higher than that of orthogonally inserted ones. However, for mode II, the 45° pins were less effective in energy absorption, compared with mode I. In their another study on mode II [36], when the pins were inserted in alignment with the shear load, referred to as 'with the nap', the peak load and energy absorption significantly increased. For instance, the peak load of a single pinned specimen at an inclination angle of 60° was double that of the traditional 0°, as the pin takes more axial force with the nap.

Yasaee et al. [27] investigated the behaviour of a single carbon-fibre pin under mixed-mode loading conditions, for both UD and quasi-isotropic (QI) laminates. The study found that the traction energy was much higher for mode I dominated conditions. The traction energy decreased abruptly when the toughening

mechanism shifted from pin pull-out to shear rupture, as shown in Figure 2.9(a). The stacking sequence of the hosting laminate directly influenced the pin failure behaviour at mode I and lower mode-mixities due to different residual stresses generated at the pin/laminate interface during the cooling-down process.

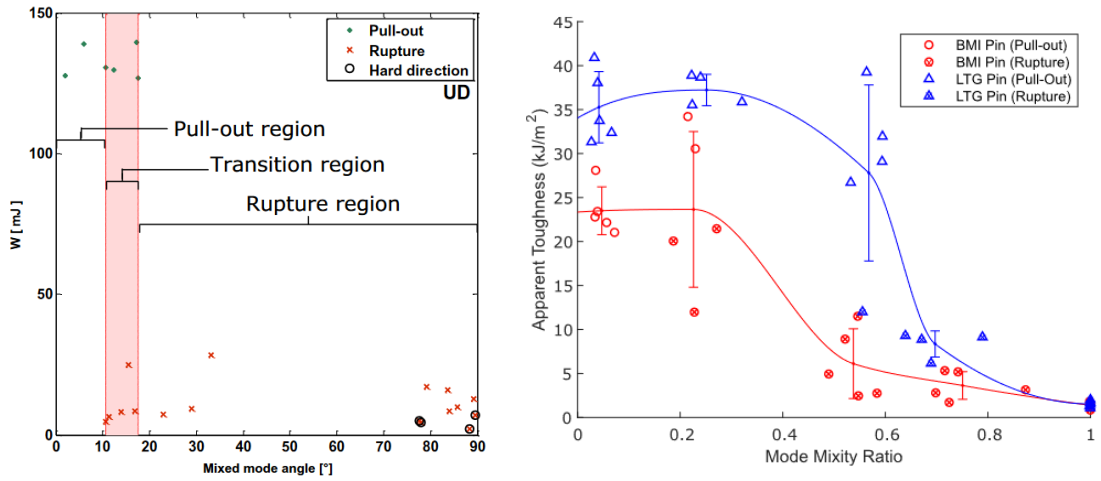

(a) (b)

Figure 2.9: (a) Absorbed energy vs. mixed-mode angle for Z-pinned UD laminates, fromYasaee et al. [27], (b) apparent toughness vs. mode-mixity ratio, from Santana de Vega et al. [41].

Santana de Vega et al. [41] manufactured new types of carbon-fibre pins with various resin systems. The study revealed that utilising a ductile matrix in Z-pins resulted in the ability to withstand more significant shear and bending deformations than the commonly employed brittle BMI resin, which enabled pull-out at the mode-mixity approaching 0.6, while Z-pins made with BMI resin typically failed at a mode-mixity of 0.2. Additionally, the incorporation of a ductile matrix (LTG) in a Z-pin was advantageous for mode I since it increased the interface friction during pull-out, as depicted in Figure 2.9(b).

2.2.2 Interlaminar properties of Z-pinned laminate

Extensive experimental studies have been conducted to examine the interlaminar fracture toughness properties of Z-pinned laminates. In particular, the mode I

double cantilever beam (DCB) test and the mode II end-notched flexure (ENF) test have been employed to evaluate the pertinent toughness characteristics.

Pingkarawat and Mouritz [42] demonstrated that the Z-pin volume content is directly proportional to an increase in mode I fracture toughness (Figure 2.10(a)). Thin Z-pins have better performance than thick ones. Pegorin et al. [43] studied the influence of pin length on both mode I and mode II performance. They found that an increase in Z-pin length enhances the mode I fracture toughness and resistance to fatigue. However, the mode II toughness decreases with pin length (Figure 2.10(b)), as long pins resist rotation during bridging. Short pins are pulled out, whereas long pins fracture without experiencing any pull-out. Pin length has no observed influence on mode II fatigue resistance.

Huang and Waas [44] and Pegorin et al. [45] both reported that a higher pin volume fraction and smaller pin size led to a larger mode II fracture toughness. As the Z-pin density increases, crack propagation transitions from unstable status to stable propagation [44]. When the crack extends, thin pins (0.28 mm diameter) exhibit a toughness threshold, while the enhancement of thick pins (0.51 mm diameter) follows a linear trend [45].

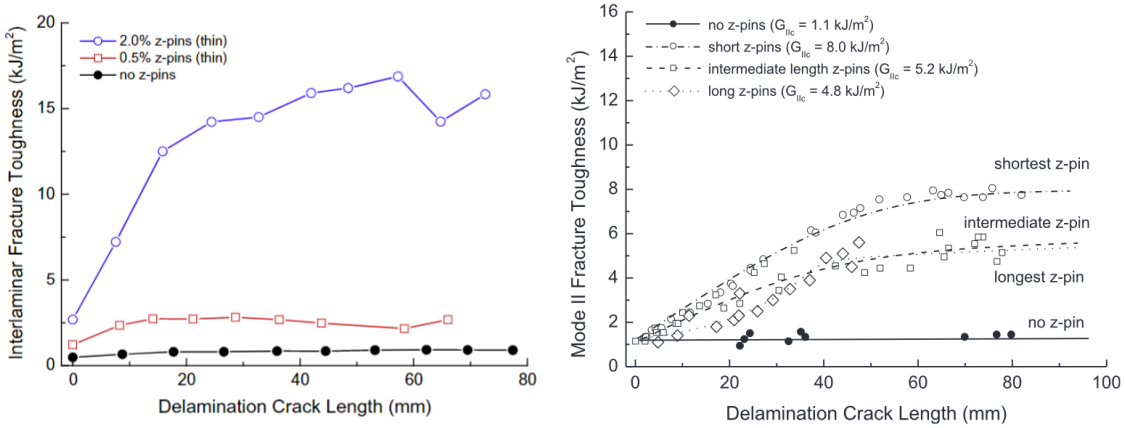

(a) (b)

Figure 2.10: Influence of Z-pin content on the mode I apparent fracture toughness, from Pingkarawat and Mouritz [42], (b) Influence of Z-pin length on the mode II R-curve, from Pegorin et al. [43].

Cui et al. experimentally studied the performance of Z-pinned laminate under dynamic loadings [46–48]. When increasing the loading rate, the efficiency of Z-pins decreased for mode I. The maximum bridging load was not obviously affected by the loading rate for mode II [46]. As the mixed mode ratio increased, Z-pinning became less effective in impeding delamination growth and transitioned from pin pull-out to pin rupture [47]. Z-pins were ineffective in impeding the crack initiation or propagation of delamination less than 5mm under dynamic loadings. However, using Z-pins resulted in a significant delay in the further expansion of cracks. The performance of Z-pinned laminates under mode I domination was sensitive to the loading rate [48].

Several studies have demonstrated the application of Z-pins to T joints. Cartié et al. [49] reported that reinforcing a T-joint with 0.28 mm Z-pins at a 5% areal density resulted in delayed crack initiation, increased peak load to pull the stiffener off, and around 10% growth in absorbed total energy. Li et al. [50] found that the effectiveness of Z-pinning was significantly influenced by the thickness ratio of flange and skin. When the ratio exceeded 0.32, the pins could increase the load carrying capacities of T-joins. In a subsequent study, they [51] found that Z-pinning improved the maximum load by up to 45%. It is worth noting thick pins exhibited significantly superior tensile performance compared to thin pins.

2.2.3 In-plane properties of Z-pinned laminate

Due to the microstructural changes brought to the laminate by Z-pinning, the in-plane mechanical properties are degraded by 5%-10% [3]. Several studies have investigated the effects of Z-pinning on the elastic modulus and strength of composite laminates under in-plane tension [31,33,52,53], compression [30,54,55], and bending [32,56] loadings.

Most studies on Z-pinning have indicated a reduction in the tensile modulus [53] or no outstanding alteration until the Z-pin volume content reaches 4% [31]. In addition, it was found that Z-pinning causes a decrease in the laminate's tensile strength following a linear manner as the Z-pin volume content and diameter

increase [31,33,53]. This decline is primarily due to the occurrence of fibre breakage and laminate swelling during the Z-pin insertion process. It has been shown that the loss of strength in a QI laminate is lower than that in a UD one [31,33], as demonstrated in Figure 2.11.

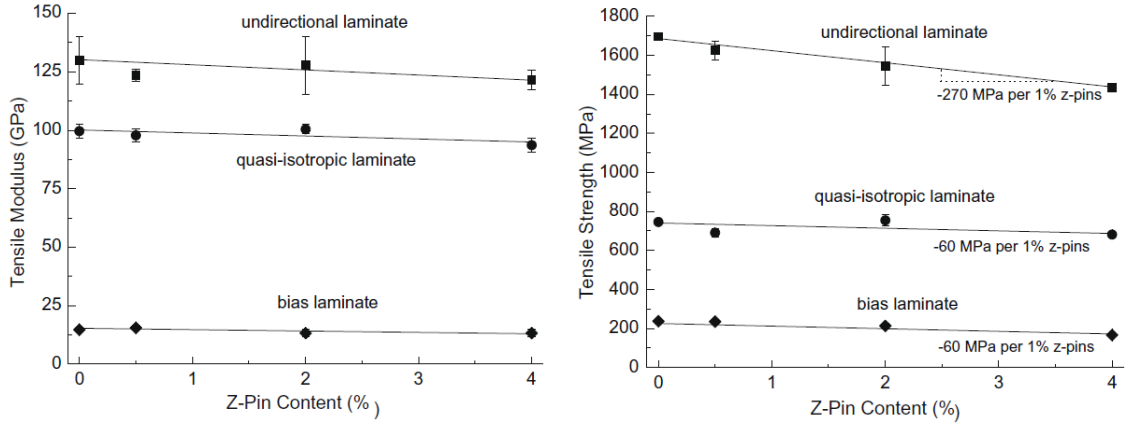

(a) (b)

Figure 2.11: Influence of Z-pin content on (a) tensile modulus, (b) tensile strength. From Mouritz and Chang [31].

Under tensile cyclic loading, Z-pinning has been found to diminish both the fatigue life and strength of laminates [31,33,53]. An escalation in Z-pin content and diameter causes a decrease in fatigue life and strength. The shape of the Z-pins also impacts the tensile strength and stiffness, with rectangular-shaped pins resulting in comparatively less reduction in strength as opposed to circular pins [25,52]. The highest performance is attained with lengthwise inserted rectangular Z-pins [52].

Similarly, Z-pins have been observed to lower both the compression modulus and strength of laminates, with the amount of reduction increasing as the Z-pin volume fraction and size increase [30,54,55]. This decrease is primarily due to the micro-buckling and fibre kinking caused by fibre waviness and crimping during compression. Similarly, Z-pins reduce both fatigue life and strength under cyclic compression loading. The adoption of rectangular-shaped Z-pins led to a lower reduction in compression strength for both UD and QI laminates [55].

Chang et al. [32] found that the flexural modulus is not significantly affected by Z-pin volume content or Z-pin size. The decrease in flexural strength correlates

linearly with Z-pin density and size. A decrease in fatigue life was observed, with thin pins performing better than thick ones. Mouritz and Cox [56] reported a decrease in flexural modulus and strength. The in-plane bending performance loss of a UD laminate is more severe than that of a QI one.

In summary, some general findings of Z-pins on the in-plane performances can be drawn as:

- Z-pins decrease or make no obvious change to the modulus and reduce the strength under both monotonic and cyclic loadings.
- The reduction increases with the pin volume fraction and pin size.
- The reduction in modulus and strength is more significant when the load-bearing direction contains the majority of fibres, i.e. higher in UD than QI.
- The fibre waviness and breakage are the most detrimental to the in-plane mechanical properties.
- Using thinner Z-pins or rectangular pins with more advanced insertion methods could have a mitigation to the loss of in-plane performance.

2.2.4 Through-thickness properties of Z-pinned laminate

There is limited research on the investigation of through-thickness properties in Z-pinned laminates. Currently, no experimental work has been reported to measure the through-thickness modulus of Z-pinned composites. Only one published paper [9] has explored the use of four-point bending tests on L-shaped composite beams to determine the through-thickness tensile failure load. Grooved stainless-steel Z-pins were used in the curved region. Physical and chemical treatments were applied to the pin surface with the purpose of increasing the friction force between the embedded pins and the surrounding laminate. Results showed that the application of thin pins (0.3 mm diameter) and thick pins (0.5 mm diameter) increased the curved beam strength by 21%, 27%, and 42%, and 8.7%, 12%, and 32%, respectively, at the areal densities of 0.5%, 1%, and 2%.

However, the failure mechanism of unpinned and Z-pinned laminates has not been thoroughly examined, and the effects of different types of pins have not been

studied, i.e. mostly used carbon-fibre pin and metal pin. As a result, there remains a significant gap in our understanding of the impact of Z-pins on through-thickness damage initiation. To address this knowledge gap, Chapters 3 and 4 of this thesis will delve into a comprehensive investigation of this matter through both experimental and numerical approaches.

2.3 Experimental study on multi-functionalities of Z-pinned composites

In recent times, there has been a significant increase in interest in the investigation of multi-functional properties of composites, beyond their primary load-bearing role. Several studies have been conducted on the multi-functionality of Z-pinned composites [10–19]. Table 2.1 provides a comprehensive summary of the relevant research studies that have been published.

2.3.1 Self-sensing with Z-pins

The first study to evaluate the feasibility of using Z-pins as a structural health monitoring approach for identifying delamination cracks inside laminates was conducted by Zhang et al. in 2016 [10]. They characterized the self-sensing functions of single T300/BMI Z-pinned laminate coupons for mode I and mode II delamination by measuring the through-thickness electrical resistance in real time. The complete pull-out process of Z-pins can be monitored for the conductive CFRP laminate.

The authors further developed the delamination-monitoring technique to include laminates with conductive Z-pin arrays and suggested a design approach for multifunctional Z-pinned laminates at the structural level [11]. This approach involves connecting Z-pins via electrode arrays fixed to the laminate surfaces (see Figure 2.12).

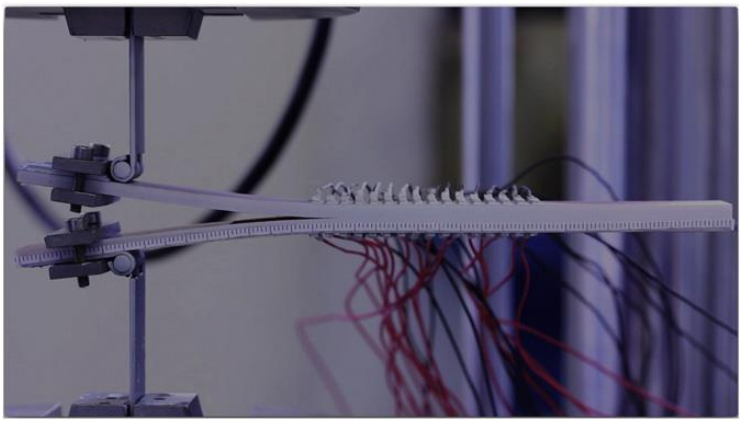

Figure 2.12: DCB coupon under testing. From Zhang et al. [11].

Table 2.1: Summary of published research on multi-functionalities of Z-pin.

Authors	Research
Zhang et al. 2016 [10]	Failure sensing of mode I & mode II test under static loading;
Zhang et al. 2016 [11]	Failure sensing of DCB test under static loading;
Pegorin et al. 2017 [12]	Experiments on electrical property enhancement;
Pegorin et al. 2018 [13]	Failure sensing of DCB test under static and fatigue loading;
Pegorin et al. 2018 [14]	Numerical analysis of the heat transfer;
Grigoriou et al. 2019 [15]	Failure sensing on flatwise compression and DCB tests of sandwich structure under static and fatigue loading;
Li et al. 2019 [16]	Experimental and numerical study of thermal conductivity enhancement;
Kadlec et al. 2020 [17]	Failure sensing on tensile test of adhesive-bonded composite lap joints under static and fatigue loading;
Li et al. 2021 [18]	Experimental and numerical study on the heat transfer for hybrid laminates;
Zhang et al. 2022 [19]	Failure sensing of mode I & mode II test under static and cyclic loading;

Pegorin et al. [13] proposed a similar approach for the mode I delamination monitoring with Z-pin arrays as an extension of the above study by Zhang et al. [11]. Instead of attaching the electrode to each protruding pin end, they bonded thin copper strips to the top and bottom surfaces. The influence of pin volume fraction and pin material on crack monitoring was studied under both static and fatigue loading. Compared with control unpinned samples, the variation of resistance for Z-pinned coupons was much higher during the crack propagation, and the sensitivity could be controlled by the volume fraction and type of Z-pins. Grigoriou et al. [15] conducted a similar research for Z-pinned composite sandwiches.

In the research of Kadlec et al. [17], the crack growth along the bond-line of composite lap joints under fatigue loading (Figure 2.13(a)) was also monitored with Z-pins. As shown in Figure 2.13 (b), the length of the fatigue crack and the rise in resistivity are strongly correlated.

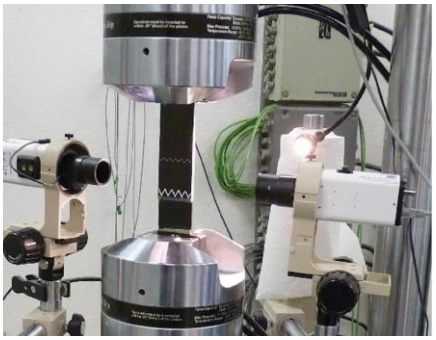

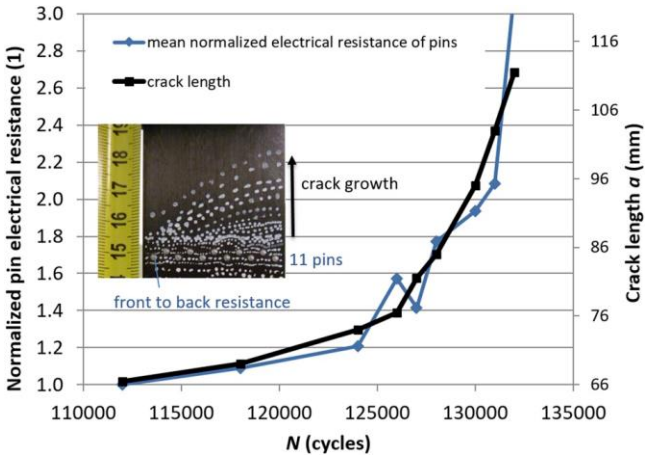

(a) (b)

Figure 2.13: (a) Test set-up, (b) measured electrical resistance during crack growth. From Kadlec et al. [17].

More recently, different from the aforementioned sensing techniques with the measurement of electric resistance change with Z-pins, Zhang et al. proposed a novel method for sensing delamination of Z-pinned composite laminates based on electromagnetic induction [19]. The method involves embedding ferromagnetic Z-pins into the composite material and then applying an external electromagnetic

field to induce eddy currents within the material. As shown in Figure 2.14, two coils were used, with the first coil generating a magnetic field and the second detecting delamination by producing a quantifiable electrical signal. This sensing approach was verified through the mode I and mode II testing under monotonic and cyclic loadings of specimens reinforced with ferromagnetic Z-pin arrays.

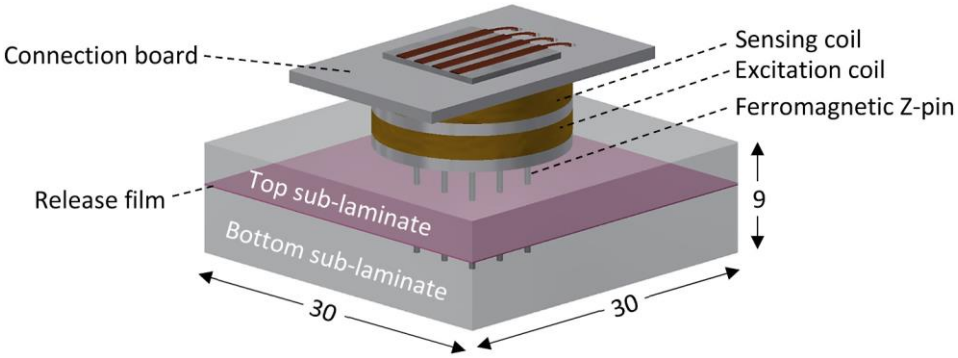

Figure 2.14: Specimen configuration. From Zhang et al. [19].

2.3.2 Electrical and thermal properties

Research has also been carried out to characterise the electrical and thermal properties of Z-pinned laminates and sandwiches. Z-pins were found to be very effective in the through-thickness direction.

Pegorin et al. [12] found that the through-thickness electrical conductivity increased with pin volume content linearly, with the enhancement of 1.84 vol% copper pins up to 10^6 times. A similar observation was made for composite sandwich structures by Grigoriou et al. [15]. Z-pins significantly improve the through-thickness conductivity of composite sandwich structures. However, the pins did not enhance the in-plane conductivity of both composite laminates and sandwiches because of the interfacial cracks that formed around the pins [12,15].

However, in Ref. [12], the top and bottom surfaces were connected using silver paste, intentionally engaging the pins to facilitate current conduction. In contrast, Chapter 5 of this thesis focuses on studying the response of both unpinned and Z-pinned laminates under a fault current at different locations for the first time. The objective is to investigate the localised current conduction characteristics around

the pins and within the laminate itself, providing valuable insights into this realistic scenario.

Li et al. [16] utilized Z-pins and graphite sheets to create a structure with 3D-enhanced thermal conductivity. The study revealed that Z-pins significantly increased the through-thickness thermal conductivity, with an increase of up to 647% when using the M55J-6K carbon fiber Z-pin (HM) with a volume fraction of 2.7% for the laminate with pyrolytic graphite sheet (PGS) at 25 °C, as depicted in Figure 2.15.

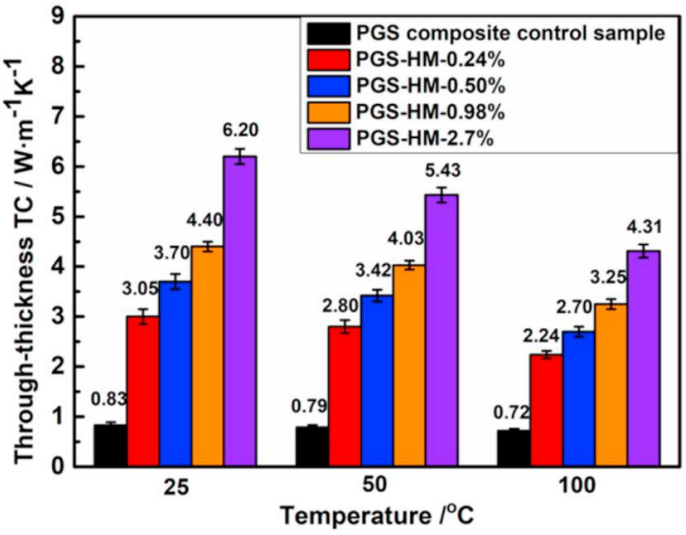

Figure 2.15: Through-thickness thermal conductivities of composite control sample and composites with Z-pins. From Li et al. [16].

In a subsequent study, they [18] developed a hybrid graphite sheet (GS) and carbon-fibre (CF) composite laminate with Z-pins for heat transfer investigation. The study observed an increase in in-plane thermal conductivity due to the combined heat transfer of the graphite sheet and pins. Figure 2.16 displays an infrared thermography image of a Z-pinned hybrid laminate, highlighting brighter regions that represent the heat transfer paths. For the [GS/CF_4/GS] laminate with single pitch pin, the through-thickness and in-plane thermal conductivities were found to be 13.7 and 8.3 times greater than those of the control sample, respectively.

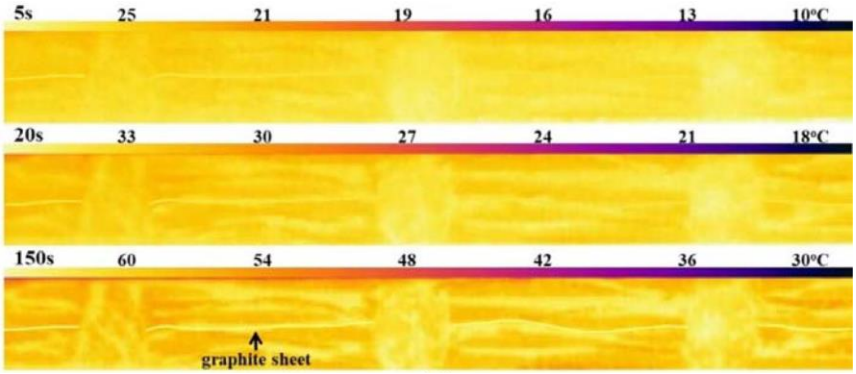

Figure 2.16: Infrared thermography of a hybrid laminate [CF_2/GS/CF_2]. From Li et al. [18].

However, to date, there has been a lack of relevant studies focusing on the effects of Z-pins on the magnetic performance of composite laminates. In order to bridge this research gap, Chapter 6 of this thesis will thoroughly examine the overall in-plane and through-thickness magnetic performance of both unpinned and Z-pinned laminates. The investigation will encompass various pin materials and volume fractions, allowing for a comprehensive understanding of their impact.

2.4 Numerical modelling of Z-pinned laminates

2.4.1 Mechanical behaviours

To characterise the bridging mechanisms and failure of Z-pinned composite laminates, multi-scale FE analysis is typically conducted. At the meso-1 level [57–60], the analysis involves FE modelling along with the results of individual Z-pin tests to determine either the mode-mixity-dependent bridging forces or apparent fracture toughness. Additionally, semi-analytical simulation is employed assuming the pin to be an Euler-Bernoulli beam that is embedded in an elastic basement [61–64]. The results obtained from the meso-1 level are subsequently utilised in the moso-2 level or macro-scale models to predict the response of Z-pin arrays.

2.4.1.1 Meso-1-level modelling

Micro-scale simulations have been used to define the behaviour of individual Z-pin. They provide in-depth insights into the micro-structure and micro-mechanics of Z-pinned laminates. Different FE simulations have been proposed to simulate the single Z-pin bridging responses under mode I, mode II, and mixed-mode loading, using the unit cell model [57,58,61,65], 2D plane-stress model [59,60] and 3D high-fidelity model [66–69].

For the single Z-pin pull-out process, Meo et al. [65] built the unit cell model with solid elements. The contact-elements were introduced to the pin/laminate interface to represent the contact and sliding. The frictional force during pullout was described by residual stress plus a Coulomb friction factor. Bianchi and Zhang [57] proposed that the pull-out resistance is caused by friction alone, resulting from the compressive residual stress around the pin due to the curing process. A meso-scale model was created, as depicted in Figure 2.17.

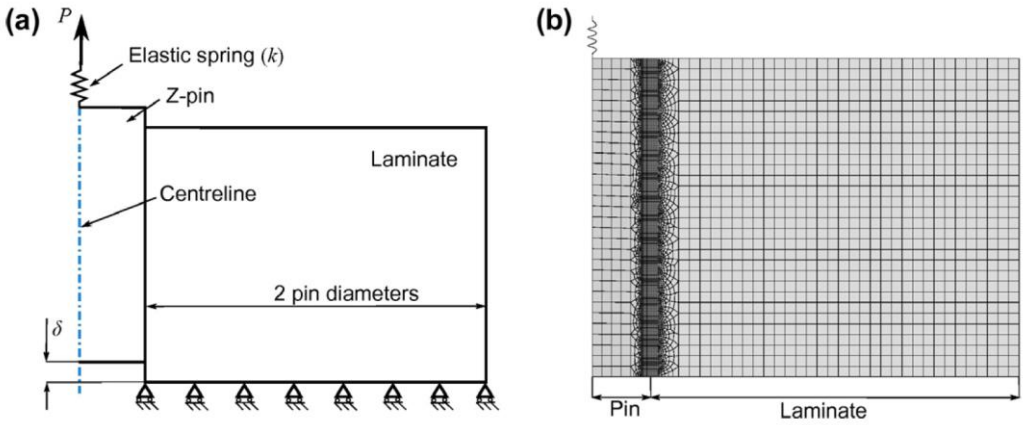

Figure 2.17: The meso-scale model (a) illustration, (b) FE mesh. From Bianchi and Zhang [57].

Cui et al. [59,60] employed a high-fidelity 2D plane-stress model to simulate the behaviour of a single pin under mode I and mode II conditions, which saves the computational time and it is simple to set up. Cohesive elements were introduced to the potential failure regions to simulate the pin/laminate debonding, pin splitting, and pin rupture, as shown in Figure 2.18. The pin and host laminate were

assumed to be bonded at the begining, then followed with debonding and friction sliding.

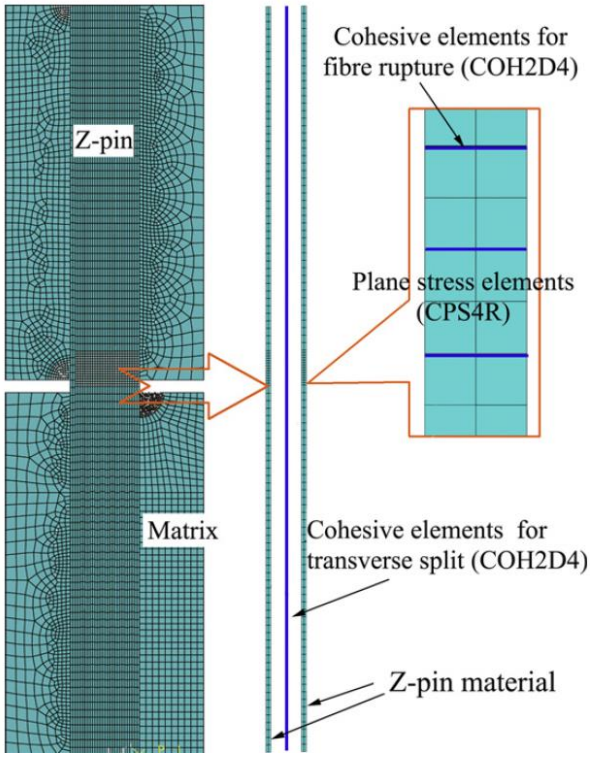

Figure 2.18: 2D plane-stress numerical model. From Cui et al. [59].

3D high-fidelity models containing the microstructure features and different failure modes of pins have been investigated [66–70]. The first high-fidelity 3D FE unit cell model of Z-pinned laminate was performed by Dickinson et al. [66] in 1999 to obtain the engineering elastic constants, in which a star-like geometry was adopted to model the microstructural features.

Zhang et al. [67] created a very detailed 3D micro-mechanical FE model to forecast the response of a single pin under mixed mode. A similar star-shaped ply-level mesh (Figure 2.19(a)) was used. Cohesive elements were inserted between the pin/laminate interface to simulate the pin pull-out process, and inside the pins to model the splitting (Figure 2.19(b)). The influence of the post-cure cool-down process was also included to analyse the residual stress.

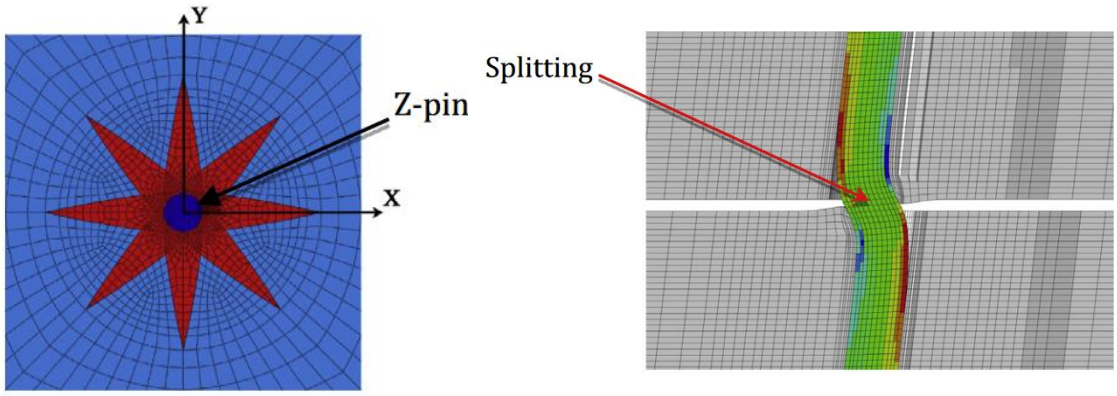

(a) (b)

Figure 2.19: (a) Star-shaped ply-level mesh, (b) Z-pin splitting. From Zhang et al. [67].

Li and Chen [69] have recently introduced an advanced approach to simulate a variety of Z-pin failures, such as pin splitting, pin rupture, snubbing, and interfacial debonding, by embedding zero-thickness cohesive elements into every element pairs in the damage zone. Figure 2.20 illustrates the cohesive elements implanted in a Z-pin and resin-rich zones. Although this approach is the most detailed one to date, it comes at a higher computational cost.

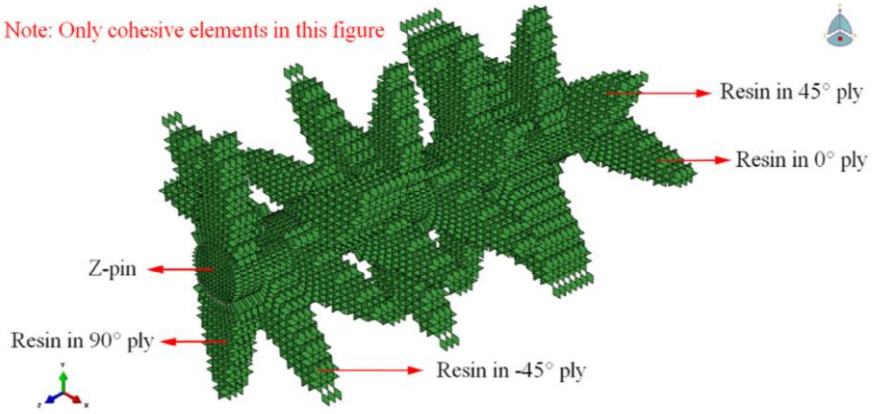

Figure 2.20: The implanted cohesive elements in a pin and resin pockets. From Li and Chen [69].

2.4.1.2 Meso-2-level modelling

There are three typical ways to model the reinforcement with multiple Z-pins in a laminate. (1) discretely model every single pin with spring elements, which

requires knowledge of the Z-pin locations and remeshing when the geometry changes [50,61]. (2) smear the Z-pin bridging force over the reinforced area and use separate laws for the cohesive elements of unpinned and localised Z-pinned regions, which also requires consideration of individual Z-pin locations [57,58,60,61]. (3) smear the Z-pin bridging response over the entire reinforced area using cohesive elements, which requires a highly automatic solution for the single pin bridging response [63,64].

In Ref. [57], a traction-separation law derived from the meso-scale single pin pull-out model was implemented into the cohesive elements at each pin location for the macro-scale DCB model to represent the enhanced delamination toughness by Z-pins. Another separate traction law was used for the cohesive elements of unpinned regions, as shown in Figure 2.21. This similar unit strip cohesive-pin model was later used for mode II loading in Ref. [61], together with a spring-pin model in which the nonlinear spring elements were employed to model each pin. The spring-pin model was found to have difficulty converging, and the computation time was four times higher than the cohesive-pin model.

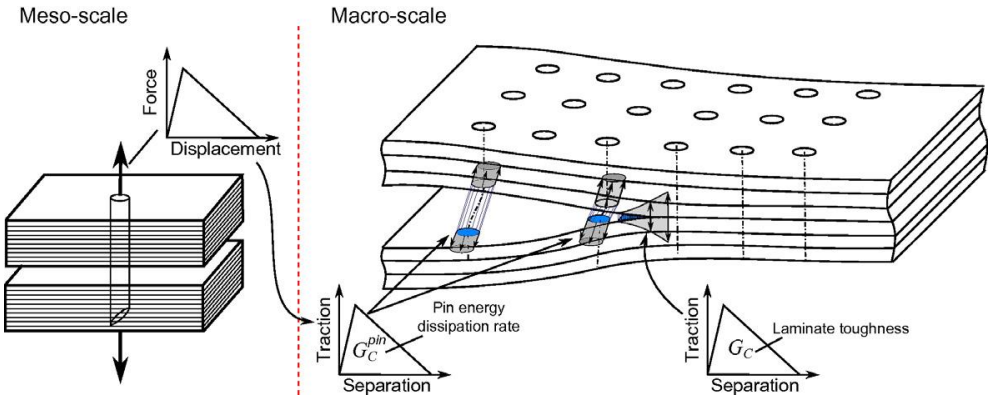

Figure 2.21: Modelling strategy of DCB Z-pinned laminate. From Bianchi and Zhang [57].

Cui et al. developed a cohesive law for mixed-mode loadings by incorporating the mode I and mode II bridging behaviour with two separate traction-separation laws [60]. As shown in Figure 2.22, cohesive elements were inserted in the interlaminar to simulate both the unreinforced areas' delamination and the Z-pinned regions' failure response. The cohesive elements for Z-pins were divided into 'tension'

elements and 'shear' elements with equal area. The results obtained from the DCB, ENF, and mixed-mode bending tests showed a good correlation between experimental and numerical results.

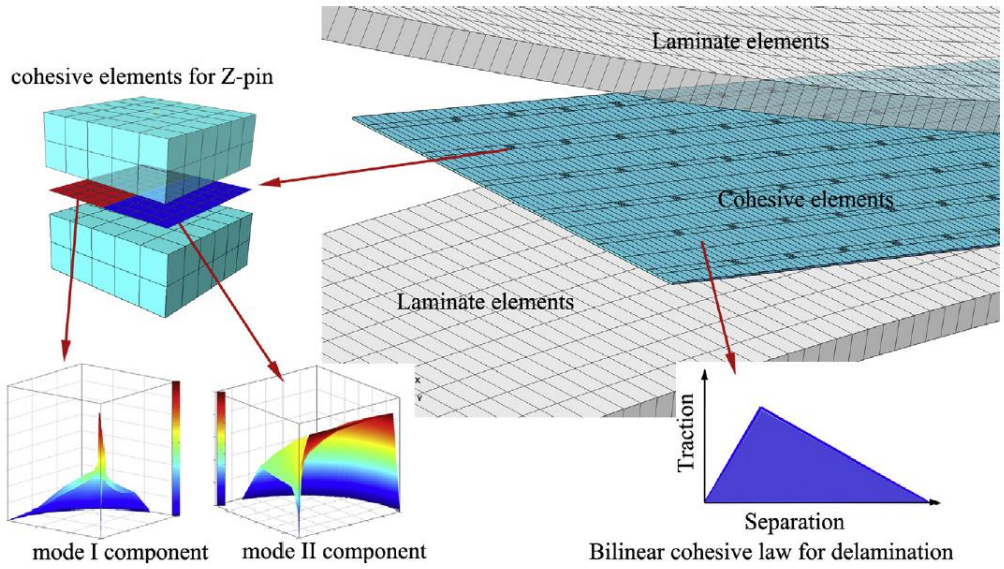

Figure 2.22: Mesh distribution at Z-pinned interface. From Cui et al. [60].

A new computational approach was suggested by Mohamed et al. [63], which combines the conventional FE method with a semi-analytical Z-pinned model. This was achieved by interpolating external bridging maps. The cohesive element formulation was then integrated with the micro-mechanical constitutive bridging model. A complete bridging map can be obtained during the analysis for every mode-mixity, which is independent of the experimental data and high-fidelity FE models that were used in the previous papers.

Melro et al. [64] established a bridging-map library by calculating micro-mechanical semi-analytical models. They then integrated the predictions into the cohesive element formulation with a tri-linear law to describe the bridging mechanism due to Z-pins. The multi-scale framework is shown in Figure 2.23. Specifically, the bridging map was determined from the dissipated energy and the total displacement at failure using the displacement at each time increment for a certain mode-mixity.

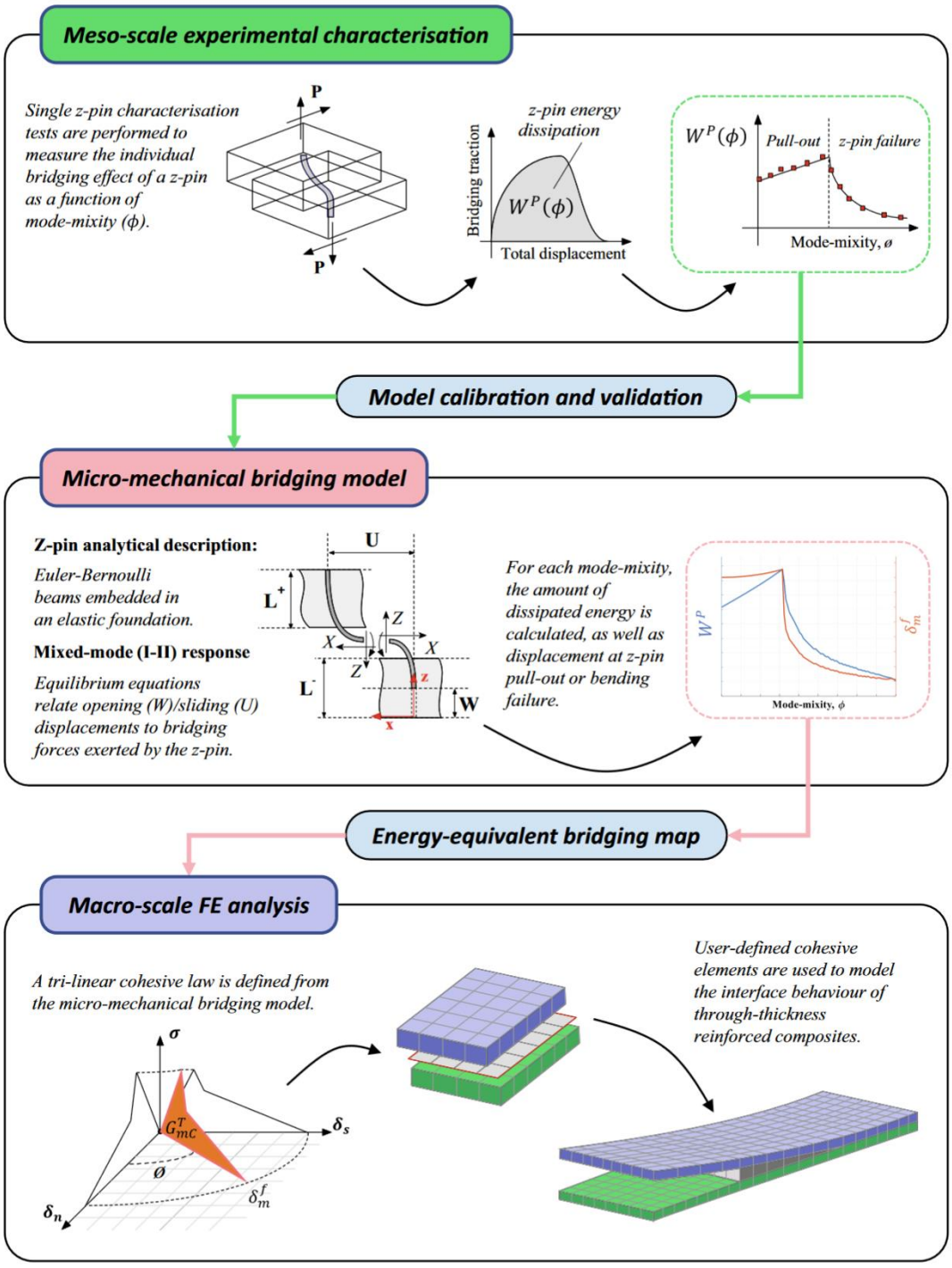

Figure 2.23: Multi-scale framework. From Melro et al. [64].

2.4.2 Multi-functionalities

Compared to the sophisticated FE modelling studies on the mechanical performance of Z-pinned laminates reviewed above, there is much less work on other properties, i.e., multifuctionalities.

Through FE modelling, Pegorin et al. [14] predicted the through-thickness thermal diffusivity of unpinned and a variety of Z-pinned laminates using Abaqus. The pin was modelled as straight without misalignment, and microstructural features induced by Z-pinning were not considered. The pins functioned as thermal pathways, and the through-thickness thermal conductivity increased with pin content linearly. The results showed that incorporating 5 vol% copper Z-pins increased the through-thickness conductivity of the laminate by approximately 10 times.

Representative volume element (RVE) models were created in Abaqus to investigate the heat transfer mechanism [16,18]. Figure 2.24 illustrates the modelling result in Ref. [18], which captures the heat flux transport between the Z-pin and the graphene sheet.

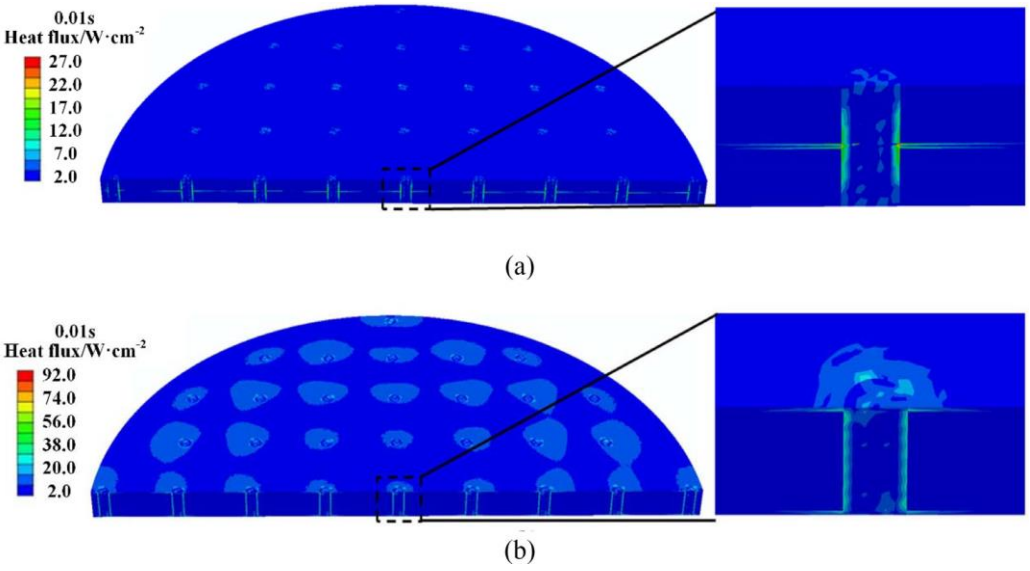

Figure 2.24: The modelling result of heat flux field of (a) [CF_2/GS/CF_2] and (b) [GS/CF_4/GS] laminates. From Li et al. [18].

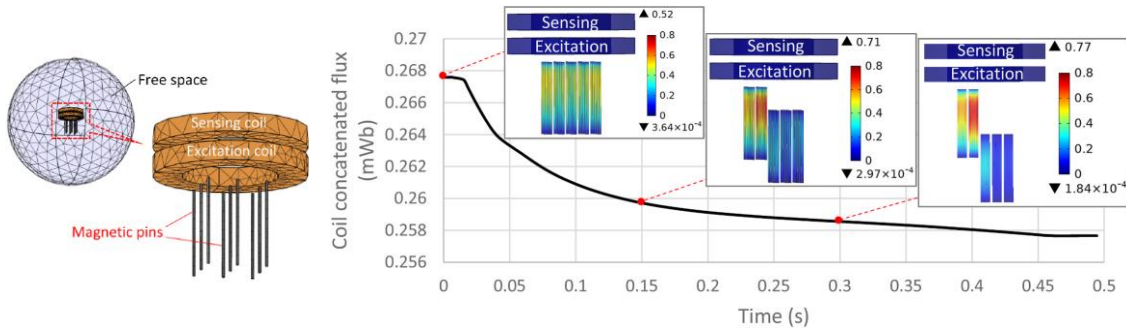

(a) (b)

Figure 2.25: (a) FE model, (b) the modelling result of magnetic flux distribution under mode I loading. From Zhang et al. [19].

In the sensing work described in Ref. [19] by Zhang et al., electromagnetic modelling was conducted using COMSOL. Each pin was treated as perfectly straight. The glass-fibre reinforced laminate and coil nylon core were not modelled as their permeabilities are close to that of free space. The specimen was enclosed in a free-space sphere to capture the surrounding magnetic flux distributions, as shown in Figure 2.25(a). The mode I & mode II tests were modelled by applying appropriate displacement and boundary conditions to the pins for the different failure modes. The sensing signal predicted by the model agrees well with the experiment. The FE model gives an intuitive view of the magnetic flux density and distribution inside the pins as shown in Figure 2.25(b).

2.5 Conclusions

Inserting Z-pins through the thickness of a laminate is a highly effective method for improving the interlaminar fracture toughness of laminated composites. This technique has been extensively explored under mode I, mode II, and mixed-mode loading conditions. However, the use of Z-pins can introduce damages that reduce the in-plane properties of the laminate. On the other hand, there is little research on the through-thickness properties of Z-pinned laminates, so one of the objectives of this thesis is to address this gap. In addition, simulation of the impact of curing on complex Z-pinned structures is limited in the literature review, which will also be investigated in this thesis.

Although extensive research has been conducted on the mechanical performance of Z-pinned laminates, only limited studies have experimentally demonstrated the additional functionalities of Z-pins in composites, including delamination sensing, and enhanced electrical and thermal properties. The relevant modelling work is even less. There is still a great deal of exploration required to combine the exceptional mechanical performance of Z-pins with other functions to be used in composites. Hence, this thesis will investigate the multifunctional applications of Z-pins in composites experimentally along with preliminary FE modelling, aiming to create next-generation Z-pinned composites with more versatile performances.

3 EXPERIMENTAL STUDY OF Z-PINNED CURVED LAMINATE UNDER FOUR-POINT BENDING

3.1 Introduction

As illustrated in the literature review chapter, substantial research has been conducted on the interlaminar fracture toughness of Z-pinned flat laminates. This aspect stands as the most significant contribution of Z-pins, as they effectively resist damage propagation by forming a large bridging zone [2,3].

However, the impact of Z-pins on the through-thickness properties was scarcely studied [2,3]. The majority of through-thickness tensile data in the literature has been generated through indirect test methods, because conducting through-thickness uni-axial tension tests poses significant challenges [71,72]. Fabricating material of uniform quality in sufficiently thick sections and introducing loading without the deleterious influence of end effects and stress concentrations is a difficult task.

Therefore, in this chapter, the four-point bending of a curved beam was chosen as the preferred method to characterize the through-thickness properties of Z-pinned laminates. This particular testing technique is deemed suitable as it not only enables the evaluation of relevant properties but also simulates a realistic structural configuration.

A typical example of a curved composite beam subjected to through-thickness tensile loading is an L-shaped joint used in the leading edge of aircraft wings. The L joint withstands a bending moment, and usually leads to delamination due to the high through-thickness tensile stress in the curved section [73–77]. In contrast to the extensively studied ability of Z-pins to resist damage propagation, this case aims to investigate whether Z-pins are effective in delaying the initiation of interlaminae cracks. In the open literature, there is only one relevent published experimental work with grooved metal pins as shown in (Figure 3.1(a)) [9]. Moreover, to the authors' knowledge, no relevant modelling work has been attempted for the aforementioned case. Thus, a comprehensive understanding of the effects of pin material and areal density of the TTS and the failure mechanism of a curved laminate are esstntial.

This chapter investigatesthe effects of the most commonly used T300/BMI carbon-fibre composites Z-pins (Figure 3.1(b)) and diamond-particle-coated steel pins (Figure 3.1(c)) on the TTS of curved composite laminates via four-point bending tests. The rationale behind selecting these two types of pin materials stems from the contrasting performance observed in previous research. Carbon-fibre pins, for instance, exhibit outstanding performance in mode I, whereas metal pins demonstrate superior characteristics in mode II. Given that different pin arrays experience varying mode-mixities in this curved beam section, it is valuable to investigate both types of pin materials to gain a comprehensive understanding of their behaviour. The specimen design and preparation are introduced in Section 3.2. The four-point bending test, together with the relevant results are presented in Section 3.3. The discussion of results is given in Section 3.4.

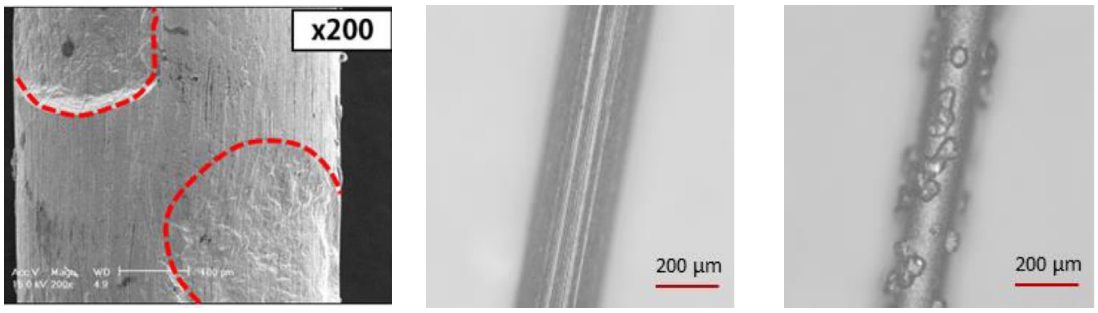

(a) (b) (c)

Figure 3.1: Microscope images of (a) 0.5 mm metal pin from Ju et al. [9], (b) carbon-fibre pin of this study, (c) diamond-particle-coated steel pin of this study.

3.2 Specimen design and preparation

The specimens studied here are curved laminates with the layup of [0, (+45/0/-45/0)$_2$ (+45$_2$/-45$_2$/0$_2$)$_3$]$_s$. The design was inspired by the work of Xu et al. [78], who used a similar specimen to embed wrinkle defects in a corner radius. That work in turn was built off the ASTM D6415/D6415M test standard for laminated composites' through-thickness strength [79]. As shown in Figure 3.2, the sample inner radius, width and thickness are 10 mm, 25 mm, and 6.75 mm respectively. The angle between the specimen's two legs is 90°. IM7/8552 carbon/epoxy UD prepreg from HexPly® was used to manufacture the laminates. Two types of pins were employed, i.e. T300/BMI carbon-fibre composites pins and metal pins coated with diamond particles to increase the surface friction. The diameter of the carbon-fibre pin is 0.28 mm, and the outer diameter of the metal pin is between 0.23 and 0.26 mm.

Five types of samples were manufactured. The control unpinned samples are named 'C', low-density (0.27%) and high-density (0.54%) carbon-fibre Z-pinned specimens are named 'L' and 'H', and the low-density and high-density metal pinned specimens are named as 'ML' and 'MH', respectively. The reference pinning areal density was calculated at the mid-plane of the curved section.

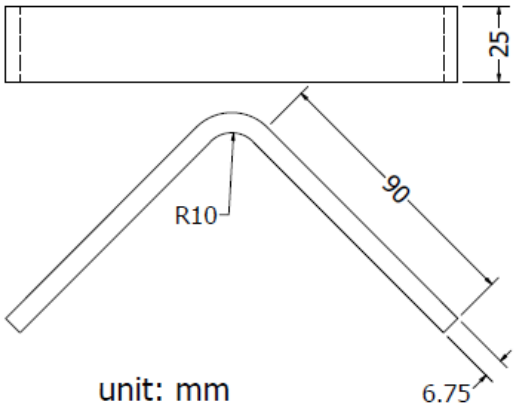

Figure 3.2: Sample geometry.

Due to the curved shape, a steel mould with the same radius of 10 mm was used for the layup and cure. The laminate was transferred to a high temperature epoxy mould for the pinning. The primary stages of the production process are as follows:

- Align the centrelines of the pregreg and steel mould and layup the pregreg onto the mould (Figure 3.3(a)).
- Conduct the debulking inside a sealed bag for 15 mins after the layup of every four plies to reduce air content (Figure 3.3(b)).
- Insert the pins into pre-drilled holes manually through the thickness of the curved section. A pair of wedges were put underneath the epoxy mould to control the pinning angle of each row, as shown in Figure 3.3(c, d).
- Cure the laminate in an autoclave, following a modified standard cure cycle [80], to which 30 mins were added for each dwelling stage to account for the effects of silicon rubbers that were applied to the top and bottom of the laminate to protect the pin ends as the laminate compacts.
- Trim the protruding pin ends with scissors. The photo of a cured laminate is given in Figure 3.3(e).
- Cut individual specimens from the cured laminate, which includes two steps: 1) cut the samples off the panel with a bandsaw roughly; 2) use a diamond face milling machine to size.

- Polish two side surfaces of the sample with fine P1200 sandpapers to ensure smoothness of the edges (Figure 3.3(f)).

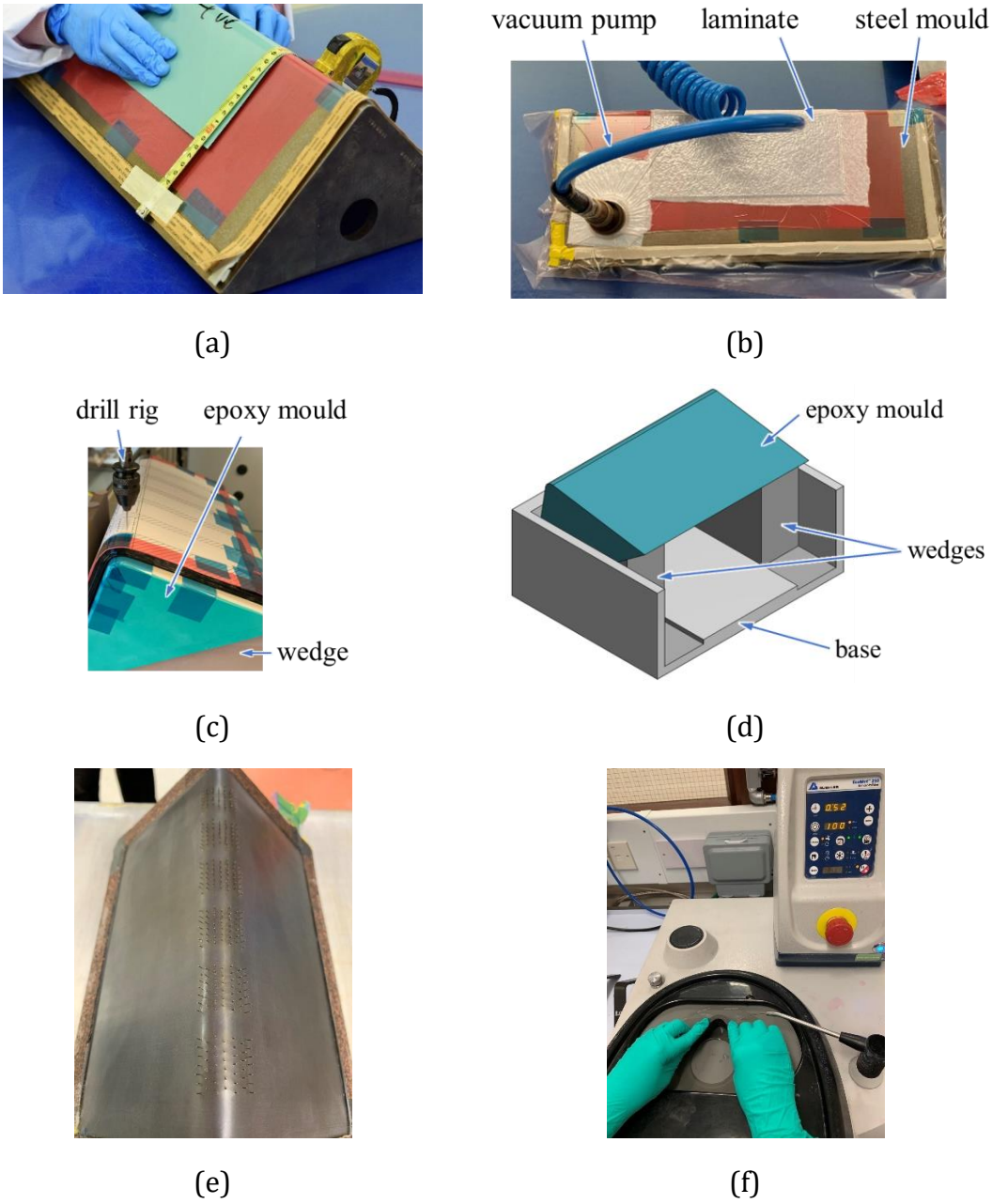

Figure 3.3: (a) layup, (b) debulking, (c) pinning, (d) pinning assembly, (e) the cured laminate, (f) sample polish.

The manufactured carbon-fibre Z-pinned samples and the top views of the pins are shown in Figure 3.4. As the laminates have a curved shape, a zig-zag configuration

was designed for pinning to avoid the pins' potential intersection at the inner surface.

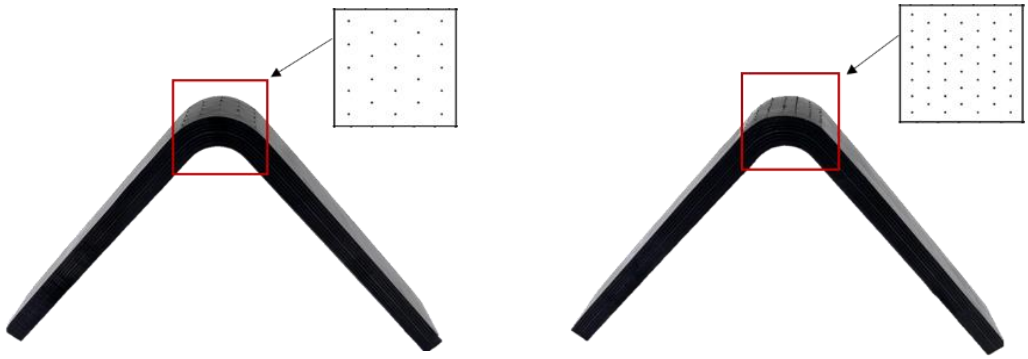

(a) (b)

Figure 3.4: (a) 0.27%, and (b) 0.54% carbon-fibre Z-pinned specimen photos.

3.3 Four-point bending test

3.3.1 Test set-up

The test method follows the ASTM D6415/D6415M – 06a standard [79]. The distances between top and bottom rollers are 60 mm and 92 mm respectively. The experimental set-up is shown in Figure 3.5.

A hydraulic-driven Instron 8872 with a 25 kN load cell was used for loading the specimens at a rate of 1 mm/min under a displacement control. A high-speed video camera and a video gauge were placed in front of the sample to record the failure events. The primary objective of employing a high-speed camera is to observe and capture any potential crack propagation events. This is particularly significant because previous literature has demonstrated the effectiveness of pins in resisting crack propagation. The frame rate of the high-speed camera was set as 50,400 fps.The tests were stopped manually when a 50% load drop had been observed. It is worth noting why DIC (Digital Image Correlation) was not utilied in this study. Firstly, employing DIC painting would have made it difficult to differentiate crack occurrences among individual plies. Moreover, the main objective of this experiment was to evaluate the effectiveness of Z-pinning in the specific scenario

under investigation. Analyzing strain distribution was not within the scope of our research focus.

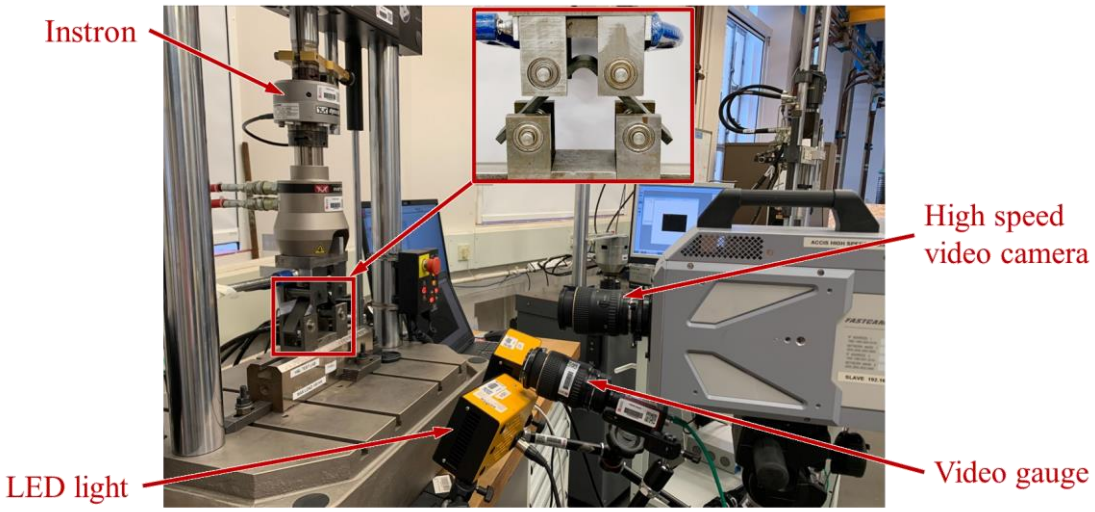

Figure 3.5: Test set-up photo.

3.3.2 Experimental results

3.3.2.1 Load-displacement curves

By comparing the images taken by the high-speed camera just before and after the failure, it was found that delamination happened suddenly within 30 frames, corresponding to approximately 0.6 milliseconds. Once the delanimation happened in the critical middle region, the structure lost its load-bearing capacity immifiately, and no crack propagation was observed.

Five samples were tested in each group and individual load-displacement curves are given in Figure 3.6. The load-displacement curves increase almost linearly until delamination occurs. For each type of sample, the linear parts overlap, demonstrating the consistency of the test set-up. The unpinned samples tend to exhibit one large load drop corresponding to failure, albeit some smaller load reductions can be observed in the charts. However, there was no obvious damage onset corresponding to those.

For the carbon-fibre Z-pinned specimens, four out of five samples with a density of 0.27% and two out of five samples with a density of 0.54% exhibited two

significant load drops. Similarly, three out of five metal pinned samples exhibited two load drops at each areal density. The remaining Z-pinned specimens exhibited only one load drop.

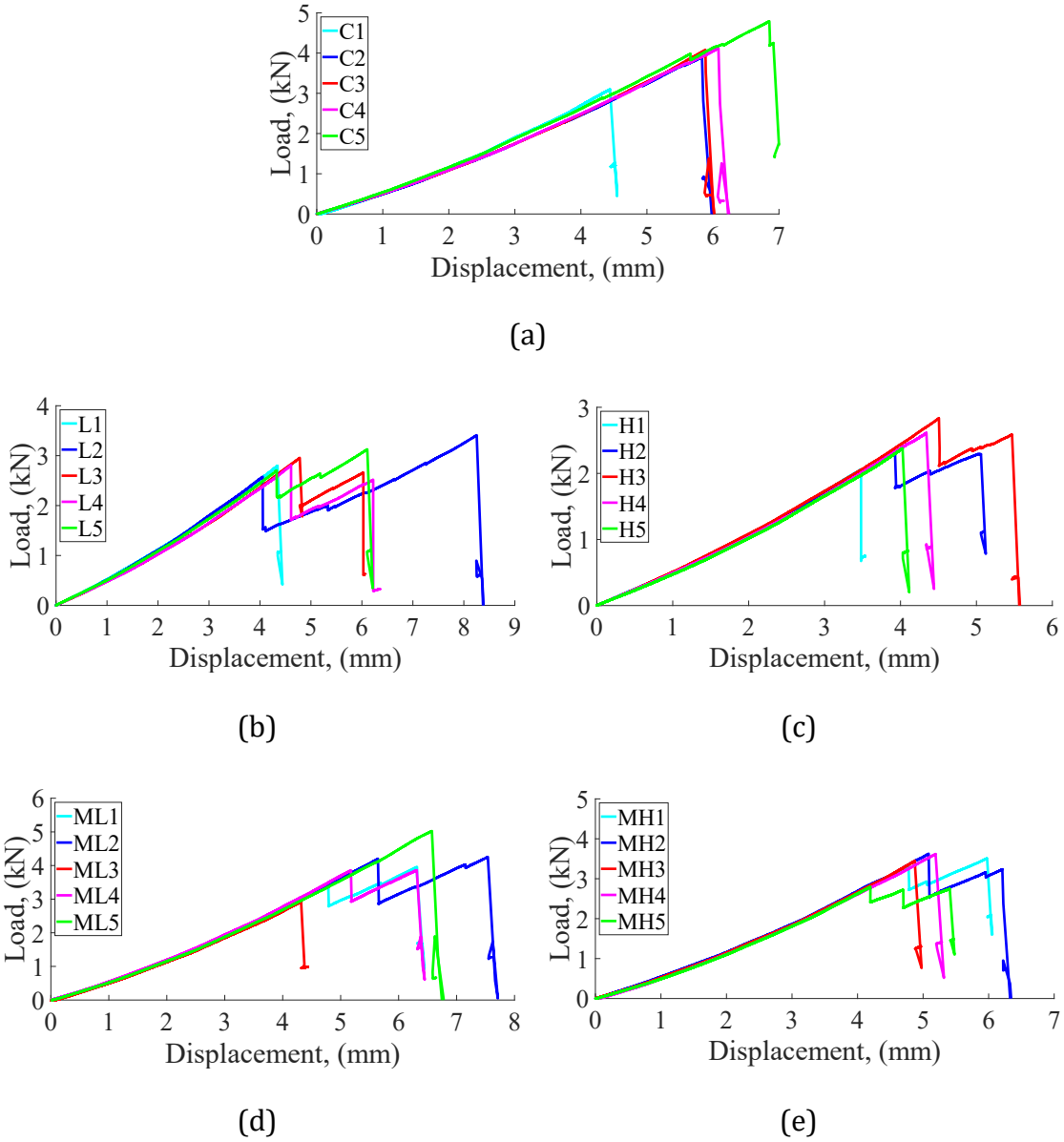

Figure 3.6: Experimental load-displacement curves: (a) unpinned samples, (b, c) 0.27% and 0.54% carbon-fibre Z-pinned samples, (d, e) 0.27% and 0.54% metal Z-pinned samples.

In order to compare the stiffness of different types of samples, which is the linear-part slope of load-displacement curves, one curve from each group was selected and plotted in Figure 3.7. It shows that the curve slopes of unpinned and Z-pinned

samples are very close, thus the presence of Z-pins up to 0.54% density here has negligible effect on the bending stiffness of the curved laminate.

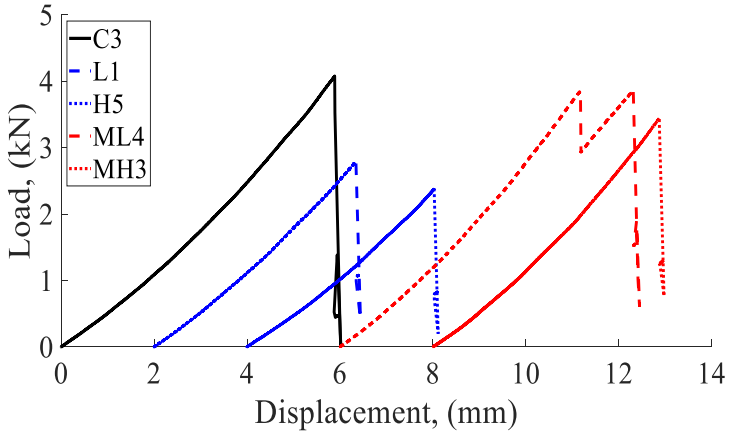

Figure 3.7: Load-displacement curves comparison with displacement offset for clarity.

3.3.2.2 Failure modes

For the unpinned samples, small edge cracks appeared near the outer surface, but they did not cause a measurable load drop, as shown in the insets P1 and P2 of Figure 3.8(a) and P1 of Figure 3.8(b). Some of these edge cracks did not propagate across the width direction and there was no load drop observed in the load-displacement curves such as the sample C3 in Figure 3.8(a). However, some of the small initial cracks led to delamination onset at the top plies through the specimen width, and this resulted in an observable load drop, as shown in insets P2 and P3 in Figure 3.8(b) of sample C4. The generation of these stable or slowly propagating cracks near the outer surface are discussed later in the next chapter with the aid of FE model data. The final load drops are all due to the catastrophic delamination in the middle region, as shown in P3 of Figure 3.8(a) and P4 of Figure 3.8(b).

Regarding the Z-pinned samples, only two samples have the cracks near the top surface, i.e. H2 and ML4, as shown in Figure 9.3 and Figure 9.4 in the appendix. Two main failure modes are observed. Delamination occurred near the inner surface of some samples, resulting in a first load drop, but the specimens did not fail completely and were still able to sustain further loading until failure in the

middle through-thickness region, such as samples L3 and H3 in Figure 3.9(a, c) and samples ML1 and MH1 in Figure 3.10(a, c). The structure became more compliant after the first load drop, as a few plies near the inner surface were partially debonded from the laminate.

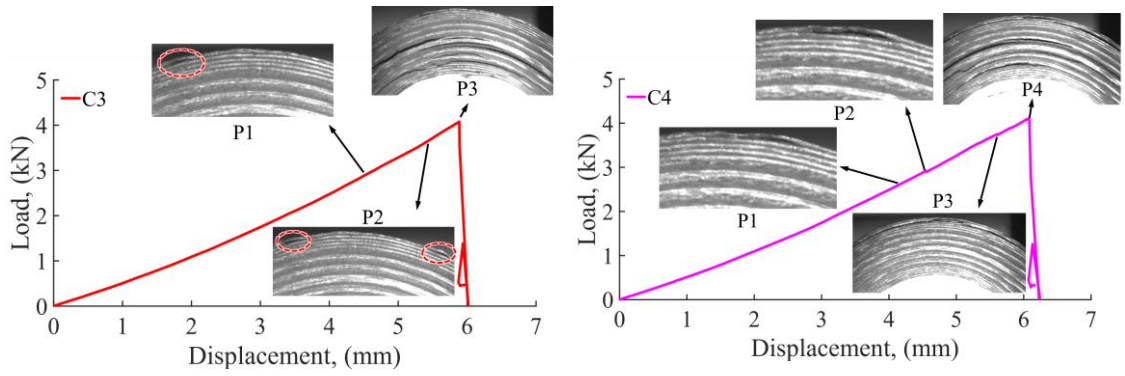

(a) (b)

Figure 3.8: Failure images of unpinned samples (Note: the plot colour of each sample is consistent with Figure 3.6).

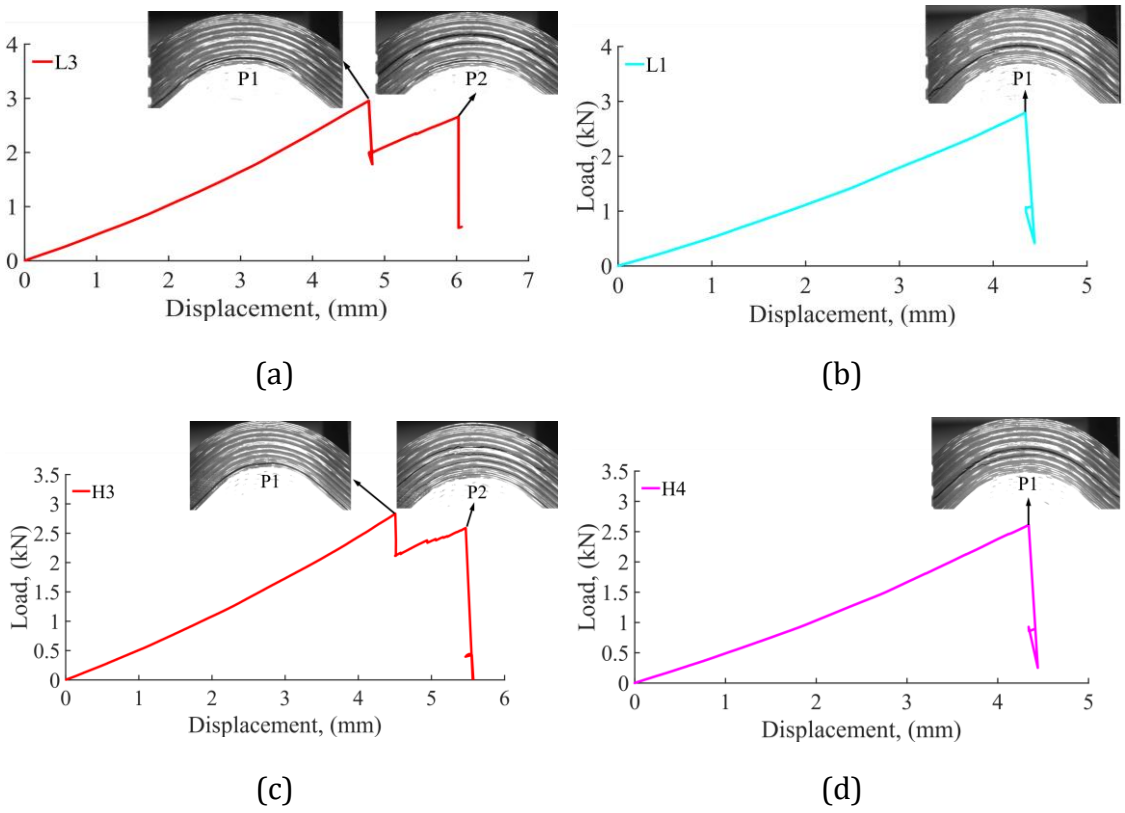

(a) (b)

(c) (d)

Figure 3.9: Failure images of carbon-fibre Z-pinned samples (Note: the plot colour of each sample is consistent with Figure 3.6).

On the other hand, some of the Z-pinned specimens did not show the near-inner-surface delamination before the catastrophic delamination in the middle through-thickness region, such as samples L1 and H4 in Figure 3.9(b, d) and samples ML3 and MH4 in Figure 3.10(b, d). The failure photos of all remaining samples are provided in the appendix from Figure 9.1 to Figure 9.5.

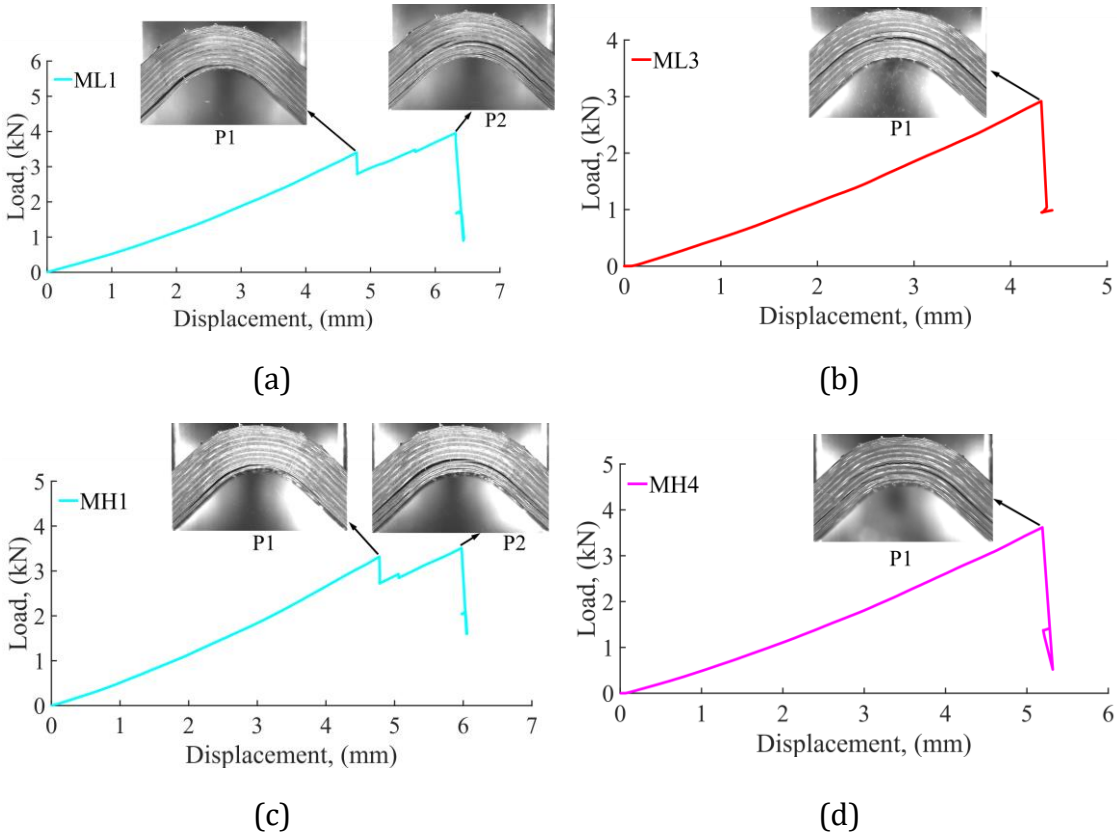

Figure 3.10: Failure images of metal Z-pinned samples (Note: the plot colour of each sample is consistent with Figure 3.6).

3.3.2.3 Through-thickness tensile strength

The Curved Beam Strength (CBS) and TTS can be calculated according to the ASTM D6415/D6415M-06a standard with the following equations [79]:

$$CBS = \left(\frac{P}{2w\,cos(\varphi)}\right)\left(\frac{d_x}{cos(\varphi)} + (D+t)\,tan(\varphi)\right) \quad (3\text{-}1)$$

$$d_y = d_x\,tan(\varphi_i) + \frac{D+t}{cos(\varphi_i)} - \Delta \quad (3\text{-}2)$$

$$\varphi = sin^{-1}(\frac{-d_x(D+t) + d_y\sqrt{d_x^2 + d_y^2 - D^2 - 2Dt - t^2}}{d_x^2 + d_y^2}) \quad (3\text{-}3)$$

$$TTS = \frac{3 \cdot CBS}{2t\sqrt{r_i r_o}} \quad (3\text{-}4)$$

The variables appearing in the equations above are shown in Figure 3.11. P is the failure load. The roller diameter D is 20 mm. φ is the angle between the horizontal direction and the specimen legs in degree, and the initial value φ_i equals to 45°. d_x and d_y are the distances between the same-side top and bottom rollers in the horizontal and vertical directions, respectively. d_x equals to 16 mm. Δ is the relative displacement in vertical direction. r_i and r_0 are the specimen's inner and outer radii. w and t are specimen width and thickness.

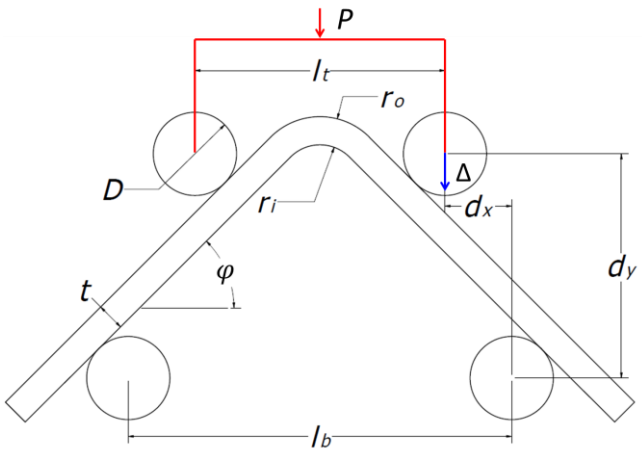

Figure 3.11: Test set-up parameters

Two TTS values are calculated here, corresponding to the first observable load drop (e.g. inset P2 of Figure 3.8(b)) and the ultimate failure load, respectively. The experimental results are summarised in Table 3.1. The coefficient of variation for mechanical testing in composites typically exhibits a range of approximately 10% [75,78]. This level of variation is considered normal and is consistent with the testing scatter observed in Table 3.1.

The TTS mean values of unpinned and Z-pinned samples were compared in the chart, with standard error bars in Figure 3.12. A clear trendline was obderved for the TTS of five types of samples. The first load-drop TTS of 0.27% and 0.54%

carbon-fibre Z-pinned specimens are 0.5% higher and 5.6% lower than the unpinned ones. The metal pins have a significant improvement on the first load-drop TTS, i.e. 35.4% and 17.5% higher at 0.27% and 0.54% areal densities, respectively.

Table 3.1: Experimental results of through-thickness tensile strength, unit: MPa, (Note: '-' means this sample only has one observable load drop.).

	1	**2**	**3**	**4**	**5**	**Mean**	**C.V. (%)**
C-1st TTS	-	46.94	-	58.00	57.16	54.03	11.40%
C-ult. TTS	61.65	73.57	76.78	76.93	85.60	74.90	11.60%
L-1st TTS	-	51.17	57.62	55.09	53.36	54.31	5.00%
L-ult. TTS	55.96	56.92	49.39	46.29	57.59	53.23	9.50%
H-1st TTS	-	46.78	55.20	-	-	50.99	11.70%
H-ult. TTS	41.90	43.96	48.62	51.41	47.81	46.74	8.10%
ML-1st TTS	66.31	79.12	-	74.08	-	73.17	8.82%
ML-ult. TTS	72.55	74.17	57.99	70.75	90.76	73.25	15.96%
MH-1st TTS	64.75	69.95	-	-	55.79	63.50	11.28%
MH-ult. TTS	65.21	59.45	67.04	69.55	52.21	62.69	11.07%

Regarding the ultimate-load-drop TTS, carbon-fibre Z-pinned samples are 29% and 38% lower than unpinned specimens, and the metal pinned samples are 2.2% and 16.3% lower than unpinned specimens respectively.

In summary, the used metal pins behave better than carbon-fibre pins on the TTS, and they have a notable enhancement on the first load-drop TTS. On the other hand, the scatter of ultimate TTS values for carbon-fibre Z-pinned samples is the smallest compared with unpinned and metal pinned specimens, pointed out by the coefficient of variation in Table 3.1 and the standard error bars in Figure 3.12.

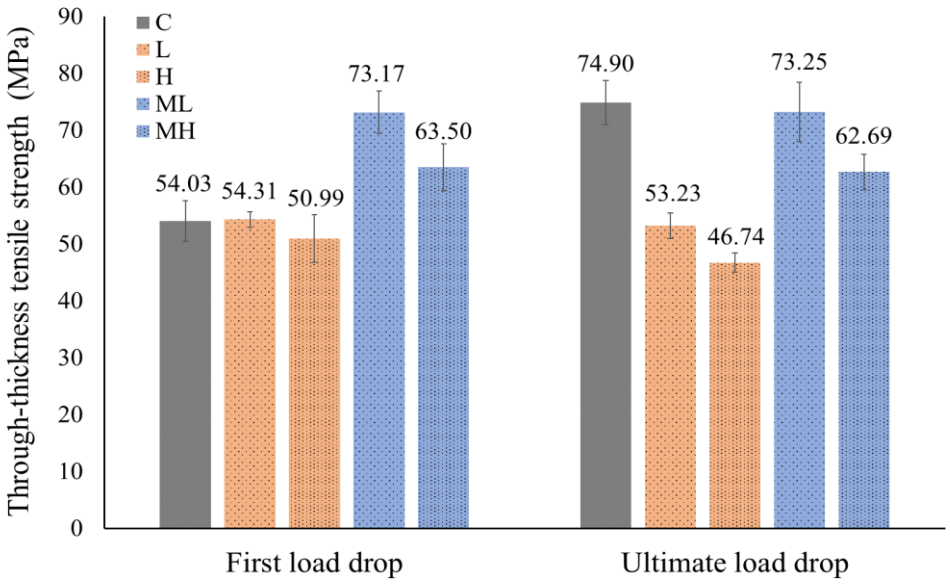

Figure 3.12: Comparison of through-thickness tensile strength.

3.4 Results discussion

3.4.1 Failure of pins

The bridging behaviour of T300/BMI Z-pins is briefly reviewed below, before looking into the Z-pin failure modes of tested specimens. When studying the Z-pin bridging mechanisms, the most commonly used test set-up is inserting a single pin into a square block with a thin layer of release film in the middle plane, then separating the block at different loading angles to simulate the delamination from mode I, mixed mode to mode II. Typical load-displacement curves of single T300/BMI carbon fibre composites pin under pull-out (mode I) and shear (mode II) loading are given in Figure 3.13(a, b).

For mode I dominated loading, the pin debonds from the laminate after the stretching period, then is gradually pulled out in a nonlinear stage. Note that the peak load drop may not be observed if the pin/laminate bonding was significantly weakened due to post-cure cool-down. In mode II dominated loading, the pin deforms locally until it eventually fails catastrophically. The failure mode of T300/BMI Z-pins under mixed mode loading is a combination of the mode I pull-

out and mode II shear rupture with a transition between them, as shown in Figure 3.13(c). The pin failure mode in the transition region is uncertain.

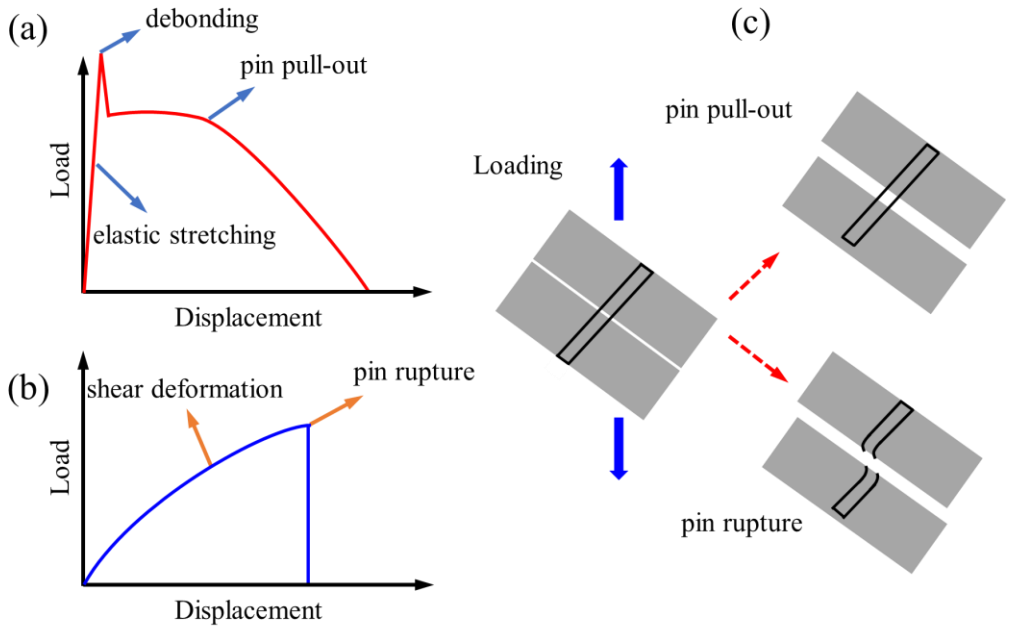

Figure 3.13: Schematic illustration of Z-pin bridging and failure modes: (a) mode I bridging curve, (b) mode II bridging curve, (c) pin failures under mixed mode.

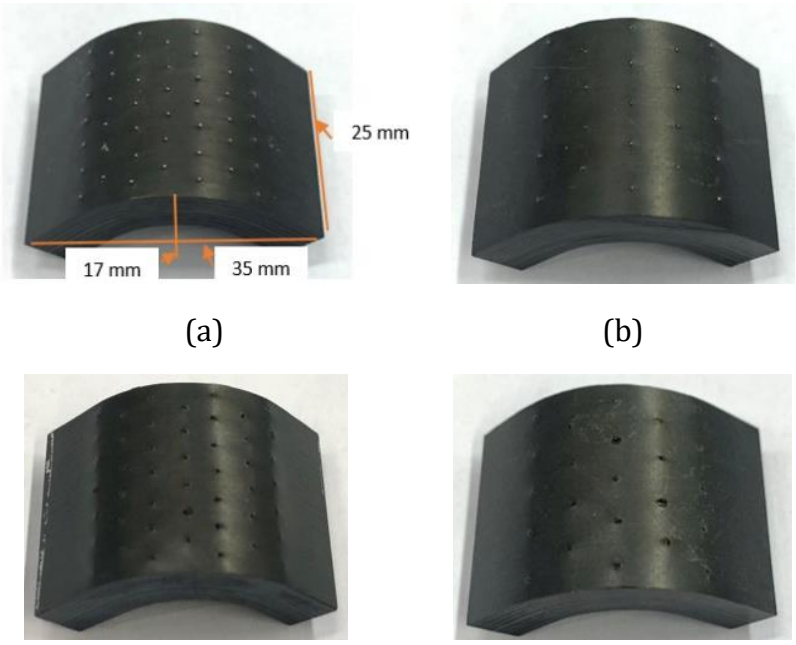

Figure 3.14: CT scanned samples (a) MH1, (b) ML1, (c) H4, (d) L3.

In order to examine the failure mode of pins inside the tested samples, not visible during the test, the curved sections were scanned with a modified 225 kVp Nikon/Xtek HMX X-Ray CT scanner. The CT scan work was supported by the EPSRC-funded NXCT program (grant no. EP/T02593/X/1) and carried out at the University of Southampton. The legs of samples were trimmed off to reduce the scanning size. One sample from each group was scanned, as shown in Figure 3.14.

As the metal causes the x-rays to scatter, it is difficult to distinguish the failure of pins from the CT scan images, as shown in Figure 3.15.

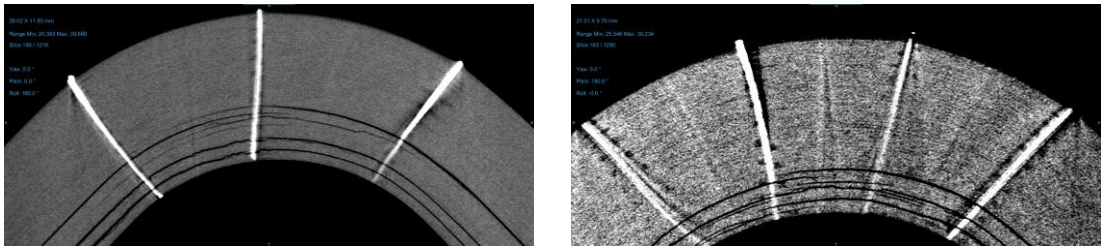

(a) (b)

Figure 3.15: CT scan images of metal Z-pinned specimens (a) ML1, (b) MH1.

Regarding the carbon-fibre Z-pinned samples, the pin and laminate materials are similar, and the contrast from different linear attenuation coefficients of constituents is small [81]. Thus, the tested coupons were soaked in a zinc iodide penetrant bath for 2 days before the scan to more clearly observe the cracks [82].

The CT scan images of carbon-fibre Z-pinned specimens show that 3 out of 23 pins of the 0.27% pinned sample were only partially broken or intact, and the remaining ones were ruptured as shown in Figure 3.16(a). All the 46 pins of the 0.54% Z-pinned sample were ruptured (Figure 3.16(b)).

The middle column pins are in principle pure mode I loaded. Their fracture is mainly because of two reasons: 1) The laminate is relative thick (6.75 mm), and the tensile failure stress of the pin is lower than the interfacial shear stress due to the long bonding/friction area; 2) The pin misalignment induces transverse shear stress on the pins. The side-column pins are under the mixed mode. They were fractured with an obvious shear deformation due to the sliding of adjacent plies such as insets (1) and (3) in Figure 3.16(b).

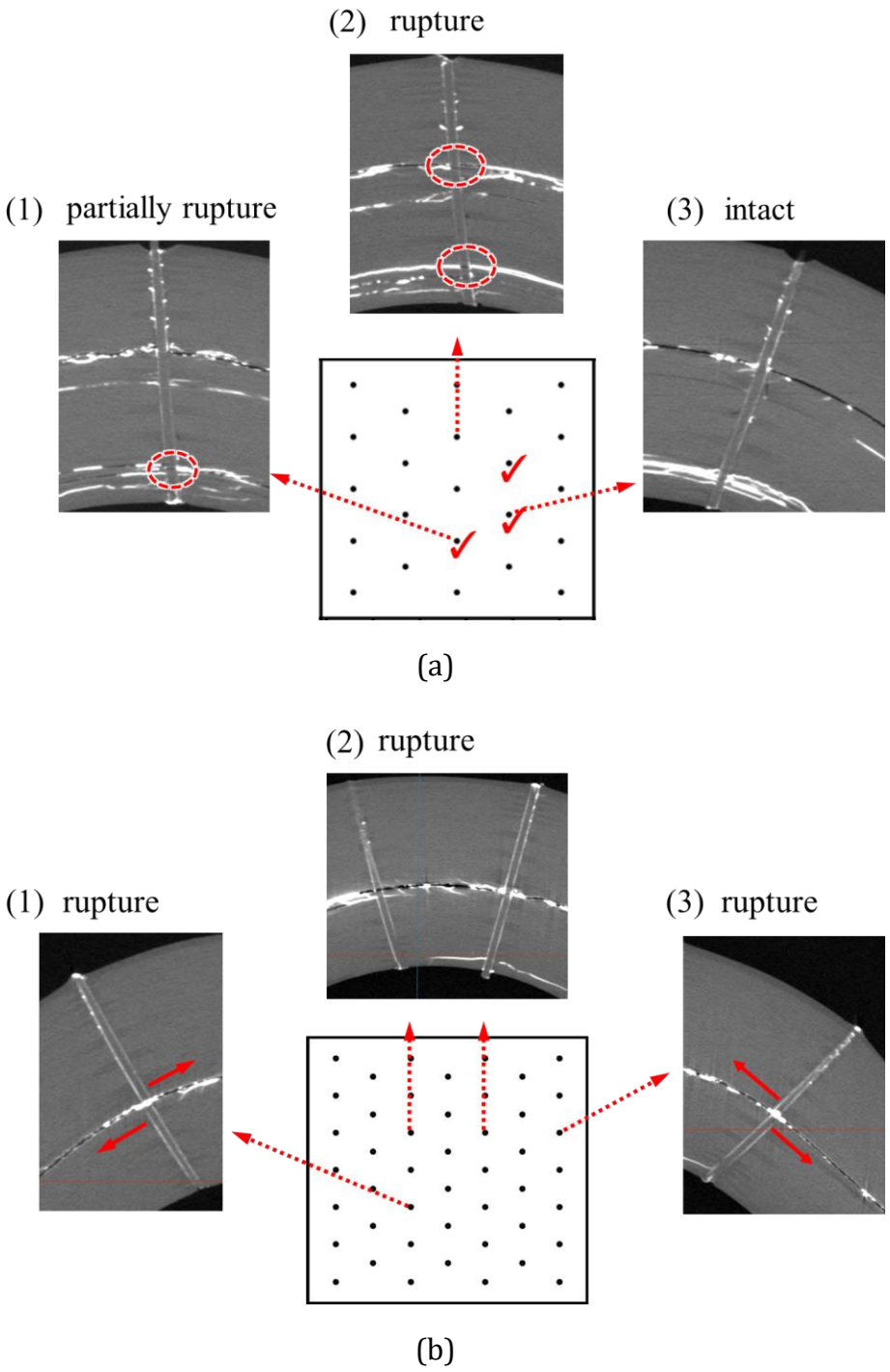

Figure 3.16: CT scan images of tested Z-pinned specimens and top view of specimen pinned region: (a) 0.27% Z-pinned, (b) 0.54% Z-pinned (Note: '✓' is the symbol of partially broken or intact pins.).

The relative offset angles ζ and ψ, which represent the misalignments of the pin from the normal and length direction, can be calculated from the in-plane

misalignment angles obtained from CT scan images [41]. For high-density carbon-fibre Z-pinned specimens, the average values of ζ and ψ were found to be 8.76° and 11.40°, respectively. These values fall within the typical range of less than 15°, indicating that the specimen's misalignments are within acceptable limits.

In summary, Z-pins are effective in resisting crack propagation in the previous research, because energy was dissipated due to the Z-pin bridging process (pull-out or rupture). However, a curved beam under the four-point bending test is in principle a crack initiation case, dominated by the interlaminar tensile stress. Once the crack was initiated in the critical region, it propagated very fast, and the Z-pins were only pulled out at a very small length or ruptured. The failure of pins is also related with their loading mode-mixities. This will be examined in the following chapter with the aid of FE modelling.

3.4.2 Effects of pins

The reduction of TTS in this study could be attributed to the microstructural features caused by the pins, such as fibre waviness, fibre breakage, and stress concentrations around the holes. The pins also have an influence on the residual stress after the cool-down process.

3.4.2.1 Pin volume fraction

The TTS decreases with the pin volume fraction, which follows a similar trend observed for reductions in in-plane properties such as tensile, compression, and bending strengths [30–33]. A higher volume fraction results in more holes with high stress concentrations, making them prone to crack formation. In the curved region, the pinning areal density increases from the outer surface to the inner surface, increasing the likelihood of near-inner-surface delamination. Pin misalignment could also decrease the distance between adjacent pins near the inner surface, which varies from pin to pin and from specimen to specimen, leading to two different failure modes of Z-pinned specimens.

3.4.2.2 Pin material

The metal Z-pinned specimens have higher TTS at each areal densities, compared with carbon-fibre pinned samples. The difference could be due to the following reasons. 1) the inner diameter of metal pin measured from the microscope image is 0.16 mm, which is smaller than that of the carbon-fibre pin (0.28 mm), although their outer diameters are close (Outer diameter of the metal pin is 0.23-0.26 mm). The specimens with thin pins have higher curved beam strength than those with thick pins, as reported in Ref. [9]. The in-plane strength loss is also smaller for thinner pins [30–33]. 2) the metal pin has surface diamond particles locked into the laminate, resulting in a higher interfacial friction force at the pin/laminate interface than the carbon-fibre pin. This interfacial force is effective in increasing the peak load under mode I [83] and lap joint shear [84]. In this study, the pins are ruptured. The delamination and pin rupture happen catastrophically and simultaneously. The failure sequence will be examined with the FE models in the following chapter to have a further discussion. 3) the residual stress due to the post-cure cool-down process is different for the metal and carbon-fibre Z-pinned specimens, which will be discussed in the next chapter as well with the aid of the FE models.

3.4.2.3 Discussion

As mentioned in the introduction, Ref. [9] reported an increase in the curved beam strength of a laminate with grooved metal pins. When the load-displacement curve in Fig. 10 from Ref. [9] is analysed and the TTS is calculated, it is found that the TTS of unpinned specimens and 0.5%, 1%, and 2% Z-pinned specimens (with a 0.3 mm diameter) were approximately 46 MPa, 56 MPa, 56 MPa, and 65 MPa, respectively. It is important to note that the measured TTS is not exactly the same but equivalent to the material's transverse tensile strength. The transverse tensile strength of the prepregs used in Ref. [9] was 61 MPa. The TTS of the unpinned specimens is much lower than the material's transverse tensile strength. Although the Z-pinned specimens show an improvement in TTS, the value is still lower or just comparable to the material's data property. For the study presented in this

thesis, the transverse tensile strength of the IM7/8552 prepreg is 64 MPa, according to Hexply [80], and 78.4 MPa according to Ref. [85]. The measured ultimate TTS of the unpinned specimen is 75 MPa, which falls within this range and indicates a reliable manufacturing quality and testing set-up. The enhancement in TTS due to Z-pins in Ref. [9] may be due to the low TTS of the unpinned control specimens. Additionally, their material's curing temperature [86,87] is lower than that used the present study, resulting in a lower residual stress level after the post-cure cool-down.

3.5 Conclusions

In this chapter, in addition to the well-explored crack propagation resisting ability of Z-pinning in flat panels, the effects of Z-pins on the through-thickness tensile strength of curved laminates were studied experimentally under four-point bend testing. Traditional carbon-fibre pins and steel pins coated with diamond particles were employed in the curved region of the laminate with a zigzag configuration at two areal densities.

Different failure modes were observed for unpinned and Z-pinned specimens using a video gauge and a high-speed video camera. Delamination happened suddenly, and it propagated very fast. CT scan images show that most carbon-fibre pins are ruptured after the test. The pins were only pulled out by a very small length, or ruptured without pullout, and the energy was not able to be dissipated at this short length.

Compared with unpinned specimens, the carbon-fibre pins mainly cause a reduction in the TTS. The metal pins perform better than carbon-fibre pins. They have a notable enhancement on the first load-drop TTS, but their ultimate TTS is still lower compared with unpinned specimens. The loss of TTS could be attributed to the microstructural features introduced by Z-pinning and residual stress generated from the post-cure cool-down process.

In summary, the curved beam under four-point bending is a crack initiation case. Z-pinning was found to be less effective here compared with the well-explored

large crack propagation scenarios. The use of Z-pins could be detrimental. Attention should therefore be paid to Z-pinning when the failure is initiation dominated. In the future, further experimental data is required to explore the impact of various parameters on the TTS. It is also crucial to control the manufacturing and cutting quality of the specimens.

4 NUMERICAL INVESTIGATION OF Z-PINNED CURVED LAMINATE UNDER FOUR-POINT BENDING

4.1 Modelling methodology

High-fidelity meso-scale models were built and run in the Abaqus/Explicit 2018 finite element software. As the experiments reveal a decrease in the through-thickness tensile strength (TTS) of the curved beam, the primary objective of the numerical modelling is to provide insights into the potential factors contributing to this reduction. The focus lies on understanding the effects of Z-pinning on the through-thickness residual stress within specimens following the cool-down stage of cure, as well as identifying the crack initiation locations in Z-pinned specimens and analysing the failure mode of the Z-pins. Since these aspects cannot be directly examined during the experiment, the utilisation of a Finite Element (FE) model becomes essential. The FE model enables a comprehensive analysis of these factors and aids in unravelling the underlying reasons behind the observed reduction in TTS.

As the laminate contains ±45° plies, the model is not symmetrical, making it unsuitable to model a quarter or half of the specimen. Additionally, the curved shape of the laminate and the zig-zag configuration of Z-pinning make unit cell, RVE, and strip models inappropriate. Therefore, the full models were created, with each pin being physically modeled.

The resin pocket is an important microstructural feature which is essential to capture the pin vicinity behaviour. Single-pinned models [67,68] used a star-shaped mesh at the ply level to maintain mesh consistency across plies with varying ply angles. Compared with the single-pinned model, there are two challenges for this study: 1) The geometry is a more complex curved shape with multiple pins. 2) Both the interlaminar delamination of the laminate and the pin/laminate interface failure need to be investigated.

Thus, different meshes were used for each ply, with cohesive element layers modelled between different angled plies of the laminate to simulate the through-thickness delamination. Due to the inconsistencies of meshes for each ply, tie constraints were defined between cohesive element layers and their adjacent plies. The pin/laminate interface was modelled with a general contact. A schematic diagram of the mesh configuration is shown in Figure 4.1.

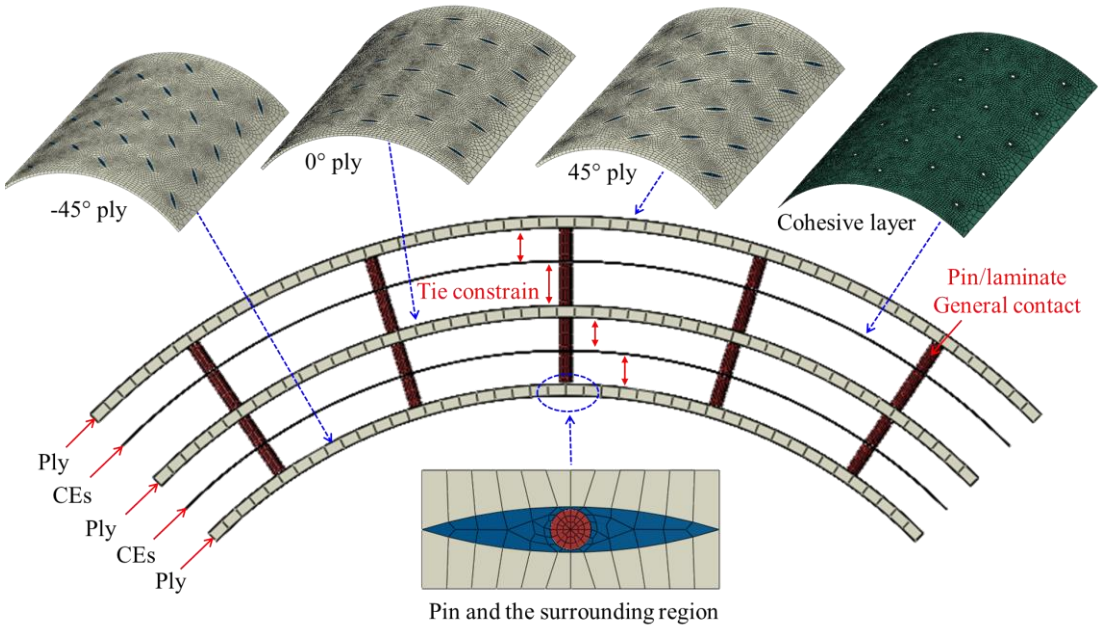

Figure 4.1: Schematic diagram of the mesh configuration.

The models were created with a versatile mesh generation code written by combining Python and MATLAB. A step-by-step flow chart of the modelling strategy is given in Figure 4.2.

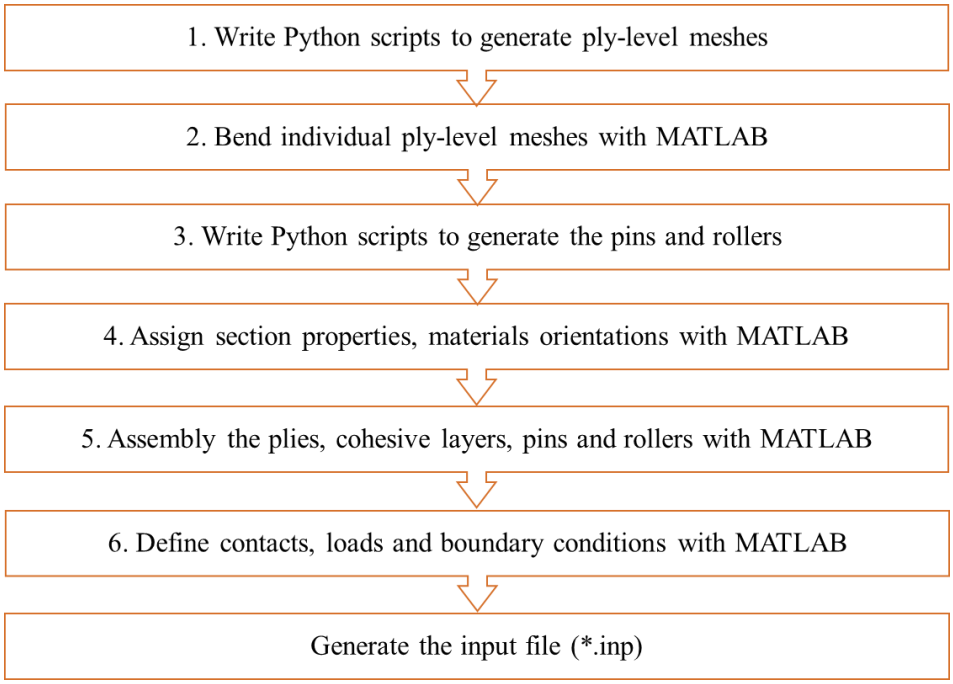

Figure 4.2: Mesh generation process.

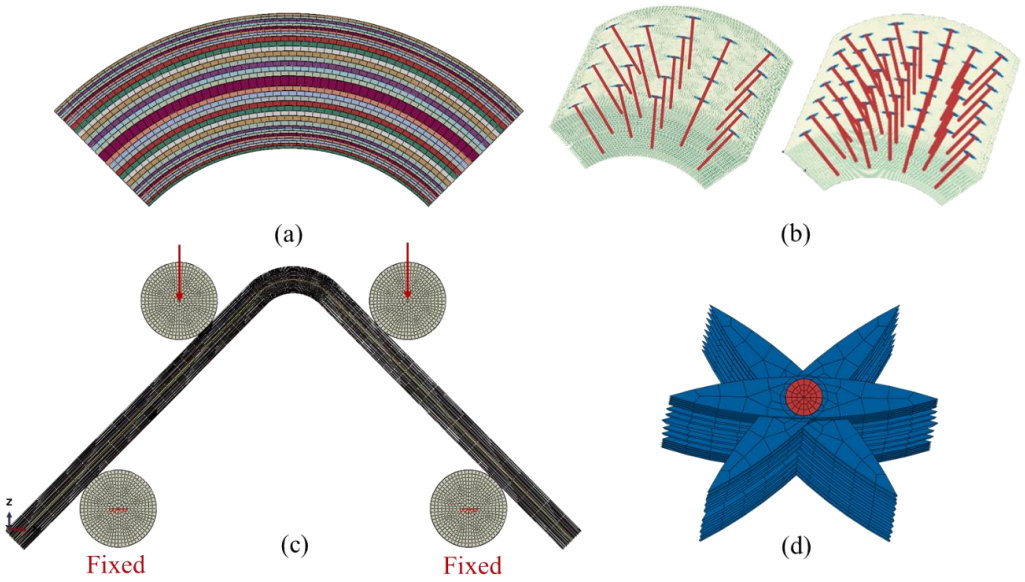

Figure 4.3: FE model (a) section view, (b) 0.27% and 0,54% Z-pinned sections, (c) load and boundary conditions, (d) pin and resin pockets.

The first step is generating flat ply-level meshes for 0°, +45° and -45° plies and cohesive layers with Python scripts, which gives the benefit of controlling the pin number, size, position and spacing. Then, the flat ply-level meshes were imported to MATLAB to bend them to the desired curved shapes. Examples of bent ply-level meshes are shown in Figure 4.1. The final step is assembling individual parts together, defining contacts, loads and boundary conditions, and generating the simulation output file with MATLAB. With this mesh generation code, the user is able to control almost all the input parameters, such as the stacking sequence, material properties, contact definitions, and the geometry and position of pins and rollers. The FE model pictures are shown in Figure 4.3.

4.2 Modelling definition

4.2.1 Material and contact properties

8-node three-dimensional COH3D8 elements were adopted for the cohesive elements, while the remaining parts of the laminate used the single-integration-point brick solid elements (C3D8R). Isotropic material properties were assigned to the resin pockets. Local coordinate systems were created to define the orthotropic material properties of each ply and pin. The input laminate material properties are presented in Table 4.1, taken from Ref. [67,88], in which E is the Young's modulus, G is the shear modulus, ν is the Poisson's ratio, α is the thermal expansion coefficient. The subscripts '1', '2' and '3' represent the fibre direction, transverse direction, and through-thickness direction, respectively.

A bi-linear traction-separation law was adopted for the interlaminar cohesive elements as shown in Figure 4.4. The quadratic nominal stress criterion in Eq. (4-1) was used for the damage initiation. The damage propagation follows a energy-based power law in Eq. (4-2). The damage variable D is defined in Eq. (4-3) [89].

$$\left\{\frac{\langle t_n \rangle}{\sigma_{\mathrm{I}}^{max}}\right\}^2 + \left\{\frac{t_s}{\sigma_{\mathrm{II}}^{max}}\right\}^2 + \left\{\frac{t_t}{\sigma_{\mathrm{III}}^{max}}\right\}^2 = 1 \qquad (4\text{-}1)$$

$$\left\{\frac{G_n}{G_{\mathrm{IC}}}\right\}^{\alpha} + \left\{\frac{G_s}{G_{\mathrm{IIC}}}\right\}^{\alpha} + \left\{\frac{G_t}{G_{\mathrm{IIIC}}}\right\}^{\alpha} = 1 \tag{4-2}$$

$$D = \frac{\delta_m^f(\delta_m^{max} - \delta_m^o)}{\delta_m^{max}(\delta_m^f - \delta_m^o)} \tag{4-3}$$

In the equations, $\sigma_{\mathrm{I}}^{max}$, $\sigma_{\mathrm{II}}^{max}$ and $\sigma_{\mathrm{III}}^{max}$ represent the maximum stress under mode I, II & III loadings, respectively. t_n, t_s and t_t are the normal and two shear stress. G_{IC}, G_{IIC} and G_{IIIC} represent the critical fracture energy under three modes. G_n, G_s and G_t are the work done by the traction in three nominal directions. δ_m^o and δ_m^f denote the relative displacements at the damage initiation and interface failure, respectively. δ_m^{max} is the maximum relative displacement [89]. Cohesive elements utilized in literature for the IM7/8552 material have strengths ranging from 60 MPa to 111 MPa for mode I and from 90 MPa to 137 MPa for mode II, respectively [67,80,88,90–92]. For this study, cohesive element strengths of 90 MPa and 110 MPa were adopted for mode I and mode II, respectively, which fall within the range of values found in the references. The mode I and mode II fracture toughness used were 0.2 N/mm and 1 N/mm, respectively, according to Ref. [67,88,90]. A summary of the input parameters is provided in Table 4.2.

Table 4.1: Input material properties for the laminate [67,88].

Properties of IM7/8552 ply										
E_{11} (GPa)	E_{22} (GPa)	E_{33} (GPa)	G_{12} (GPa)	G_{13} (GPa)	G_{23} (GPa)	ν_{12}	ν_{13}	ν_{23}	α_{11} (°C^{-1})	α_{22} (°C^{-1})
161	11.4	11.4	5.17	5.17	3.98	0.32	0.32	0.436	0	3e^{-5}
Properties of T300/BMI Z-pin										
E_{11} (GPa)	E_{22} (GPa)	E_{33} (GPa)	G_{12} (GPa)	G_{13} (GPa)	G_{23} (GPa)	ν_{12}	ν_{13}	ν_{23}	α_{11} (°C^{-1})	α_{22} (°C^{-1})
144	7.31	7.31	4.45	4.45	2.63	0.25	0.25	0.39	0	3e^{-5}
8552 Resin										
E (GPa)	G (GPa)	ν	α (°C^{-1})							
4.56	1.67	0.37	6.5e^{-5}							

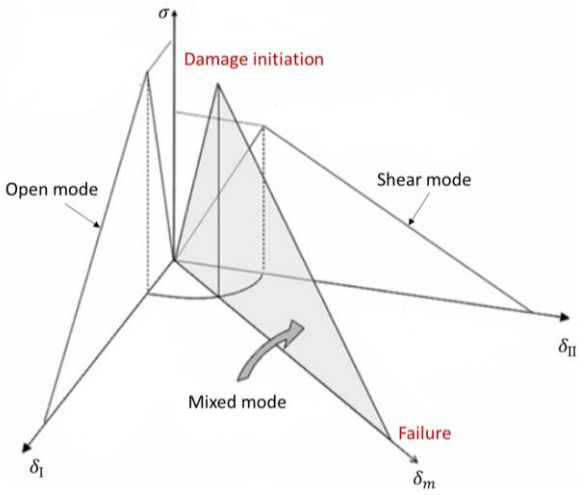

Figure 4.4: Bi-linear traction-separation map of cohesive elements.

Table 4.2: Input properties for interlaminar cohesive elements.

Properties of interlaminar CEs								
G_{IC}	G_{IIC}	G_{IIIC}	σ_I^{max}	σ_{II}^{max}	σ_{III}^{max}	K_I	K_{II}	K_{III}
(N/mm)	(N/mm)	(N/mm)	(MPa)	(MPa)	(MPa)	(GPa)	(GPa)	(GPa)
0.2	1.0	1.0	90	110	110	100	100	100

The pin/laminate interface bonding and friction force were defined with cohesive elements plus a Coulomb friction law in the general contact of Abaqus/Explicit 2018 by selecting the surfaces of pins and surrounding holes. The parameters used for the interface are given in Table 4.3, taken from Ref. [67].

Table 4.3: Input properties for the pin/laminate interface [67].

Properties of pin/laminate interface									
G_{IC}	G_{IIC}	G_{IIIC}	σ_I^{max}	σ_{II}^{max}	σ_{III}^{max}	K_I	K_{II}	K_{III}	μ
(N/mm)	(N/mm)	(N/mm)	(MPa)	(MPa)	(MPa)	(GPa)	(GPa)	(GPa)	
0.01	1.0	1.0	60	90	90	100	100	100	0.8

4.2.2 Load and boundary conditions

The rollers were modelled as rigid bodies and made contact with the laminate via surface-to-surface contacts. The rollers served as the master, and the laminate

acted as the slave, as shown in Figure 4.5 (a). Figure 4.5 (b) shows a mesh top view of one roller and the laminate. Two reference points of the top rollers were used for the loading, and the bottom rollers were fixed (Figure 4.3(c)).

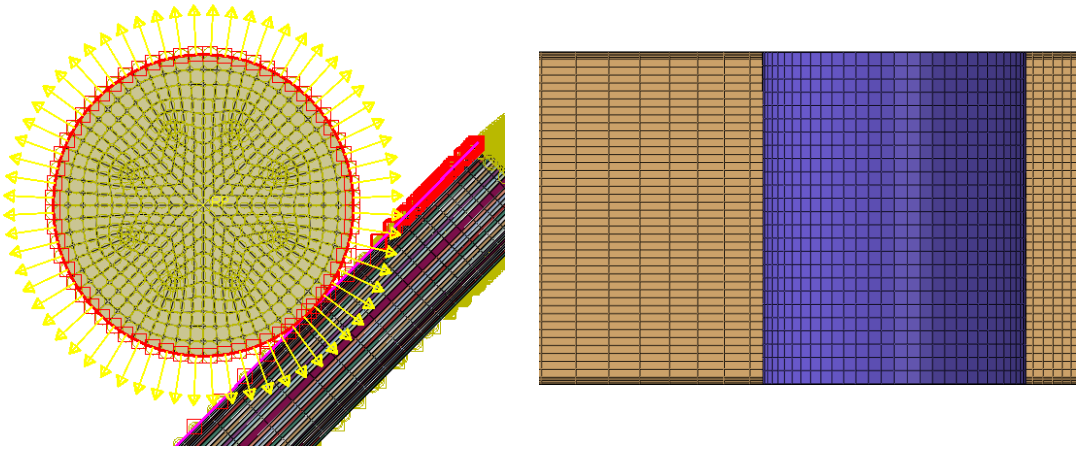

(a) (b)

Figure 4.5: (a) Surface to surface contact for the roller and laminate, (b) top view of roller and laminate mesh.

Two steps were simulated: 1) A temperature field of -160 °C was applied to the model to simulate the cool-down process after cure; 2) After the cool-down step, a smoothed vertical velocity was applied to the reference points of the two top rollers to simulate the loading process. Mass scaling was employed to speed up the simulation without invoking excessive kinetic energy. The time increment step was set as 10^{-6}. To ensure that dynamic effects were negligible and did not affect the failure predictions, the kinetic energy was compared to the internal energy, and the internal energy was found to be significantly greater than the kinetic energy.

4.2.3 Mesh convergence study

For the unpinned model, the mesh configuration for the plies and interlaminar cohesive elements is identical. To account for free edge stress, four narrow strips of fine elements with a width of 0.125 mm were positioned at two edges, as shown in Figure 4.6. In the through-thickness direction, there is one element for each

angled ply block, as shown in Figure 4.3(a). The element size was gradually increased towards the end of each leg to reduce the model size.

Following a convergence study, it was found that the stress of elements in the mid-width plane is not sensitive to the element size. The same result was achieved when the element size was set to 0.6 mm, 1.25 mm and 2.5 mm, respectively. Regarding the cohesive elements, the mesh convergence study is more critical for failure prediction. Two models were simulated, with the element size of the curved section in the length direction being 0.25 mm and 0.125 mm respectively, as shown in Figure 4.6.

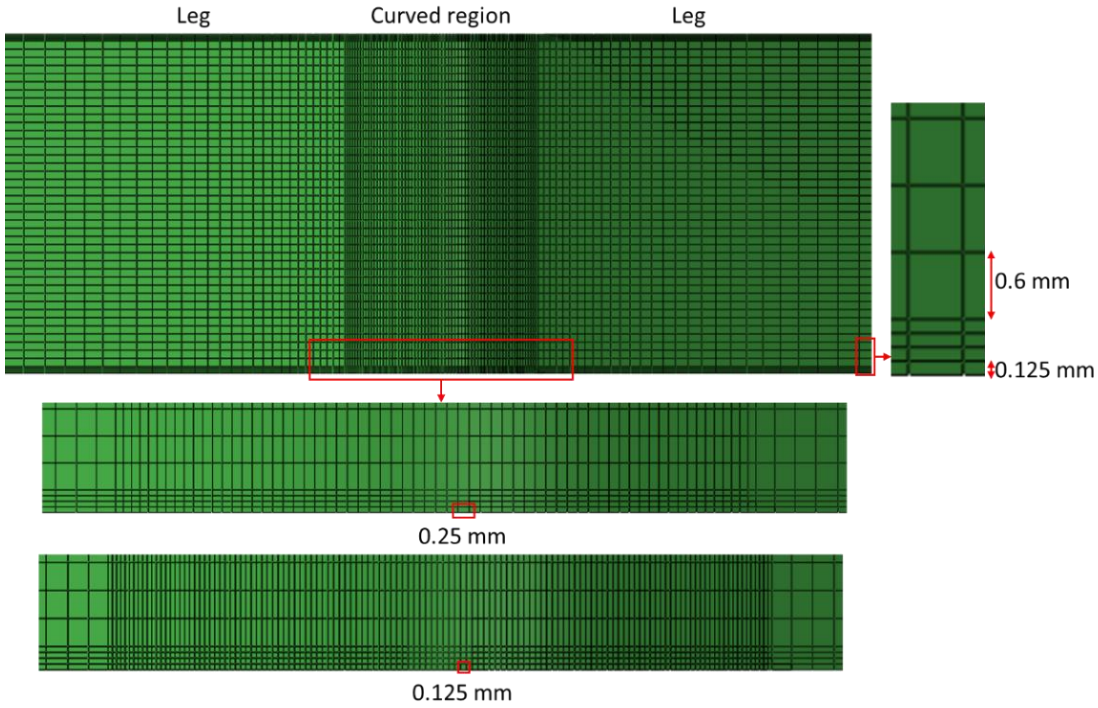

Figure 4.6: Top view of the mesh for the unpinned model.

The modelling result in Figure 4.7 shows that two load-displacement curves almost coincide. Thus, a size of 0.25 mm is sufficient for the cohesive elements of the curved section, which was controlled to be equal to or less than 0.25 mm for both unpinned and Z-pinned models. An example of local meshes for Z-pinned model is give in Figure 4.8.

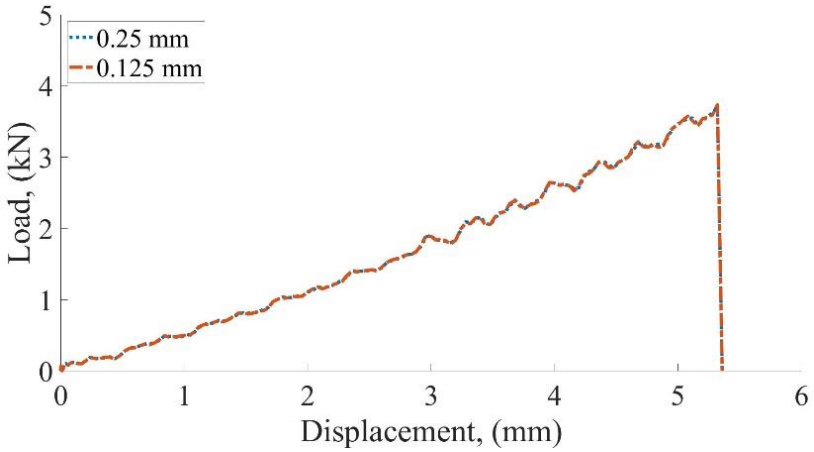

Figure 4.7: Cohesive elements mesh convergence study result.

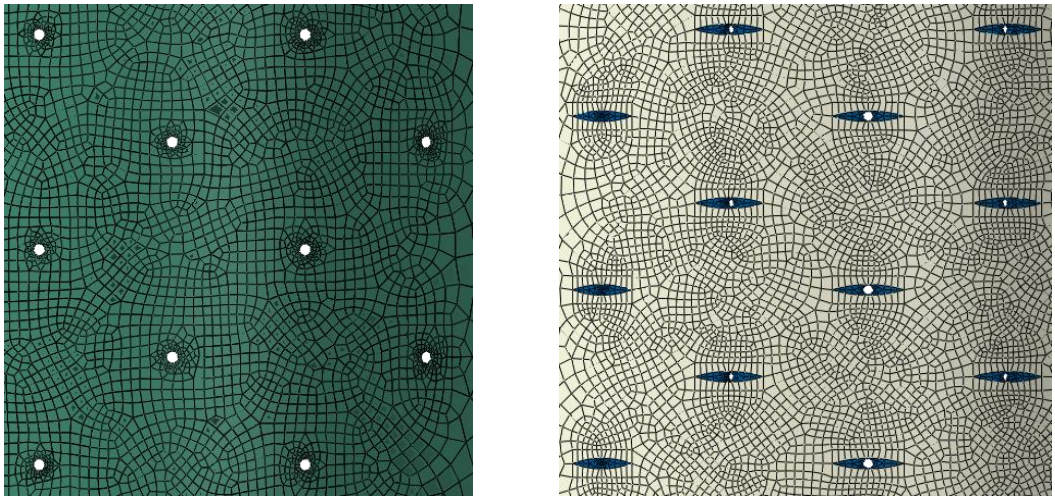

(a) (b)

Figure 4.8: Local meshes of (a) cohesive element layer, (b) 0° ply.

4.3 Result discussion

4.3.1 Unpinned model

4.3.1.1 Free edge stress analysis

As mentioned in the previous experiment chapter, local cracks were observed near the top surface of unpinned specimens at the 0°/+45° and 0°/-45° interfaces, as shown in Figure 4.9.

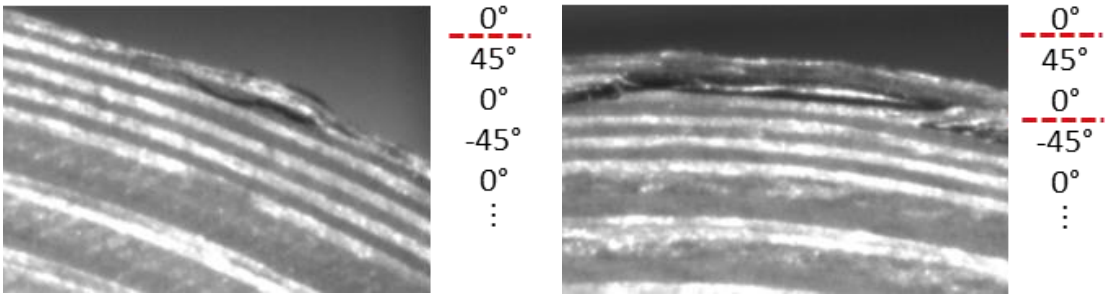

Figure 4.9: Local cracks near the top surface of unpinned specimens (Note: white parts in the photos are 0° plies).

In order to examine if it is due to the high interlaminar stress developed at free edges [78,93], a stress analysis was carried out for the unpinned model in Abaqus/Explicit, which is linear elastic without interlaminar cohesive elements. A mesh convergence study was carried out with fine element sizes. There are two elements in the through-thickness direction for each ply. In the length and width directions, the element sizes are 0.05×0.01, 0.1×0.02, and 0.2×0.04 (unit: mm), respectively. The elements of an edge strip in the centre of the curved section (Figure 4.10) were selected for the quantitative analysis.

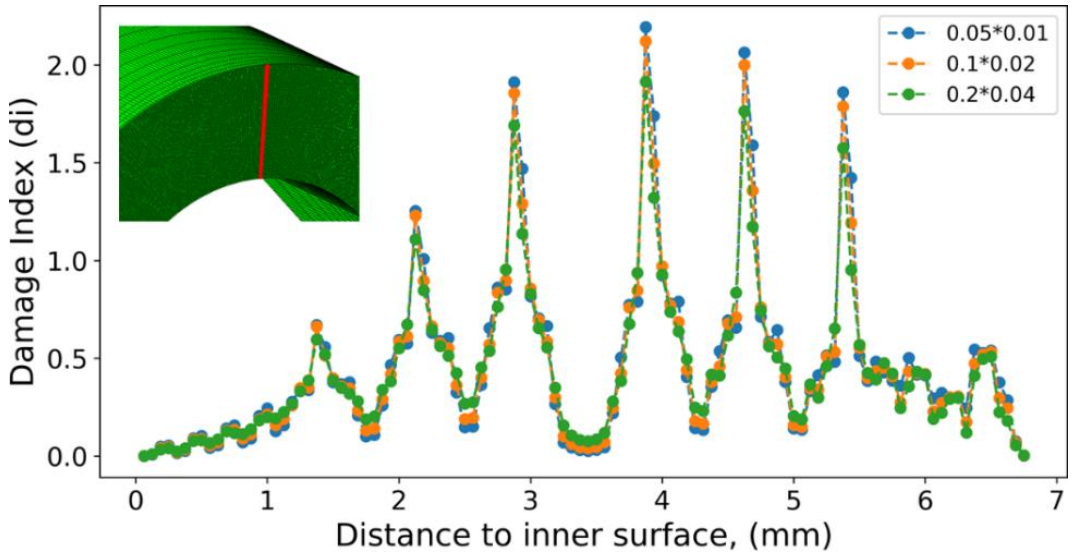

Figure 4.10: Mesh convergence study of an edge strip.

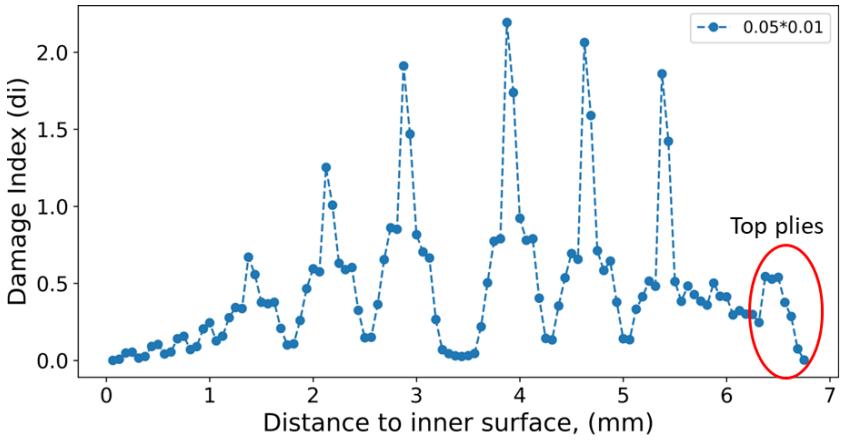

(a)

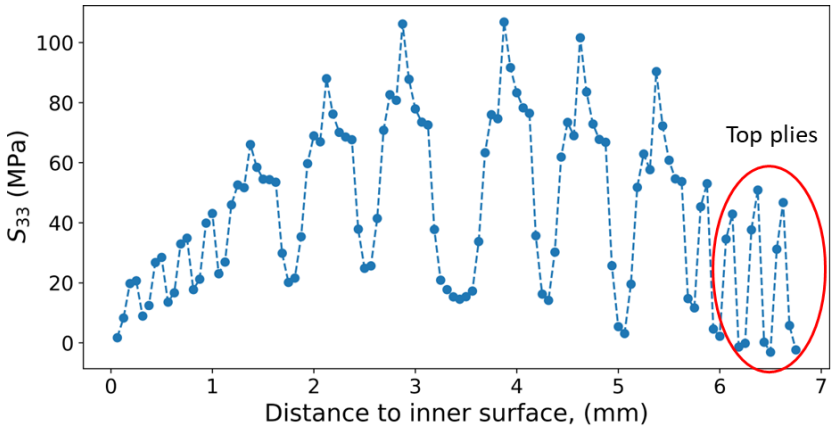

(b)

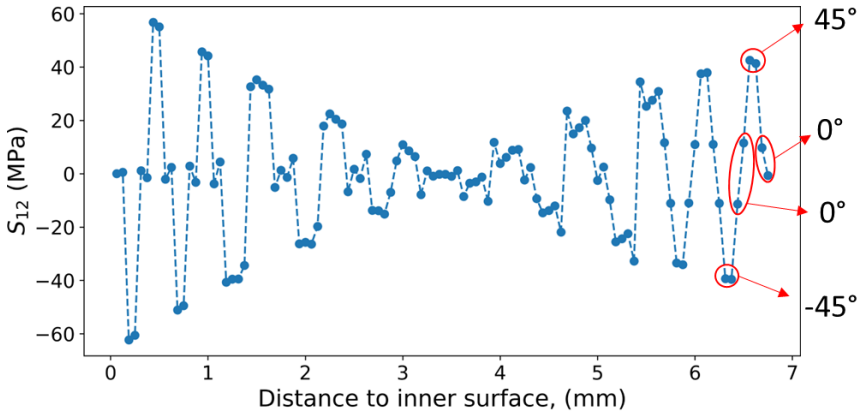

(c)

Figure 4.11: Plots of (a) delamination damage index, (b) through-thickness tensile stress, (c) in-plane shear stress.

Two main failure modes were examined here: delamination and in-plane shear. For the delamination, a damage index *di* was defined with a quadratic law [93–95] by using the through-thickness tensile stress s_{33}, and transverse shear stresses s_{13}, s_{23}, as described in Eq. (4-4). $\sigma_{\mathrm{I}}^{\max}$ and $\sigma_{\mathrm{II}}^{\max}$ are equivalent to the mode I and mode II strength of cohesive elements, and the values used here are also 90 MPa and 110 MPa.

$$di = \left(\frac{s_{33}}{\sigma_{\mathrm{I}}^{\max}}\right)^2 + \left(\frac{\sqrt{s_{13}^2 + s_{23}^2}}{\sigma_{\mathrm{II}}^{\max}}\right)^2 \tag{4-4}$$

As shown in Figure 4.10, the result was found to converge, and the three models have the same trend of stress distribution for the picked edge-strip elements with very little difference between the 0.05×0.01 and 0.1×0.02 models.

The simulation results of the 0.05×0.01 model are plotted in Figure 4.11. Figure 4.11(a) shows that the delamination damage index of the top plies is higher than the bottom plies, but much lower compared with the mid through-thickness region. Four peaks of *di* exist around the mid-plane at +45°$_2$/-45°$_2$ interfaces. The through-thickness tensile stress is plotted separately in Figure 4.11(b). It shows that s_{33} still has the peak value around the mid through-thickness plane, but the values are also high for the top plies.

Figure 4.11(c) gives the distribution of in-plane shear stress s_{12}. It increases from the mid-plane to the inner and outer surfaces. It is high within the top and bottom +45° and -45° plies. Thus, cracks at the top layers are more likely because the in-plane shear failure promotes delamination. While for the inner plies, even if the in-plane shear stress is high, the delamination index is very low, thus didn't generate local cracks there. In addition to the above reasons, manufacturing defects such as wrinkles and voids may promote edge cracks as well.

4.3.1.2 Result discussion

The experimental and modelling load-displacement curves of unpinned specimens are compared in Figure 4.12. It shows that their linear parts agree well. The

predicted failure load is 3.72 kN, which is slightly lower than the average experimental result of 4 kN.

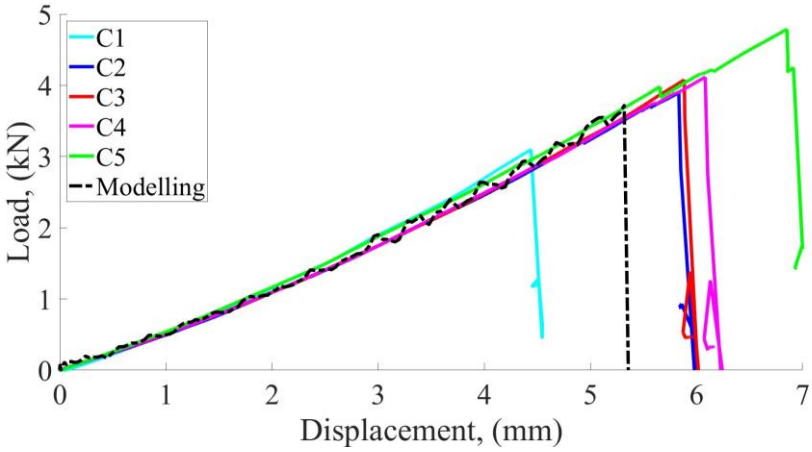

Figure 4.12: Experimental and modelling load-displacement curves of unpinned specimens.

Regarding the failure mode, the model is able to capture the final catastrophe delamination in the mid-region. For instance, as shown in Figure 4.13, the delamination of specimen C1 happens just above the mid-plane at the $+45°_2/-45°_2$ interface, which is the same as the modelling predicted.

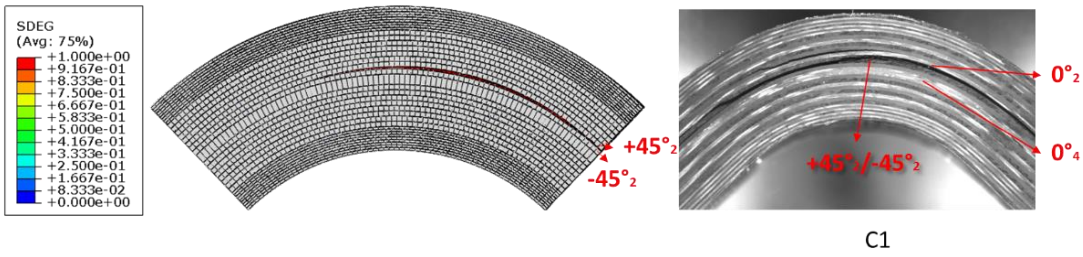

Figure 4.13: Experimental and modelling failure of unpinned specimen.

Since the in-plane failure was not considered in this model, the model is not able to capture the cracks near the top surface. When an across-width delamination happened around the top surface, the plies were relaxed from the laminate, and the specimen became more complaint to carry future loading at a higher displacement. Thus, the predicted failure load of the FE model is lower than the experimental mean value.

4.3.2 Carbon-fibre Z-pinned model

The modelling result of 0.27% and 0.54% carbon-fibre Z-pinned specimens will be discussed in this section to explain the experimental phenomena. The mode-mixities of pins will be analysed first, followed by the residual stress analysis and the failure result discussion.

4.3.2.1 Mode-mixities of Z-pins

With the aid of the FE model, the mode-mixity α of the pins can be calculated. The mode-mixity is defined as the ratio of the crack sliding displacement to the total displacement [41,67,96], and it can be calculated with the following equation:

$$\alpha = \frac{\sqrt{u_1^2 + u_2^2}}{\sqrt{u_1^2 + u_2^2 + u_3^3}} \tag{4-5}$$

in which u_1 and u_2 are the displacements of a pin in the hoop and width directions, while u_3 is the pin axial (i.e. radial) displacement. Considering the displacements taken from the FE model just before delamination occurred, the calculated mode-mixities of side-column pins from the outer surface to the inner surface are plotted in Figure 4.14.

It shows that the mode-mixity α increases from the outer surface to the inner surface, because of the laminate curved shape. The mode-mixity values are consistently above 0.2 and exceed 0.6 for the columns C1& C7 of the high-density Z-pinned specimen, which are the farthest away from the centre of the curved region. The CT scan images in the experiment chapter show that almost all pins were ruptured after the test. In Ref. [41], the same type of pin was tested under a variety of mode-mixities for a single pinned block with a film layer in the middle. It was found that when the mode-mixity is above 0.2, the pin starts to transfer from the pull-out failure to shear-out failure. Although the test configuration in Ref. [41] is different from this study, the effect of the mode-mixity is observed to be the same.

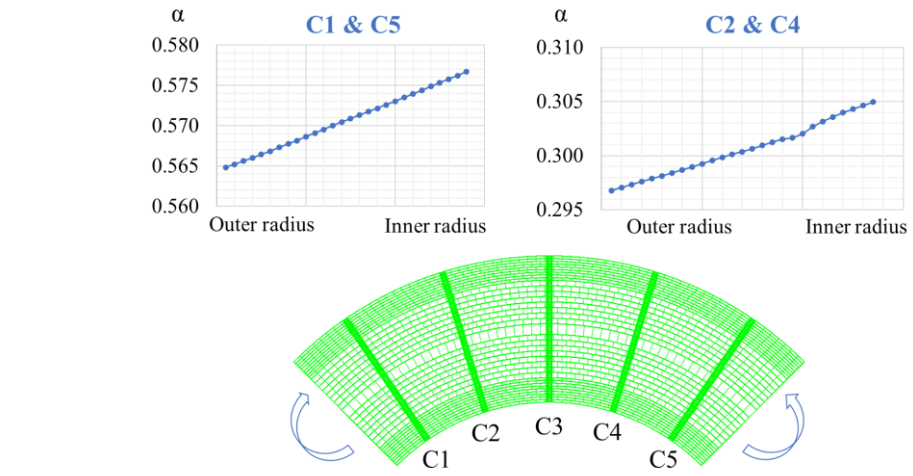

(a)

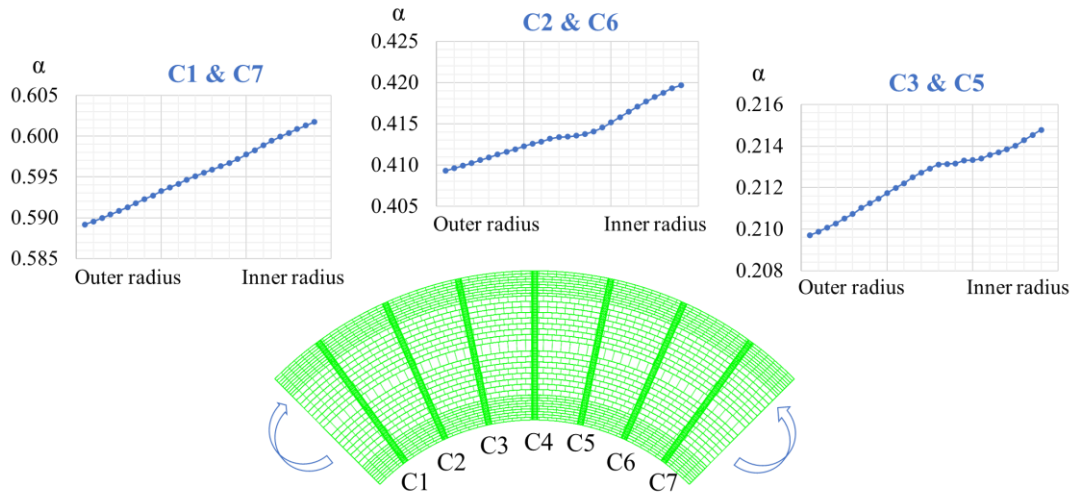

(b)

Figure 4.14: Plot of Z-pin mode-mixities (a, b) 0.27% and 0.54% carbon-fibre Z-pinned models.

4.3.2.2 Residual stress analysis

The modelling result shows that through-thickness tensile stress in the middle section of an unpinned laminate after cool-down is very low (up to 3.6 MPa) as shown in Figure 4.15(a).

After adding pins, the pins tend to oppose the through-thickness contraction of the laminate due to the mismatch between the through-thickness thermal expansion coefficients of the carbon-fibre pin and the host laminate. Thus, in Figure 4.15(b, c),

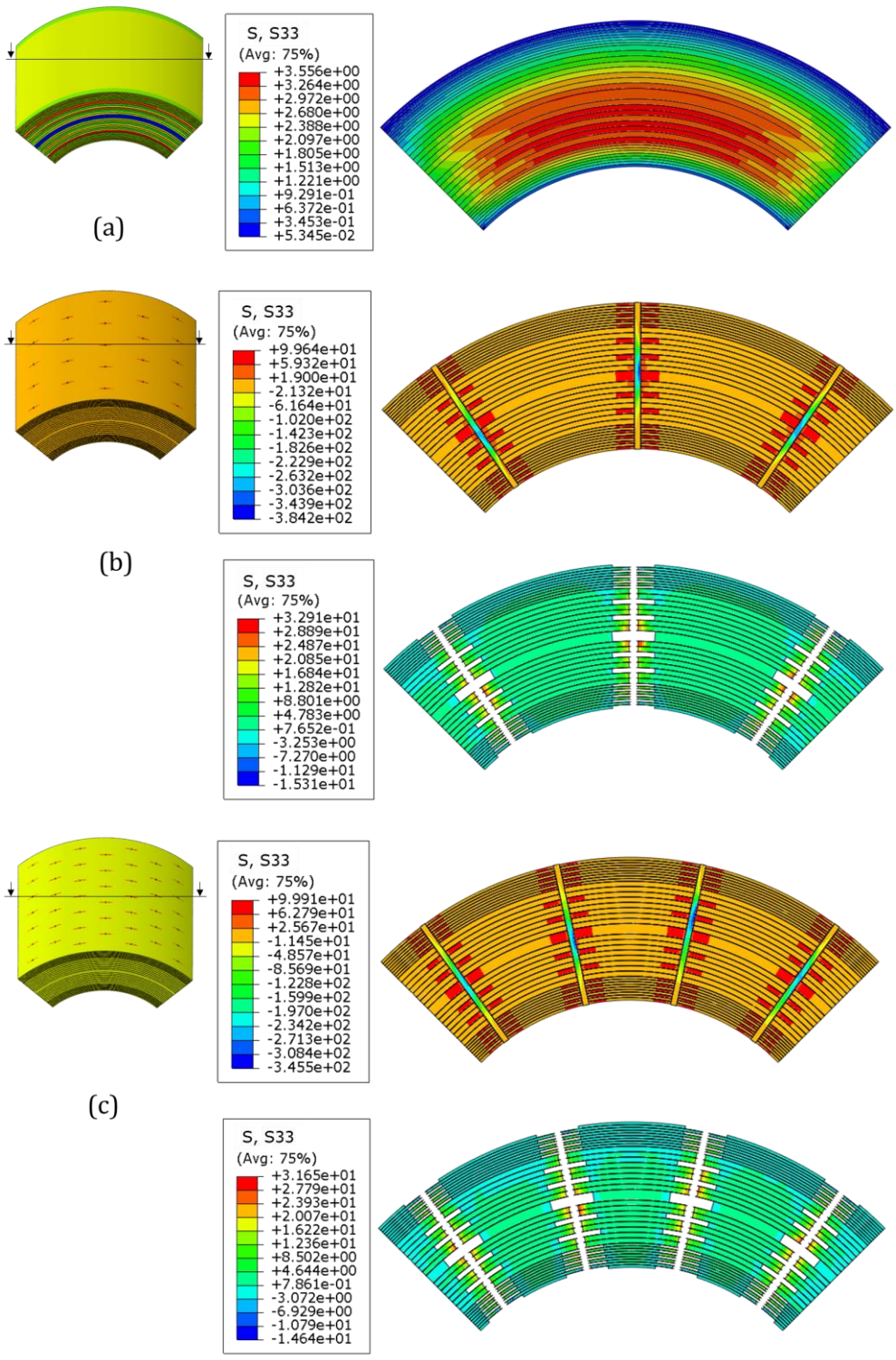

Figure 4.15: Modelling results of through-thickness tensile stress after the cool-down of cure: (a) unpinned, (b, c) 0.27% and 0.54% carbon-fibre Z-pinned (Note: S33 is the through-thickness or radial stress here. Resin pockets and pins are shown and removed respectively in (b) and (c)).

the through-thickness tensile stress in the resin pockets reaches 100 MPa, and consequently the pin is under compression with a stress peak of about -384 MPa. The residual tensile stress in the Z-pinned laminates locally researches 33 MPa in proximity of the resin pockets (see Figure 4.15(b, c) with pins and resin pockets removed).

Figure 4.16 is the damage index plot of the pin/laminate interface after the cure step. It shows that the pins partially debond from the laminate at two ends due to the contraction of the vicinity laminate in the through-thickness direction.

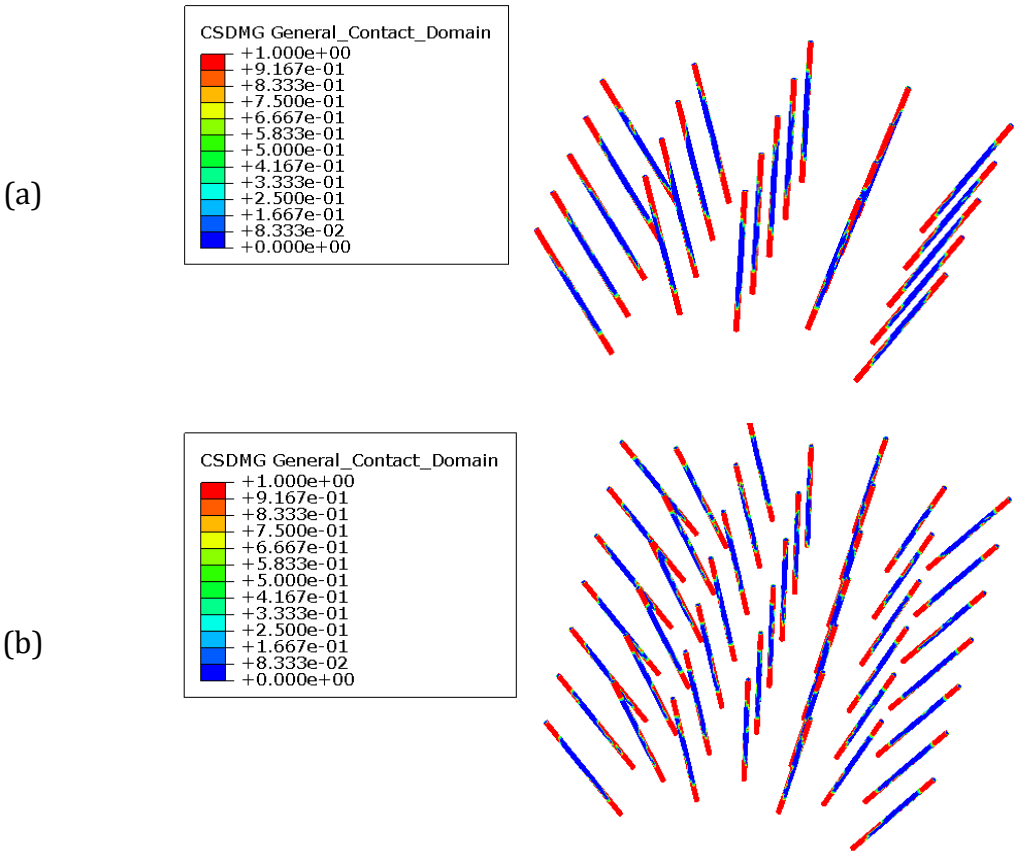

Figure 4.16: Damage index plot of pin/laminate interface after the cure step pins with (a) 0.27% and (b) 0.54% areal densities.

In summary, the presence of Z-pins introduces high residual stress within the laminate and especially around the pins, due to the post-cure cool-down. The delamination observed in Z-pinned laminates is thus expected to initiate close to the pins.

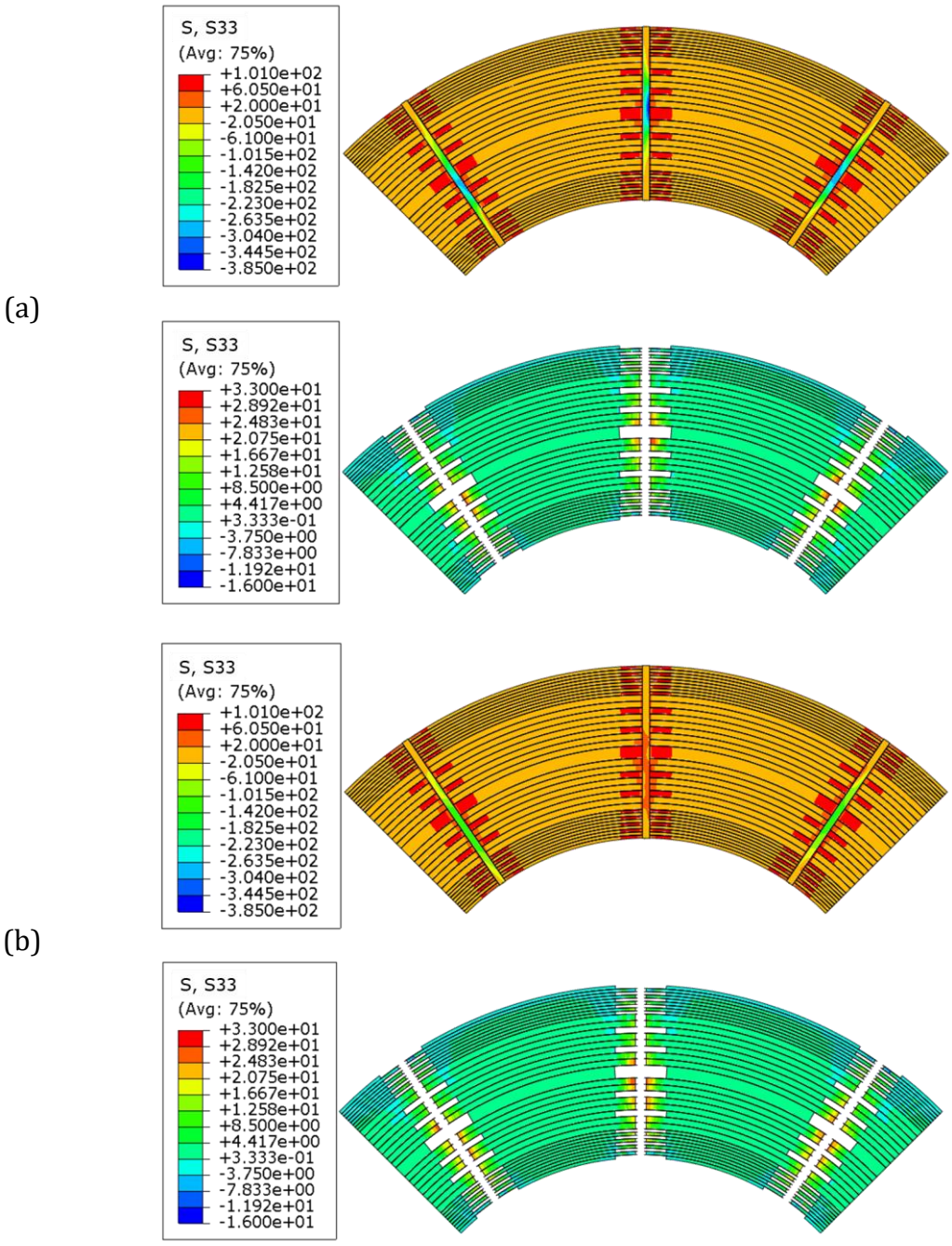

Figure 4.17: Comparison of the through-thickness residual stress of (a) carbon-fibre and (b) metal Z-pinned specimens.

To compare the residual stress of carbon-fibre and metal Z-pinned specimens, another model was simulated by changing the Z-pins' material to steel, with a Young's modulus, Poisson's ratio, and thermal expansion coefficient of 190 GPa, 0.29 and 1.2 e^{-5} $°C^{-1}$, respectively [97]. The results for both carbon-fibre and steel

pins are presented in Figure 4.17, with the scale bar set to be the same for an intuitive view.

For the through-thickness direction, the thermal expansion coefficient of metal pin is closer to the laminate compared with the carbon-fibre pin, while it is opposite for the in-plane direction. The overall residual stress of the laminate is similar in both cases. The through-thickness residual stress of the metal pin (maximum compressive stress of -163 MPa) is much smaller than that of carbon-fibre pin (maximum compressive stress of -384 MPa), because of greater contraction of the metal pin during cool-down. When looking at the images with the pins and resin pockets removed in Figure 4.17, it shows that the residual tensile stress in the carbon-fibre and steel Z-pinned laminates is very close, which locally researches 33 MPa and 32 MPa in proximity of the resin pockets, respectively.

4.3.2.3 Failure analysis

The experimental and modelling load-displacement curves of 0.27% and 0.54% carbon-fibre Z-pinned specimens are compared in Figure 4.18. It shows that the linear parts of the curves agree well. As shown in Figure 4.18, the numerical failure loads of 0.27% and 0.54% Z-pinned models are 2.60 kN and 2.42 kN, respectively, which are close to but slightly smaller than the experimental values.

As mentioned in the experimental chapter, there are two failure modes of Z-pinned specimens: 1) a first load drop near the inner surface due to delamination; 2) only one catastrophic failure in the mid-region. As discussed in the experimental section, inner-surface delamination is expected to be due to the pin misalignment. These features were not included in the model, thus the models only capture the second failure mode with one load drop.

Figure 4.19 shows the modelling predicted and experimentally observed delamination. For the 0.27% Z-pinned model, the captured delamination happens at the $+45°_2/-45°_2$ interface below the mid-plane, which is the same with specimen L1, as shown in Figure 4.19(a). The modelled 0.54% Z-pinned specimen has the delamination at $+45°_2/-45°_2$ interfaces as well. The high-speed camera captures

the sequence of delamination events for specimen H1, as shown in Figure 4.19(b). It shows that the initial delamination starts from the modelling predicted +45°$_2$/-45°$_2$ interface, then propagates to the 0° plies.

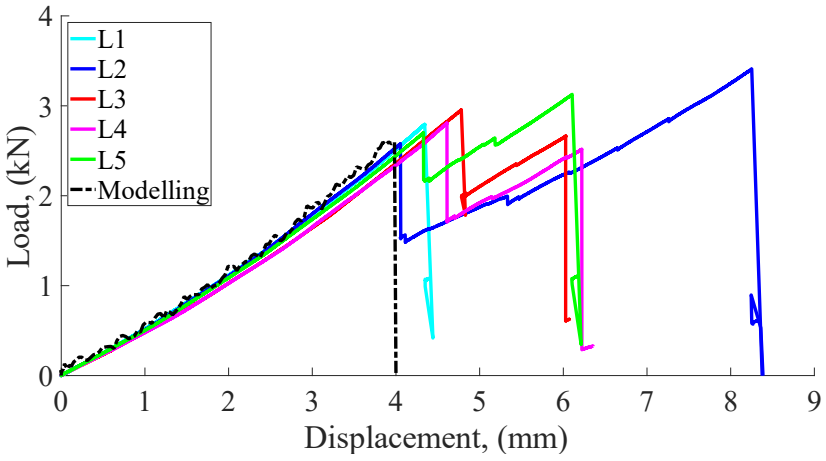

(a)

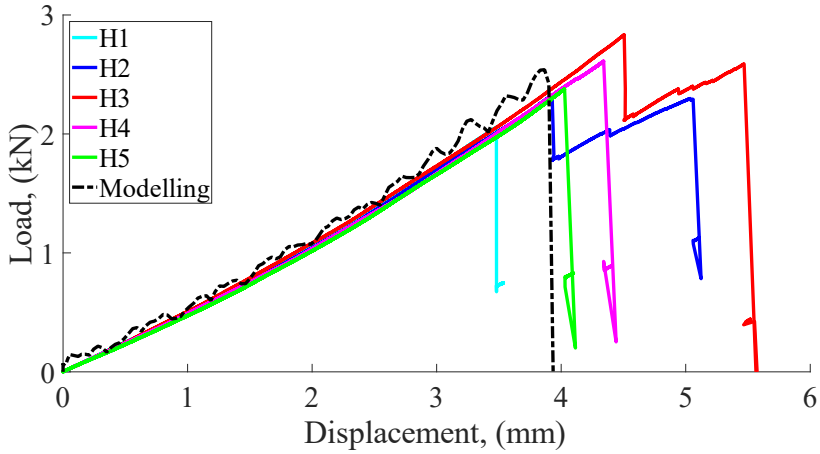

(b)

Figure 4.18: Experimental and modelling load-displacement curves for (a) 0.27% and (b) 0.54% carbon-fibre Z-pinned specimens.

Figure 4.20 shows the top view of the failed cohesive element layers of the 0.27% Z-pinned FE model. Figure 4.20(b) indicates that the cohesive elements started to fail locally from the stress concentration areas around the pinned holes (No. 14 pin region). Subsequently, the damage propagated to the entire cohesive element layer, leading to the load drop.

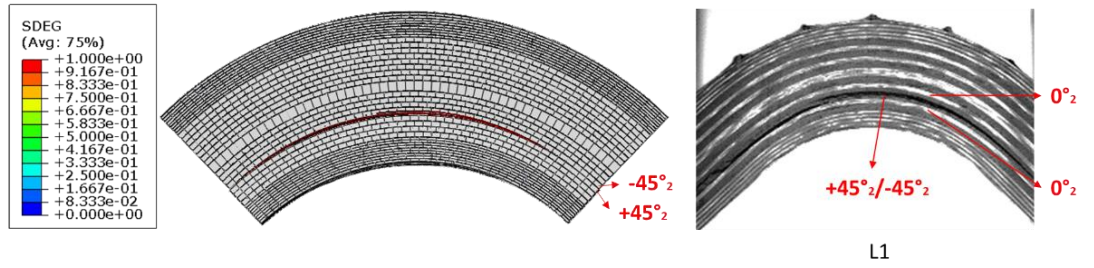

(a)

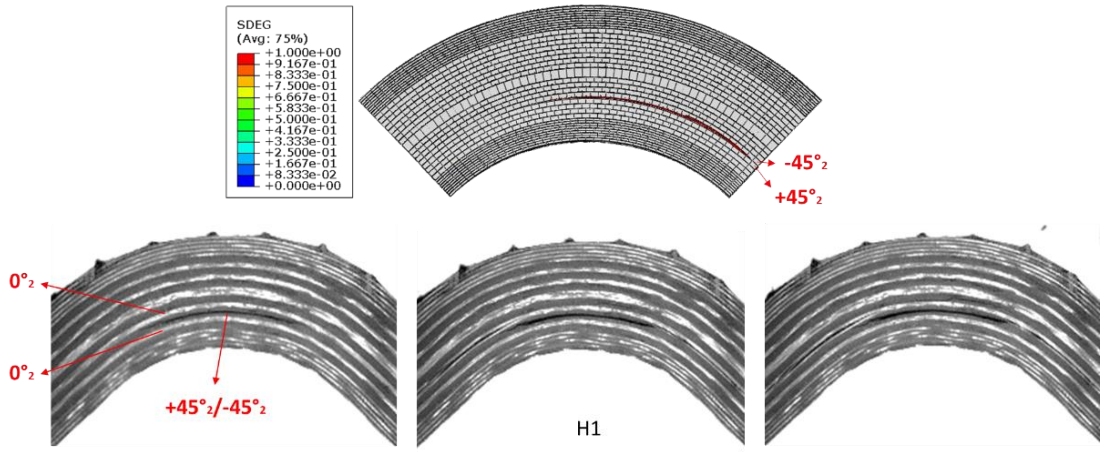

(b)

Figure 4.19: Experimental and modelling failure of (a) 0.27%, (b) 0.54% carbon-fibre Z-pinned specimens.

To analyses the pin failure, the axial stress of the No. 14 pin during this time period is examined, as presented in Figure 4.21. When the cohesive layer failed, the pin was under bending with a local maximum tensile stress of 427 MPa and compressive stress of -391 MPa, as shown in Figure 4.21(c). Within a very short time period, the crack opened quickly, causing the local tensile stress in the pin to rise dramatically to 1037 MPa. This value is close to the tensile strength (1200 MPa) of the T300/BMI carbon-fibre pin [61]. The simulation terminated at 0.6245 s due to the excessive distortion of cohesive elements, making it impossible to observe the stress at a further step. It is worth noting that the residual friction stress [54,55] was not considered in this model, which led to a relatively low predicted tensile stress. Thus, it can be concluded that the pin rupture occurs just after the failure of the cohesive layer.

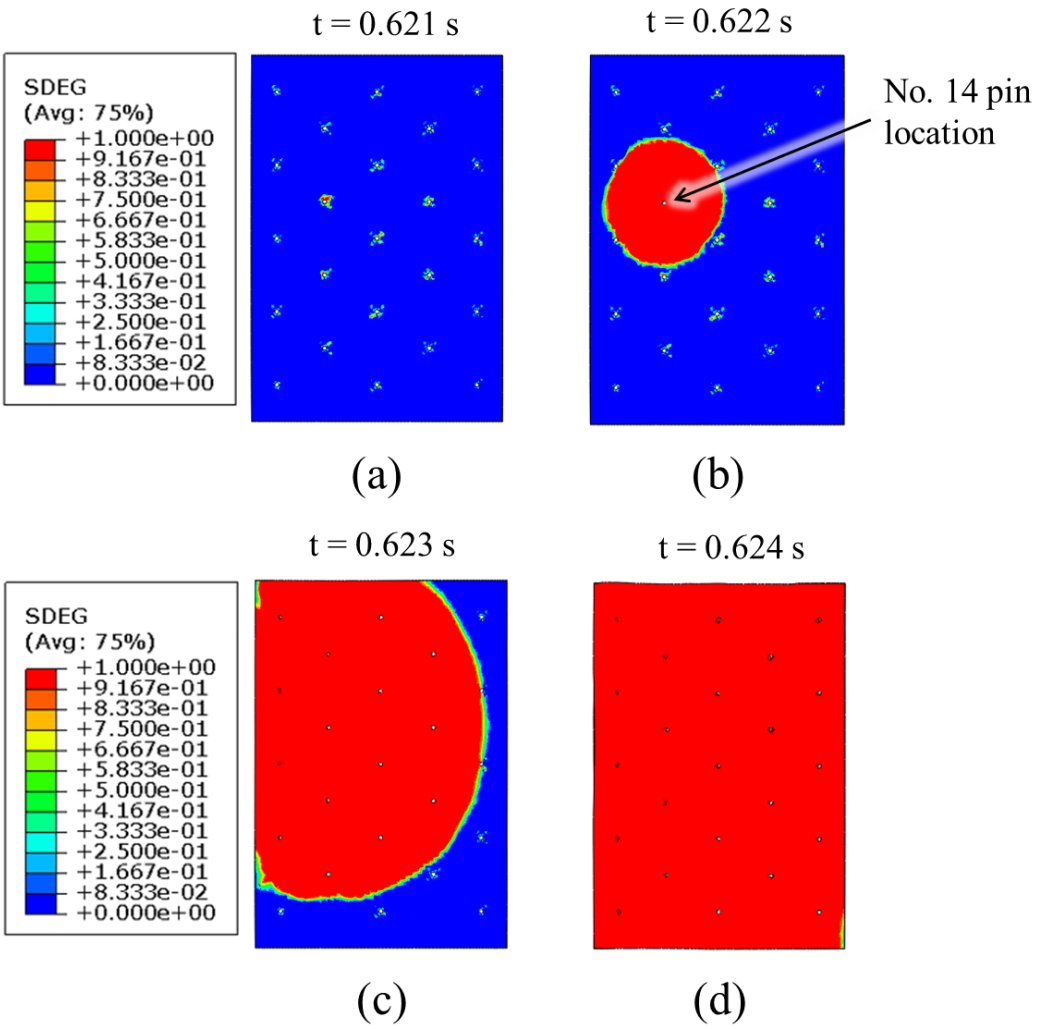

Figure 4.20: Failure of interlaminar cohesive layer for the 0.27% carbon-fibre Z-pinned specimen.

To examine the pin pull-out distance, Figure 4.22 plots the relative displacement between No. 14 pin and the surrounding laminate versus time. At the time step of 0.621 s, when the crack initiates, the relative displacement increases from 0.0085 mm to 0.0182 mm and then decreases when the cohesive layer fails. The maximum pull-out displacement is less than 10 μm, confirming that the pin is only pulled out at a very small distance and cannot form a large bridging zone to dissipate the mechanical energy under this circumstance.

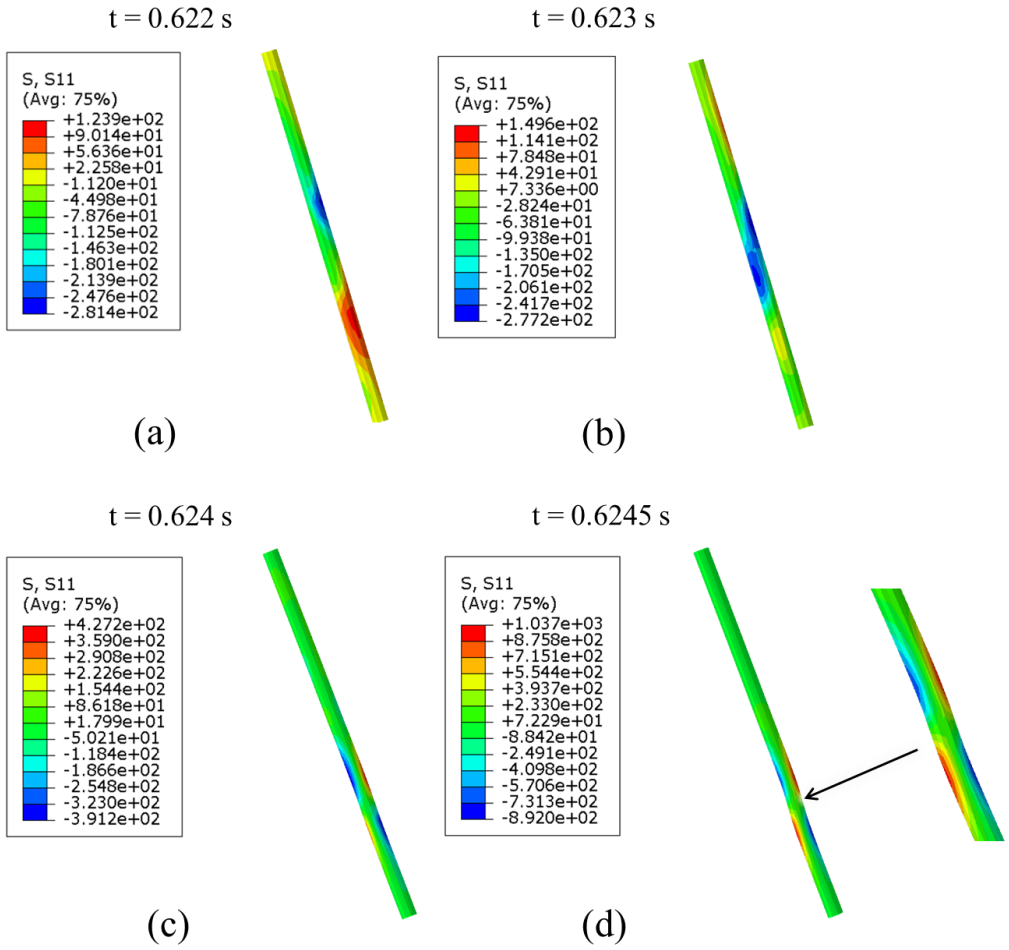

Figure 4.21: Axial stress of the No. 14 pin for the 0.27% carbon-fibre Z-pinned specimen.

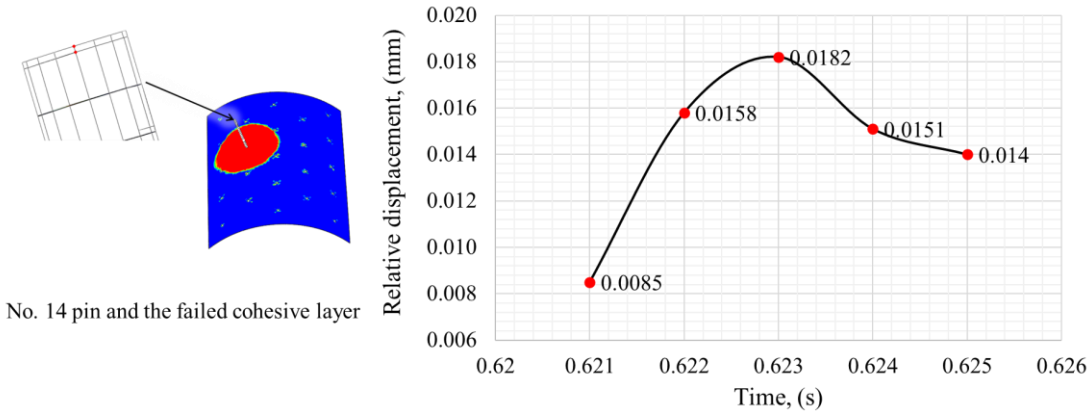

Figure 4.22: The relative displacement between pin and laminate during delamination.

4.4 Conclusions

In this chapter, high-fidelity meso-scale FE models were created for the unpinned and carbon-fibre Z-pinned specimens with a versatile mesh generation code, then simulated in Abaqus/Explicit. With the aid of FE models, the failure mechanisms observed from the experiment were analysed. Some conclusions could be drawn as below:

- The in-plane shear stress drove the delamination near the top surface of unpinned specimens.
- The modelling load-displacement curves' linear parts agree well with the experimental results for both unpinned and carbon-fibre Z-pinned specimens.
- The unpinned model successfully captures the catastrophic failure in the mid-through thickness region, and the predicted failure load is close to the experimental mean value.
- High residual stress was generated inside the laminate at the areas around pins during the cool-down process after cure, and the pin ends partially debonded from the laminate at this stage.
- The damage of failed cohesive elements layer was found to start from the pinning holes. Once the cohesive layer was failed completely, the carbon-fibre pin was ruptured in a very short time due the high local tensile stress generated from the crack's shear 'opening'. The pull-out displacement of pin was very small, and a large bridging zone was not formed.

In summary, the FE modelling has shown that the residual interlaminar stress generated from the post-cure cool-down stage is very high in the pin proximity, and there is also stress concentration around the holes. These features cause the crack to start from the pinning regions and reduce the through-thickness tensile strength of carbon-fibre Z-pinned specimens. Future work could focus on characterising the effects of pin/laminate interface friction force using FE modelling.

5 EFFECTS OF Z-PINS ON THE FAULT CURRENT RESPONSE OF COMPOSITES

5.1 Introduction

The use of electrical power in aircraft is on the rise to boost overall efficiency, and cut fuel consumption, therefore reducing greenhouse gas emissions. It also provides better control performance and reduces maintenance. Thus, more electric aircraft (MEA) or full electric aircraft are being developed worldwide, together with the adoption of electric propulsion systems [98,99]. In parallel, there has been a trend towards using non-metallic composite materials, particularly CFRP, to reduce the structural weight. One of the advanced MEAs, Boeing 787, has more than 50% of its structure built of CFRP. This results in a 20% reduction in structural weight and an improvement of 10-12% in total aircraft efficiency [100].

Continuous electrical current conduction through the CFRP may cause localised Joule heating that results in matrix degradation and can ultimately lead to structural failure. To garantee that current does not go through CFRP when there is an electrical fault, bulky cable harnesses and heavy raceways are used

extensively to form a return network for the current via existing metallic structures. Additional weight and volume are added to the system and advantages of mechanical performance attributable to the usage of CFRP are weakened [101,102]. Thus, the aerospace industry is promoting the creation of an embedded system by integrating electrical power systems with the aircraft's structural components [102]. It allows CFRP components to join the current return path under electrical fault conditions. The high impedance of CFRP will lead to a low electrical fault current that is difficult to detect with traditional grounding topology, while the Joule heating effects sitll exit [102]. Therefore, it is crucial to enhance CFRP's electrical conductivity and have a thorough understanding of its behaviour under fault currents before and after the conductivity enhancement.

Due to the high electrical anisotropy of CFRP, electrical behaviour of CFRP is more complex than metals. Piche et al. [103] modelled the dynamic electrical property of a CFRP under a short circuit by combining a 3D linear wired approach with an analytical model. The fibres, connection between fibres and plies were represented with thin wire networks. The modelling resistance was validated with the experimental data for a QI laminate in the time domain. Jones et al. [104] experimentally investigated the fault current response of a unidirectional (UD) CFRP. The time to reach the glass transition temperature (T_g) against the initially applied voltages/ power was found to follow a nonlinear decaying power relationship.

However, there is a lack of study on the fault current response of through-thickness reinforced composites. This chapter investigated electrical and consequential thermal behaviour of Z-pinned laminates under fault currents for the first time. Specimens with two pin materials at two areal densities were measured under a variety of in-plane and through-thickness fault currents, in comparison with unpinned ones. Specifically, specimen preparation is introduced in Section 5.2. Resistance measurement results are presented in Section 5.3, then fault current tests and results are illustrated in Section 5.4.

5.2 Specimen preparation

The specimens used in this study were made of UD M21/IMA prepreg (HexPly® M21/34%/UD194/IMA-12K) [105] following the QI stacking sequence of $[+45°/90°/-45°/0°]_{3s}$. The M21/ IMA laminates include an additional layer of resin toughened with thermoplastic particles as a separate interleaf between plies [106]. The interleaving method is a well-known way to increase the inter-laminar toughness of cured laminates [107], but the thick interleaf layer has a negative influence on electric current.

Two types of pins with the same diameter of 0.28 mm, i.e. copper (from WIRES) and the more conventional T300/BMI pin were employed to make Z-pinned specimens. The reason for choosing a copper pin is primarily due to its significantly higher conductivity compared to carbon-fiber composites pin. Consequently, the impact of the pin material on the overall performance will be readily apparent. The pin-to-pin distances were designed to be 8 mm and 5 mm respectively, which gives the pinning areal densities of 0.1% and 0.25%. In total, five categories of samples were manufactured, unpinned (UP), copper low-density (COP-L) and high-density (COP-H) Z-pinned, carbon low-density (CAR-L) and high-density (CAR-H) Z-pinned.

The specimen manufacturing process mainly includes:

- Design the sample and pinning layout for the laminate (Figure 5.1(a)).
- Layup the prepreg in sequence on an aluminium plate and de-bulk for 15 mins in a vacuum bag after every four plies.
- Soften the laminate with a hot plate underneath and manually insert pins through the thickness of laminates. A printed layout paper wrapped with a release film was placed on top the laminate to locate the pinning position as shown in Figure 5.1(b).
- Cure the laminate in an autoclave under a modified Hexcel cure cycle [105] to compensate the influence of two layers of silicon rubber placed on the top and bottom of laminate.
- Cut individual samples from the cured laminate with a diamond saw.

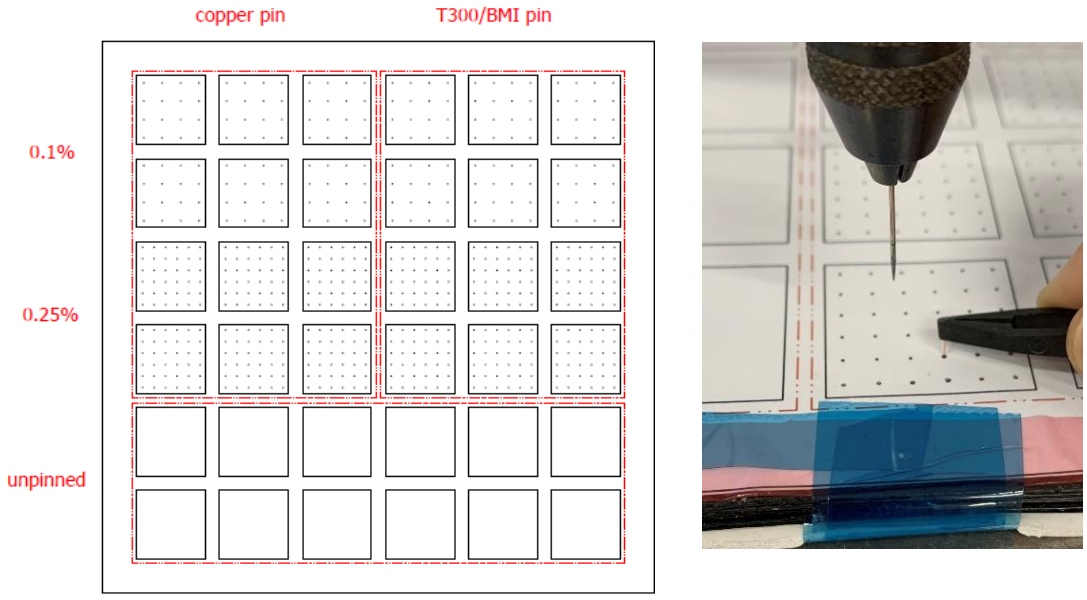

(a) (b)

Figure 5.1: (a) Sample layout drawing, (b) pinning photo.

Figure 5.2 is the photo of cured laminate. Each ply has a nominal thickness of 0.188 mm after cure. The sample has a dimension of 30 × 30 × 4.5 mm^3 (length × width × thickness).

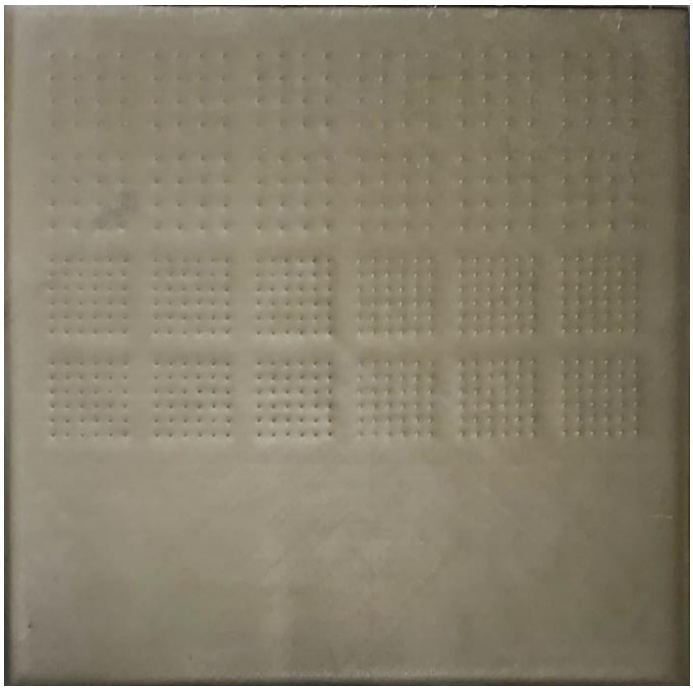

Figure 5.2: The cured laminate.

5.3 Resistance measurement

5.3.1 Measurement setup

Similar to the scenario that Jones et al. considered in Ref. [104], the rail-to-ground fault inside a CFRP structure was investigated, which can be caused by the vibration and chafing of an insulator. Here the current path is extended to in-plane and through-thickness directions, respectively, as shown in Figure 5.3.

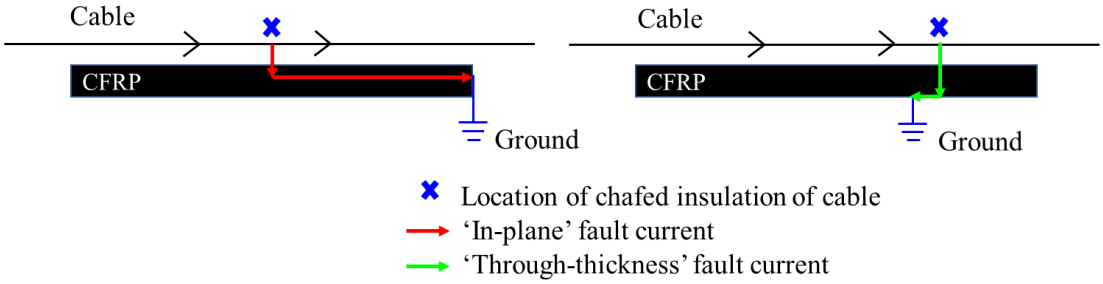

Figure 5.3: Path of the fault current through a CFRP structure.

The study of Ref. [104] was based on a UD laminate. Here, a QI stacking sequence, which is more commonly used in the composites industry was investigated, as well as the effects of Z-pins on the fault current performance of composites. The scenario is more complex for a QI stacking sequence with +45° surface plies. Thus, nine current input areas were designed on the top surface to take into consideration of different circumstances caused by chafing of an electric cable, for example. The exit points were on the side and bottom surfaces respectively, which represented the in-plane and through-thickness fault currents.

Figure 5.4: The designed polisher rig.

Epoxy on the top and bottom plies was carefully removed by a polisher to mimic the cable chafing effect. An aluminum polish rig (Figure 5.4) was specially designed and made in the workshop to polish these square-shaped samples.

A thin layer of silver was painted uniformly on each 1×1 mm^2 square box. In order to achieve a good painting quality, the to-be-painted area was cut out from adhesive paper by a laser cutter (Figure 5.5), then the paper was pasted on the sample, afterwards the silver paste was brushed in the blank area. The top and bottom surfaces of Z-pinned samples with numbered silver paint electrodes are shown in Figure 5.6.

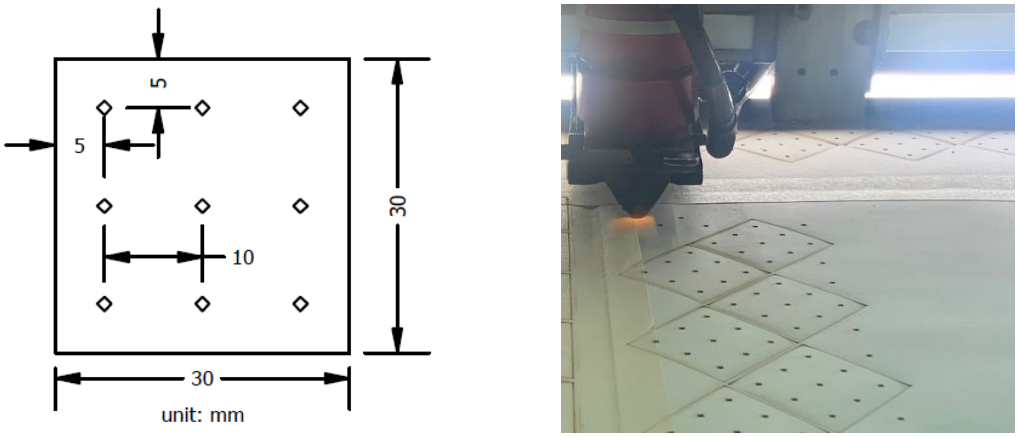

(a) (b)

Figure 5.5: (a) Chafing areas layout, (b) laser cutting of the adhesive paper.

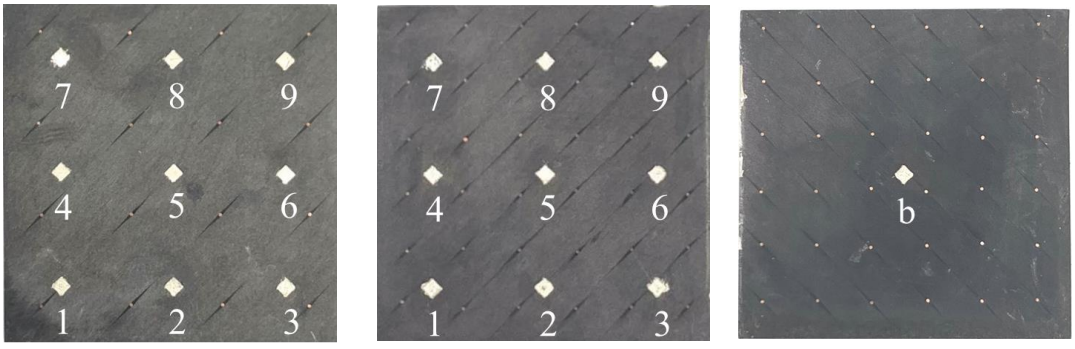

(a) (b) (c)

Figure 5.6: Sample photos: (a) COP-L top surface, (b) COP-H top surface, (c) COP-H bottom surface.

Three different methods of connecting the electrodes were tried at the beginning, including wire contact, metal pin contact and wire clamping, as shown in Figure 5.7. The first one (Figure 5.7(a)) is holding a wire manually with moderate pressure applied to ensure a tight connection. In Figure 5.7(b), a metal pin was fixed to have a secure contact with the electrode by a magnetic stand. The third method involves using a G-clamp to secure the wire in place (Figure 5.7(c)). The side surface of the specimen was coated with silver paste and a copper block was tightly clamped to it. This was done to reduce the contact resistance and ensure consistency in the measurements.

(a) (b) (c)

Figure 5.7: Trials of test set-up, (a) wire contact, (b) metal pin contact, (c) wire clamping.

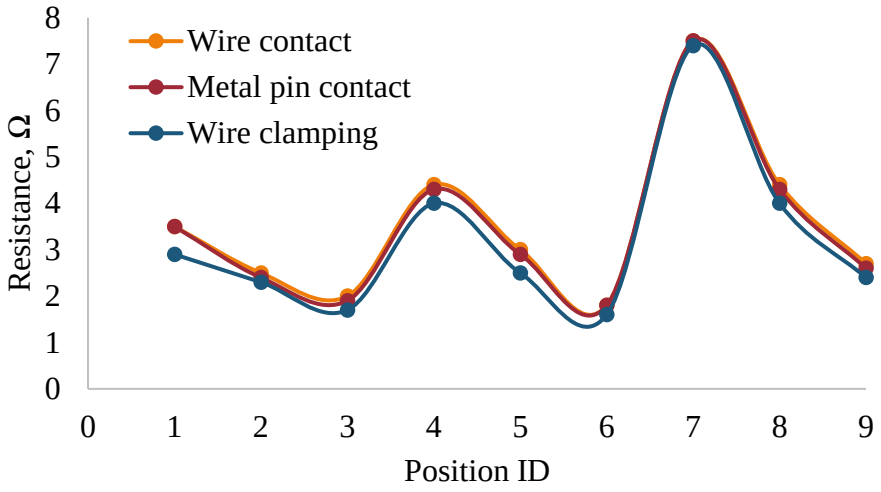

Figure 5.8: Test results of different set-ups.

The test result read from a millimeter is plotted in Figure 5.8. It shows that the difference between the three set-ups is very small, especially for the manually held wire (1st method) and metal pin contact (2nd method). The contact pressure applied by a hand, a magnetic stand, and a G-clamp have a negligible difference in the result. Finally, the second method with a metal pin was adopted as it makes the surface visible for thermal imaging and keeps the consistency for each measurement simultaneously.

When measuring the in-plane resistance (Figure 5.9(a)), each of the top surface electrodes was connected to a probe of a milliohm meter in turn. For the through-thickness measurement (Figure 5.9(b)), a probe was connected to each of the top surface electrodes in turn and the output was recorder from a probe on the central bottom electrode using metal pins. Each measurement was taken twice to ensure accuracy, and a negligible bias was achieved.

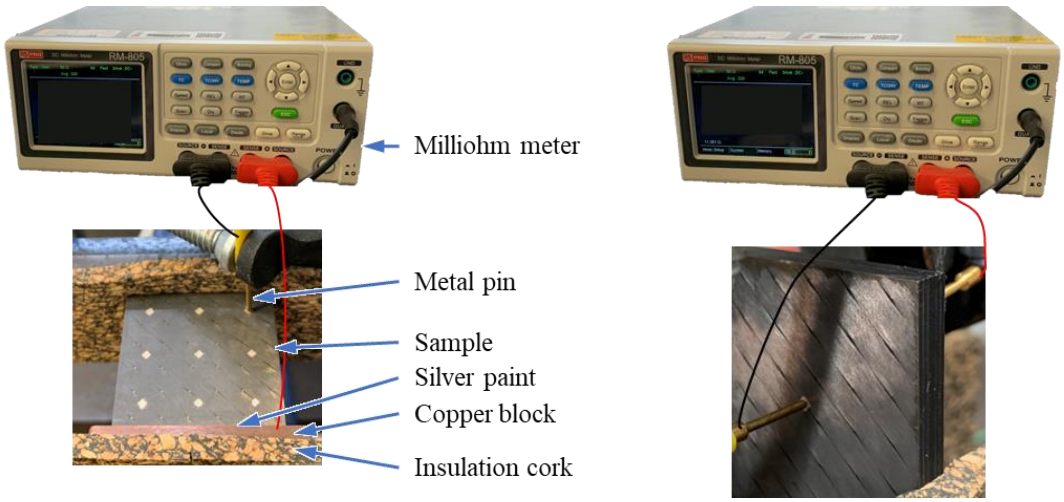

(a) (b)

Figure 5.9: Resistance measurement setup, (a) in-plane, (b) through-thickness.

5.3.2 Test results of the through-thickness direction

Three samples were tested for each group, the measured through-thickness and in-plane average resistances and variations are given in Table 5.1 and Table 5.2. Individual sample result is given in Table 9.1 and Table 9.2 in the appendix.

Table 5.1: Experimental results of the through-thickness resistance, (unit: Ω).

Type	Position	1	2	3	4	5	6	7	8	9
UP	AVE	1760	1767	1798	1772	1758	1767	1810	1771	1759
	C.V. %	39.0%	39.1%	38.5%	39.3%	38.9%	39.1%	38.7%	39.3%	39.0%
COP-L	AVE	32.26	41.62	57.56	36.92	31.43	43.02	54.34	38.04	32.66
	C.V. %	12.1%	10.6%	20.1%	5.2%	12.1%	12.4%	15.4%	4.5%	11.3%
COP-H	AVE	21.55	21.68	29.65	25.93	20.68	23.80	31.82	23.43	21.80
	C.V. %	14.8%	11.6%	20.8%	19.7%	16.8%	21.8%	9.2%	10.9%	21.7%
CAR-L	AVE	23.07	26.37	35.91	26.74	22.41	26.24	40.03	26.28	23.43
	C.V. %	20.7%	17.5%	23.1%	15.1%	21.4%	17.2%	22.3%	15.8%	18.2%
CAR-H	AVE	15.57	16.58	20.49	16.51	15.56	16.65	19.30	16.23	16.04
	C.V. %	9.8%	13.2%	9.1%	6.8%	8.2%	12.6%	8.1%	6.7%	8.2%

Table 5.2: Experimental result of the in-plane resistance, (unit: Ω).

Type	Position	1	2	3	4	5	6	7	8	9
UP	AVE	8.88	3.05	3.23	33.80	7.70	1.94	76.19	33.81	8.40
	C.V. %	56.6%	33.3%	21.1%	40.0%	56.4%	17.1%	50.4%	39.9%	47.2%
COP-L	AVE	6.01	4.74	3.10	11.30	4.56	3.83	28.13	12.94	5.66
	C.V. %	40.7%	30.8%	19.3%	43.9%	2.3%	28.4%	30.2%	24.3%	23.9%
COP-H	AVE	4.31	2.91	3.20	7.52	3.54	2.46	14.03	7.15	3.20
	C.V. %	20.5%	16.5%	19.9%	33.0%	27.0%	26.0%	32.0%	33.1%	27.9%
CAR-L	AVE	4.26	4.23	3.14	8.44	3.57	3.82	22.25	8.50	3.39
	C.V. %	4.5%	11.5%	65.6%	4.7%	5.7%	6.3%	19.1%	9.2%	9.6%
CAR-H	AVE	3.27	2.53	2.32	4.38	2.76	2.02	7.33	4.21	2.93
	C.V. %	22.5%	17.4%	23.2%	1.6%	20.6%	16.1%	6.0%	7.4%	1.4%

Table 5.1 shows that the through-thickness resistances of unpinned samples are at the order of 10^3 ohms. After adding pins, the resistance decreased significantly at all nine locations (less than 10^2 ohms). The resistance variation of unpinned sample is much higher than Z-pinned ones, comparing the coefficients of variation (C.V.) in Table 5.1. The reason will be discussed later.

The mean value of measured resistance is plotted in Figure 5.10. Due to the large difference between unpinned and Z-pinned samples, the unpinned data is plotted using a secondary y-axis on the right. The plot has a symmetric trend which is consistent with distribution of top-surface electrodes, e.g., positions 1 & 9, 2 & 8, 3 & 7, and 4 & 6 are symmetrical about position 5. The resistance of positions 3 & 7 is the highest, because the current needs to travel furthest in the direction perpendicular to surface-ply fibres to reach the bottom surface exit electrode b. It also implies that the current path of the top ply dominates the global result.

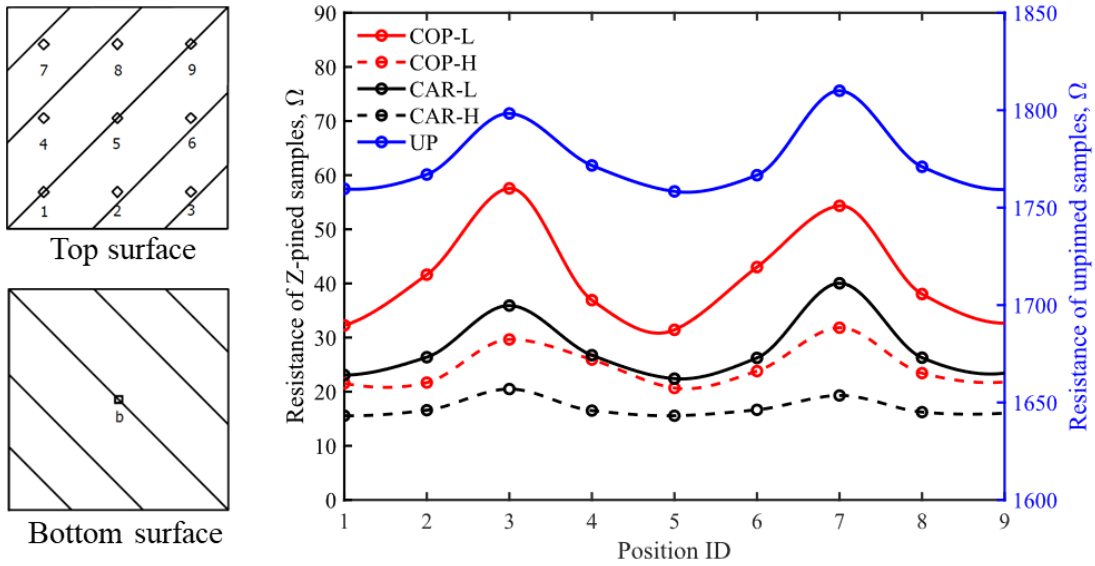

Figure 5.10: Experimental plot of the through-thickness resistance.

5.3.3 Test results of the in-plane direction

For the in-plane direction (Table 5.2), the Z-pins also reduce the resistance, although the amount is not as much as the through-thickness direction. The similar top layer dominated behaviour was observed in Figure 5.11. If the current can pass

from fibres at the chafing area to the exit electrode directly, the resistance is low, such as positions 1, 2, 3, 5, 6 and 9. The resistances associated with positions 4, 7 and 8 of Z-pinned samples are much smaller than unpinned ones, because the current is able to transfer through the thickness, then go through the fibres of other layers to the side exit electrode.

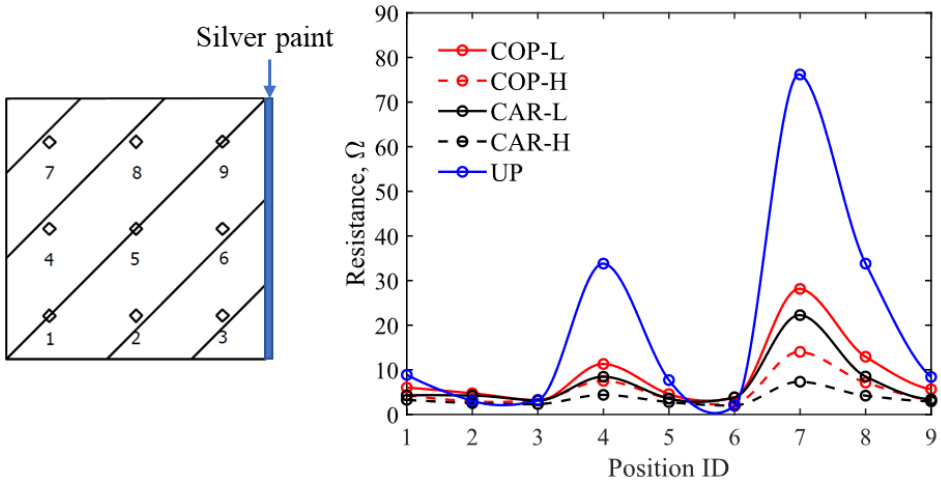

Figure 5.11: Experimental plot of the in-plane resistance.

5.3.4 Result discussion

5.3.4.1 Influence of Z-pin materials and areal densities

The resistance of copper Z-pinned samples is higher than carbon-fibre Z-pinned samples in both in-plane and through-thickness directions (comparing the red and black curves in Figure 5.10 and Figure 5.11), while the electric conductivity of copper pins is much higher than carbon-fibre pin [12]. The copper pins therefore didn't function as expected for the through-thickness current transfer.

As reported in the literature, the laminate fibres are forced to bend around the pin during insertion [3]. The resin pocket around the pin and the interfacial cracking impedes the current flow within the ply. In order to see the detailed information around the pin, the samples were cut into slices and potted with epoxy resin (Figure 5.12 (a)), then polished to make the individual fibre visible.

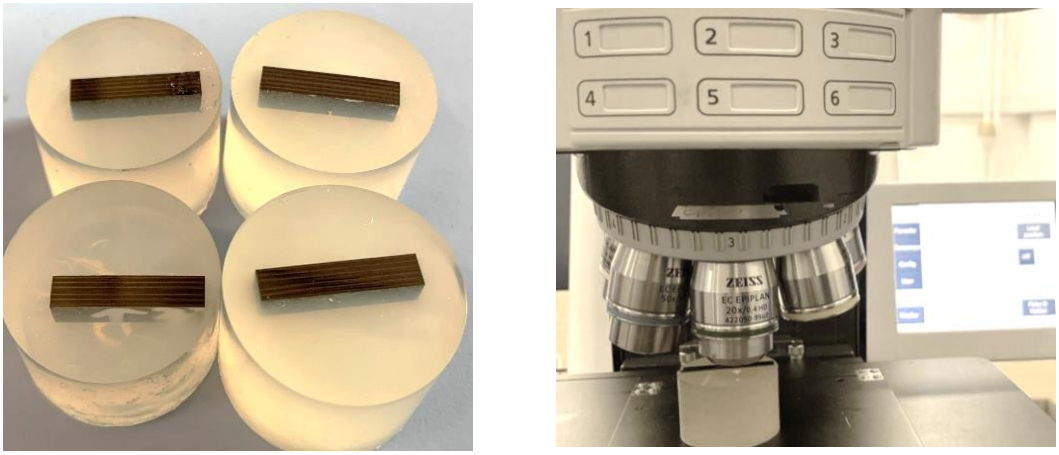

(a) (b)

Figure 5.12: (a) Potted samples, (b) microscope imaging with ZEISS.

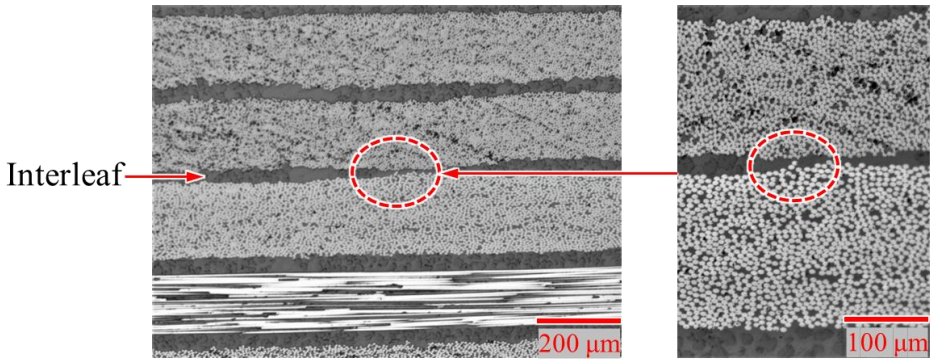

(a)

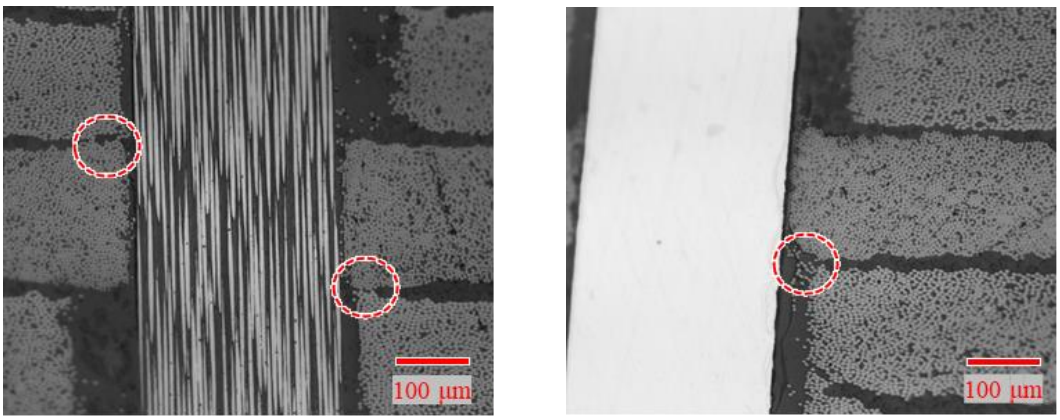

(b) (c)

Figure 5.13: Microscope images of sample cross sections, (a) unpinned, (b) carbon-fibre Z-pinned, (c) copper Z-pinned.

The microscope images from ZEISS (Figure 5.12 (b)) of the cross sections are given in Figure 5.13. It shows that there is randomly localized interlaminar fibre touching inside the unpinned sample (Figure 5.13(a)). Since they are randomly distributed, the through-thickness resistance of unpinned samples varies a lot (as shown in Table 5.1).

In Figure 5.13(b, c), due to the fibre bending around the pin (known as crimping), more fibre touching was observed in the through-thickness direction for both carbon-fibre Z-pinned and copper Z-pinned samples. Thus, the electrical conductivity is mainly related with the pinning quality, e.g., the misalignment angle. As the copper pin is soft, although great care was taken during insertion, it was slightly bent, and the misalignment angle is higher than that of carbon-fibre pins.

For a quantitative comparison, the resistance of a reference laminate was measured, which was pinned with enamelled copper wires. This wire has the same size as bare copper wire with 0.28 mm diameter, with a polymer layer coated on the outside, making the pin electrically isolated on its surface. The measured resistance of the enamelled copper pinned (ECOP) specimens was very close to that of the uncoated copper pinned ones, as shown in Figure 5.14. It again demonstrates that the pin itself is not directly engaged in the current path. The fibre-to-fibre connections, instead of the pins, are the main current flow path for through-thickness conduction. The enamelled copper pin was only used to examine if the conductivity of the pin has an effect on the global resistance here, and it will not be discussed in the following sections.

In addition, the high-density Z-pinned samples have lower resistance than low-density ones for both pin materials (comparing the solid and dashed curves in Figure 5.10 and Figure 5.11), because the higher areal density brings more fibre connections in the vicinity of the pins.

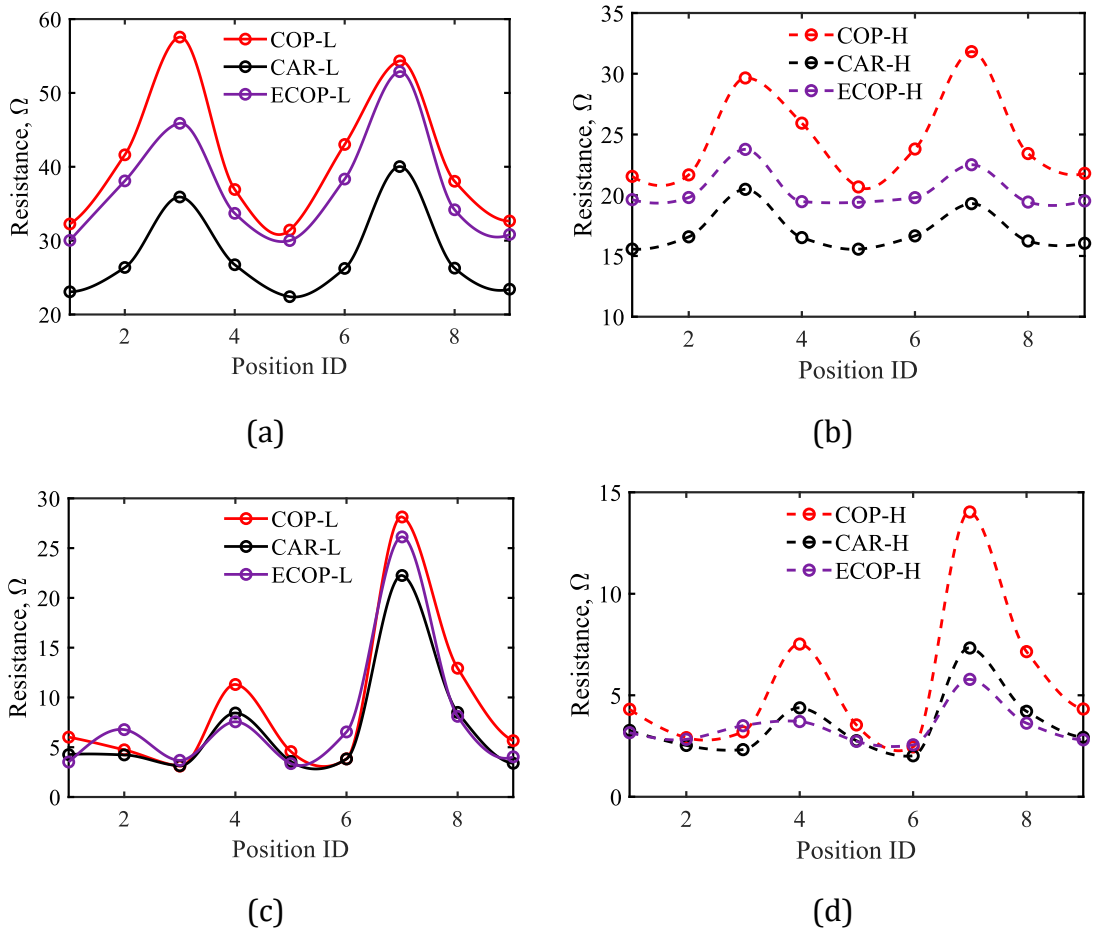

Figure 5.14: Experimental resistance of the enamelled copper pins, (a, b) through-thickness, (c, d) in-plane, (L: low density, H: high density).

5.3.4.2 Current transfer path

For an intuitive view, an illustration of the current transfer path of the first two plies and interfaces is given in Figure 5.15, assuming that there are three and two fibre touching zones in the 1st and 2nd interfaces, respectively. The red, blue and green lines represent the current path from the injection position. Specifically, the current will pass through the top ply (1st ply), then the pin vicinity with fibre touching in the 1st interface, and afterwards within the 2nd ply to find the conductive path in the 2nd interface.

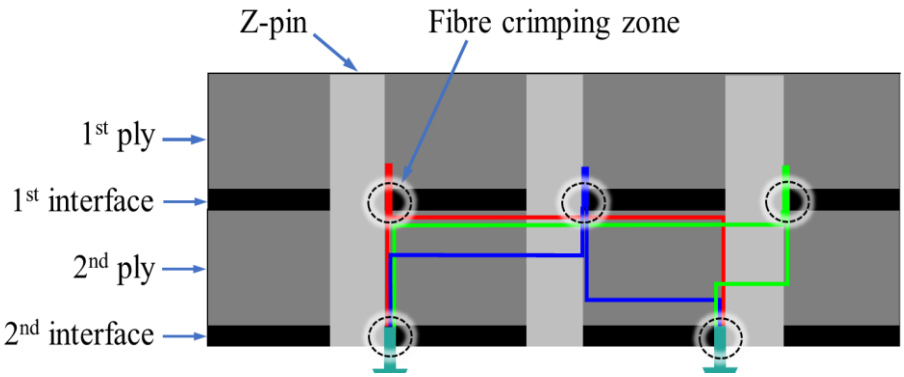

Figure 5.15: Schematic diagram of the current path inside the first plies.

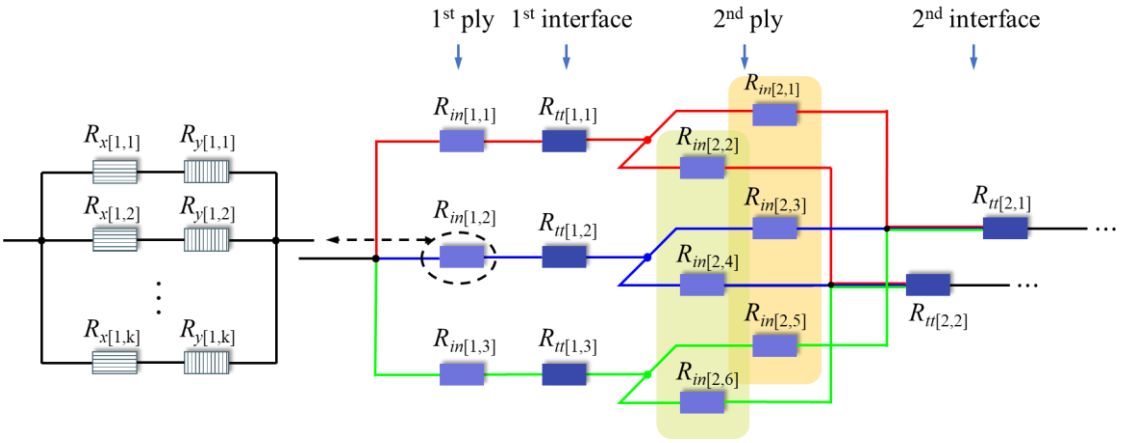

Figure 5.16: 3D topology electrical resistance model.

The 3D topology electrical resistance model is drawn in Figure 5.16, in which $R_{in[i,m]}$ and $R_{tt[j,n]}$ are the m^{th} equivalent resistor of i^{th} ply and n^{th} the resistor of the j^{th} interface, respectively. From the diagram, it can be seen that if the number of fibres touching zones within two adjacent interfaces are *a* and *b*, there is a*b current path generated inside the ply in-between. For instance, there are 6 current paths in the 2nd ply as shown in Figure 5.16. When inserting pins, the interlaminar resistance R_{tt} is reduced significantly, thus the total through-thickness resistance is much smaller. If adding more pins (increasing the pinning areal density), there are more current paths generated.

5.4 Fault current response test

5.4.1 Test setup

The resistance measurement results above show that the resistant reduction of position 7 by Z-pins is the most obvious for both in-plane and through-thickness directions, see Figure 5.10 and Figure 5.11. Thus, a constant current was injected from this position to simulate the in-plane and through-thickness fault current response of unpinned and Z-pinned laminates. The test set-up is shown in Figure 5.17. The current was supplied with a source meter (KEYSIGHT B2902A). A data logger was used to collect the data of voltage and temperature (when a thermocouple was applied), and a thermal camera was employed to capture the temperature distribution on the samples' surface.

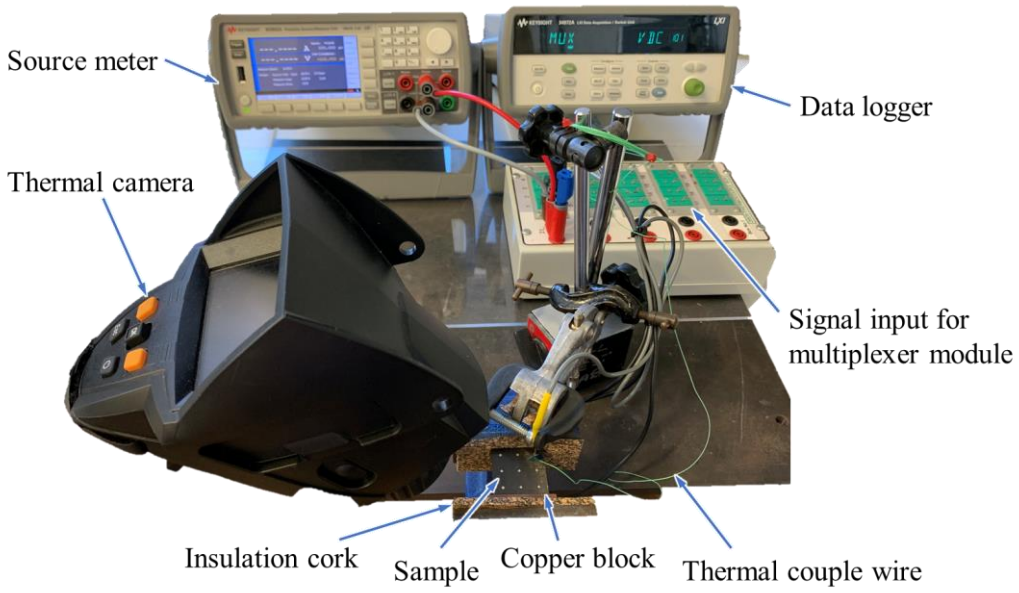

Figure 5.17: Fault current response test set-up.

The current injection lasted for 10 mins (600s) for each test. Figure 5.18(a) shows the temperature versus time plot of an unpinned sample at different levels of current. It shows that the temperature grows very fast at the beginning, then becomes stable after 400 s. A period of 10 mins is long enough to achieve a temperature stable state.

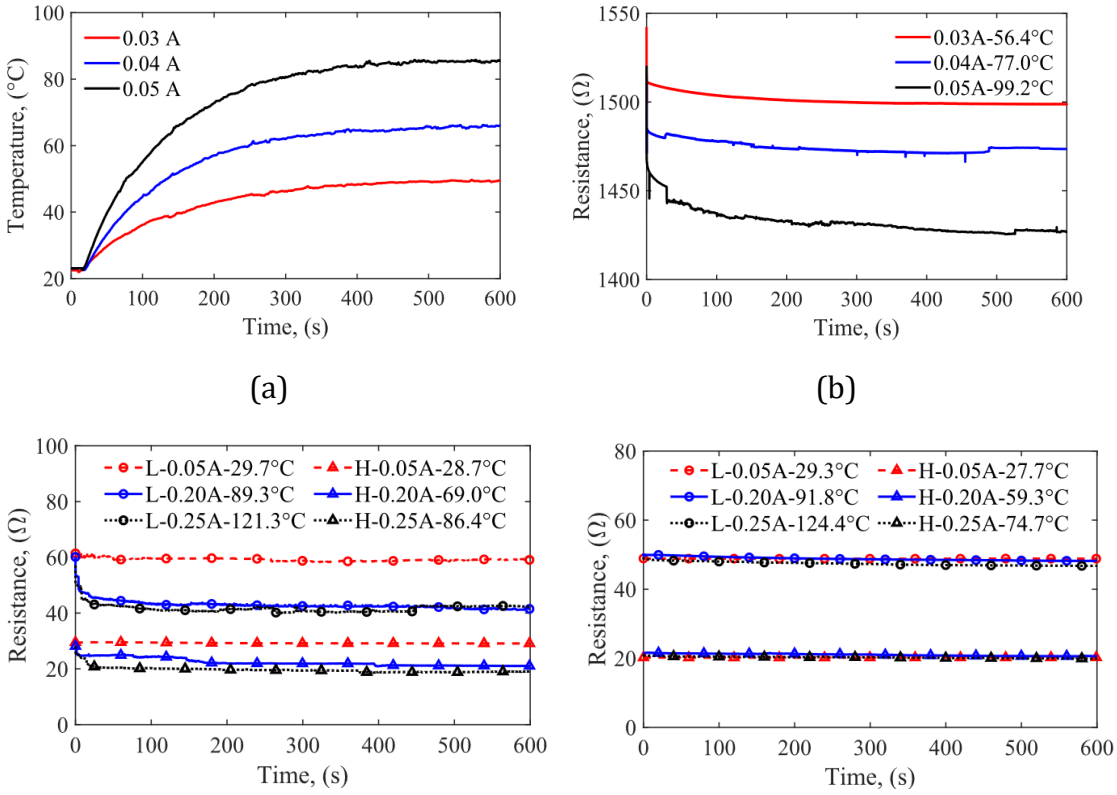

Figure 5.18: (a) Temperature versus time plot of an unpinned specimen, through-thickness fault current response test results of (b) unpinned, (c) copper and (d) carbon-fibre Z-pinned specimens, (L: low density, H: high density).

5.4.2 Test results of the through-thickness direction

The instantaneous power $P(t)$ has the following relationship with the fault current I_f and resistance $R(t)$:

$$P(t) = I_f^2 \cdot R(t) \tag{5-1}$$

In this case, $R(t)$ is a time dependent variable, and I_f is constant, controlled by the source meter accurately. As the through-thickness resistance of the unpinned samples is much higher than Z-pinned ones, in order to achieve a comparable level of power, the injected current for unpinned samples is smaller than Z-pinned ones.

5.4.2.1 Resistance versus time

The injected current, initial resistance, power, and the ultimate temperature T_u are summarized in Table 5.3. It shows that T_u increases with the current amplitude for each type of sample. When all types of samples were injected with the same current of 0.05 A, T_u of the unpinned sample goes up to 99.2 °C, which is much higher than that of Z-pinned samples (less than 30 °C). The pins effectively suppress the Joule heating effect and keep the resin in a safe temperature margin when there is a top-to-bottom fault current.

Table 5.3: Current injection data for the through-thickness direction.

	Initial Resistance (Ω)	**Injected current (A)**	**Initial Power (W)**	**Final Temperature (°C)**
UP	1577	0.03	1.42	56.4
	1577	0.04	2.52	77.0
	1577	0.05	3.94	99.2
COP-L	62.4	0.05	0.16	29.7
	62.4	0.2	2.50	89.3
	62.4	0.25	3.90	121.3
COP-H	30.1	0.05	0.08	28.7
	30.1	0.2	1.20	69.0
	30.1	0.25	1.88	86.4
CAR-L	49.8	0.05	0.12	29.3
	49.8	0.2	1.99	91.8
	49.8	0.25	3.11	124.4
CAR-H	21.2	0.05	0.05	27.7
	21.2	0.2	0.85	59.3
	21.2	0.25	1.33	74.7

The resistance versus time is plotted in Figure 5.18(b-d) with the injected current and ultimate temperature listed in the legend. In Figure 5.18 (b), the resistance of unpinned samples decreases suddenly at the beginning, then tends to stablise. The

decrease is mainly caused by the thermal expansion, which enhances transverse and interlaminar fibre touching [108].

When the copper Z-pinned samples are under higher currents of 0.2 A and 0.25 A (Figure 5.18(c)), the resistance decreases at the beginning. While the resistance of carbon-fibre Z-pinned sample remains relatively constant throughout the test (Figure 5.18(d)). The resistance drop of copper pinned samples is mainly caused by the mismatch of the thermal expansion coefficient (CET) between the copper pin ($1.67e^{-5}$ °C^{-1}) [109] and the laminate (0 °C^{-1} in the fibre direction , $3e^{-5}$ °C^{-1} in transvers and through-thickness directions) [67]. Residual stress was generated at the pin/laminate interface during heating, enhancing the fibre touching of pin vicinity [3]. While the CETs of carbon-fibre pin and laminate are comparable, and the thermal expansion influence on the interface is negligible.

5.4.2.2 Heat flow within the top ply

The current flow inside the top surface of Z-pinned samples is discussed here. As mentioned in Section 5.3, for Z-pinned samples, the current flows through the pinning vicinity via fiber touching.

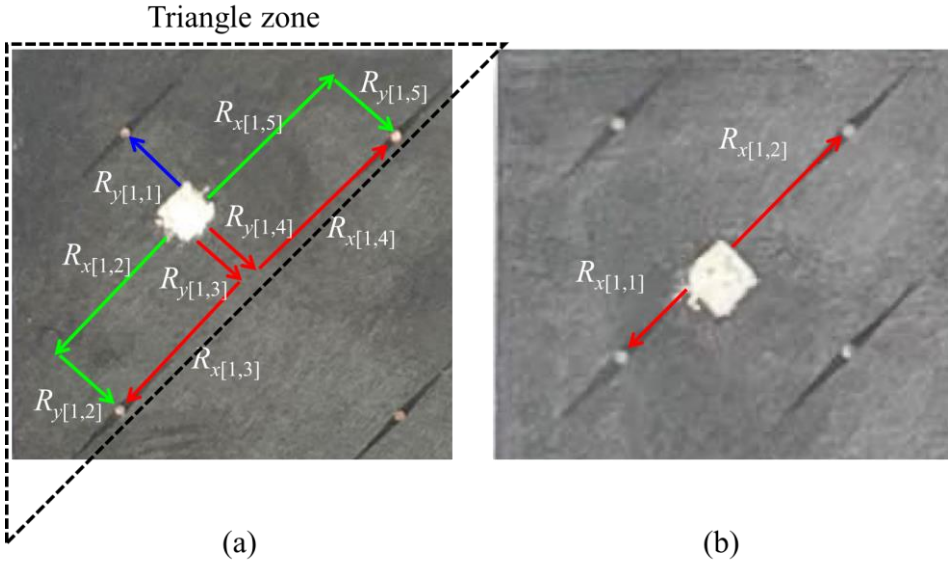

Figure 5.19: Current flow diagram in the top surface of Z-pinned samples; (a) COP-L top surface, (b) COP-H top surface.

In Figure 5.19(a) showing a low-density Z-pinned sample, there is no direct path from the current injection point to the pins through the fibres directly, thus the current will flow both along fibres (x axis) and perpendicular to fibres (y axis), and the whole triangle zone is involved in the current transfer. While for high-density Z-pinned ones, the current can flow to two adjacent pins through the fibres directly (Figure 5.19(b)).

The left picture of Figure 5.16 gives an example of the electrical resistor model of the in-plane resistor $R_{in[1,2]}$. In general, the m^{th} equivalent in-plane resistor of i^{th} ply, $R_{in[i,m]}$, can be denoted with the resistors along and perpendicular to the fibre directions (R_x and R_y) as below, in which k is the number of conductive paths.

$$R_{in[i,m]} = \frac{1}{\frac{1}{R_{x[i,1]} + R_{y[i,1]}} + \frac{1}{R_{x[i,2]} + R_{y[i,2]}} \cdots + \frac{1}{R_{x[i,k]} + R_{y[i,k]}}} \qquad (5\text{-}2)$$

Since the heat flow distribution of carbon-fibre and copper Z-pinned specimens are similar, the result of copper Z-pinned specimens is given in Figure 9.6 and Figure 9.7 in the appendix. Figure 5.20 shows the thermal images of unpinned and carbon-fibre Z-pinned samples. The current injection (top) and exit (bottom) surfaces are on the left and right sides, respectively.

The bright areas correspond to regions with the highest temperature change along the current conducting path. As discussed above, for the low-density Z-pinned sample, the top left triangle area including three pins is involved in the current transfer, which can be observed in Figure 5.20(c). While for the high-density Z-pinned sample, two pinned areas appear brighter in Figure 5.20(e). When looking at the bottom surfaces of pinned specimens (Figure 5.20(d, f)), the pinned areas exhibit higher temperature than their surroundings, because these fibre touching zones are engaged in transferring the current. Regarding the unpinned sample in Figure 5.20(a), the heat distribution is uniform for both surfaces. A single hot spot is visible on the side surface, located in one of the areas where fibres are randomly touching each other. It is notable that the heated area on the bottom surface is greatest for the high-density carbon-fibre case out of all the pinned samples,

indicating that in this case the Z-pins have most significantly facilitated current flow through the thickness of the sample.

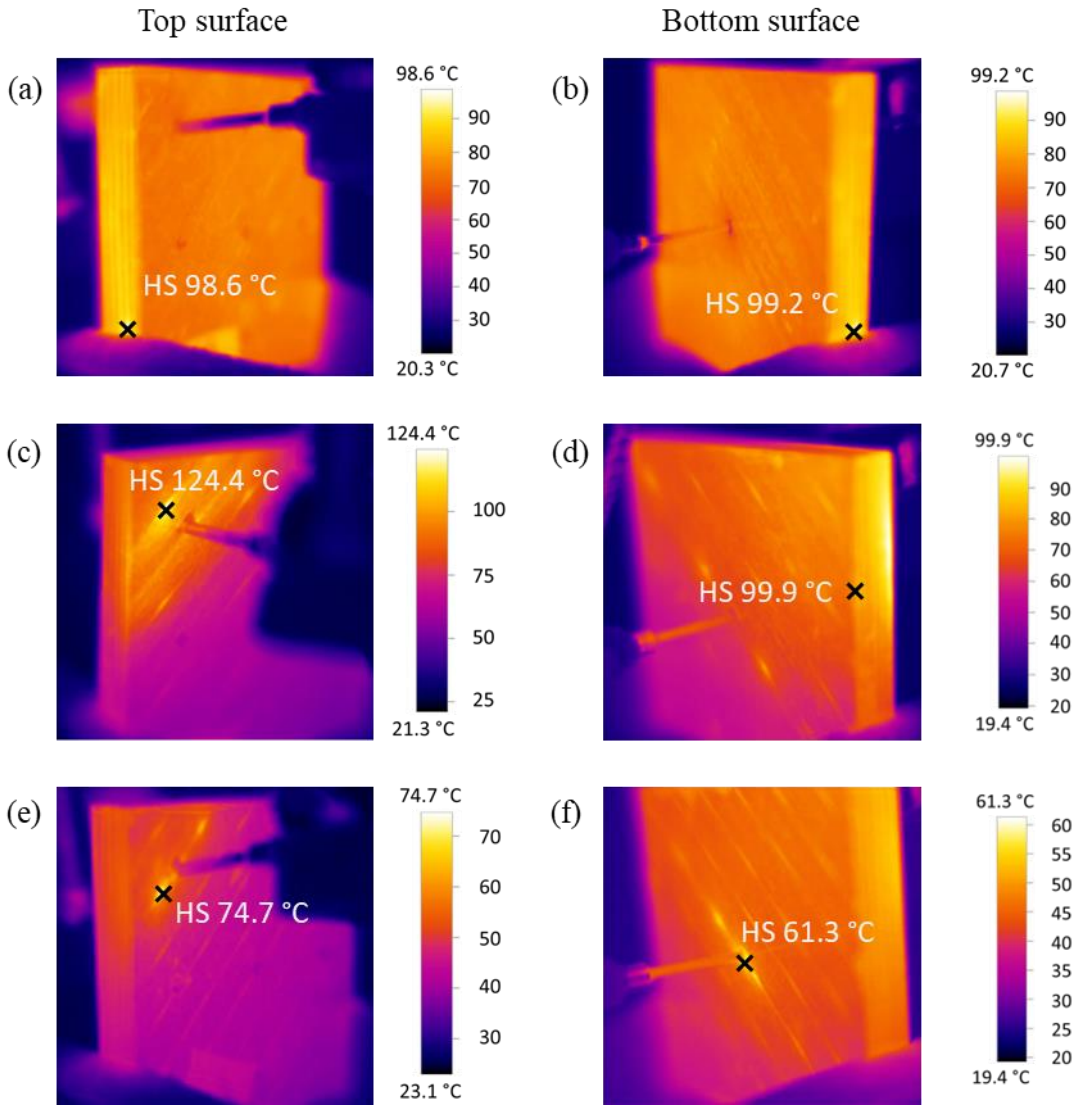

Figure 5.20: Through-thickness thermal images: (a, b) UP-0.05 A, (c, d) CAR-L-0.25 A, (e, f) CAR-H-0.25 A.

5.4.3 Test results of the in-plane direction

The current injection data from the in-plane direction tests is summarized in Table 5.4. Just like the through-thickness, the ultimate temperature T_u increases with the current amplitude. When the current is 0.2 A for all types of samples, T_u of unpinned sample (99.1 °C) is much higher than Z-pinned ones (maximum 56.8 °C).

Table 5.4: Current injection data for the in-plane direction.

	Initial Resistance (Ω)	Injected current (A)	Initial Power (W)	Final Temperature (°C)
UP	55.9	0.1	0.52	43.0
	55.9	0.2	2.09	99.1
COP-L	27.2	0.2	1.09	56.8
	27.2	0.3	2.45	99.1
	27.2	0.4	4.35	149.4
COP-H	14.0	0.2	0.56	44.9
	14.0	0.3	1.26	70.0
	14.0	0.4	2.24	106.6
CAR-L	21.8	0.2	0.87	53.8
	21.8	0.3	1.96	91.4
	21.8	0.4	3.49	132.6
CAR-H	8.2	0.2	0.33	41.0
	8.2	0.3	0.74	62.3
	8.2	0.4	1.31	95.0

The resistance versus time is plotted in Figure 5.21. It also shows that the resistance of unpinned samples drops suddenly at the beginning, then becomes stable. In terms of the copper pinned samples, it has been illustrated in Figure 5.18(c) that the resistance decreases when temperature goes up for the through-thickness fault current. While the resistance doesn't change when it experiences an in-plane current, as shown in Figure 5.21(b). It implies that the current only goes through a few plies instead of the whole thickness under this circumstance, by comparing Figure 5.18(c) with Figure 5.21(b). On the other hand, the resistance of carbon-fibre pinned samples is still quite stable.

The thermal images of the top surface are presented in Figure 5.22. In Figure 5.22(a), it has a random hot spot on the top surface of the unpinned samples, which is one of the through-thickness fibre touching area. In terms of the carbon-fibre Z-pinned samples, the in-plane thermal images are quite similar to the

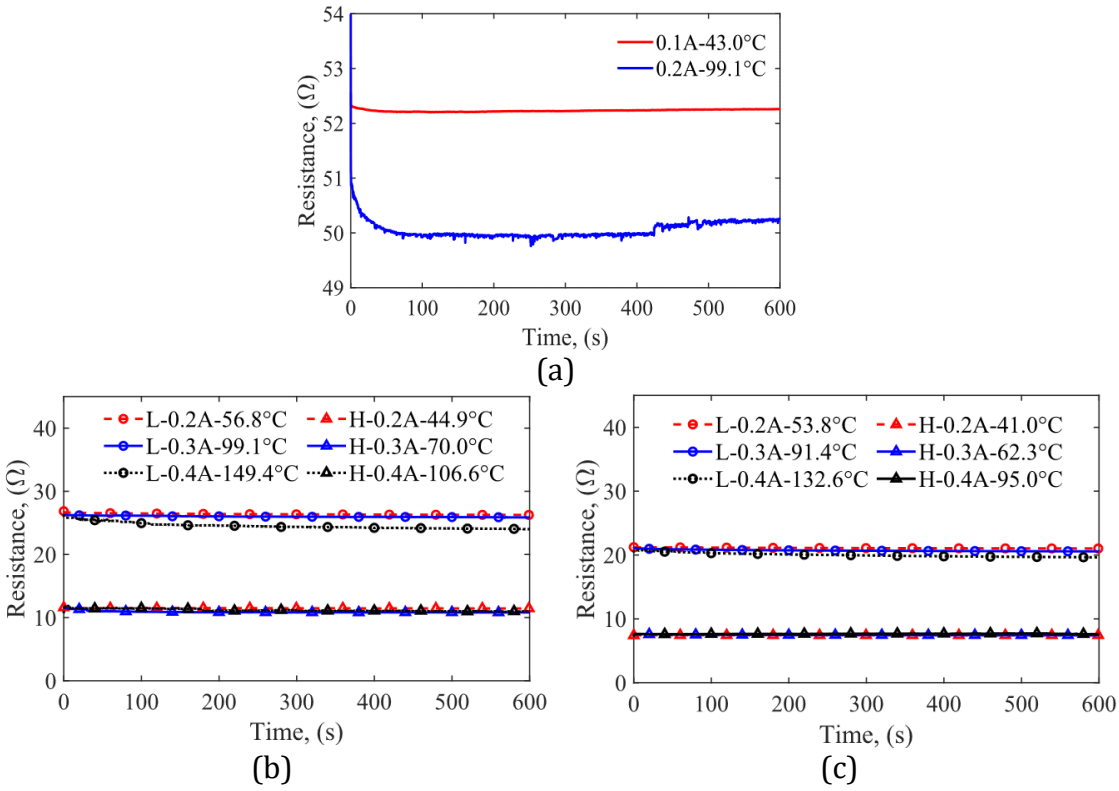

Figure 5.21: In-plane fault current response test results of (a) unpinned, (b) copper and (c) carbon-fibre Z-pinned specimens, (L: low density, H: high density).

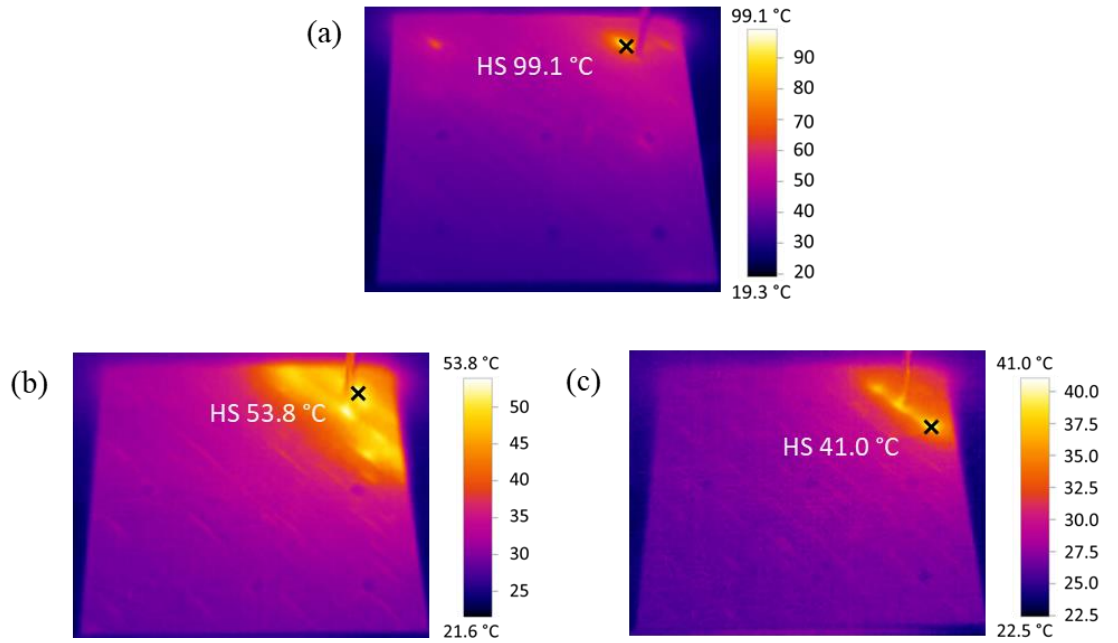

Figure 5.22: In-plane thermal images: (a) UP-0.2A, (b) CAR-L-0.2A, (c) CAR-H-0.2A.

through-thickness ones, since the current will transfer through the top surfaces firstly for both scenarios. The analyse of through-thickness fault current above is also applicable to the in-plane direction.

5.5 Conclusions

This chapter investigates the behaviour of Z-pinned laminates under electrical current experimentally. Two scenarios related to the in-plane and through-thickness fault current were studied for a QI composite laminate made from M21/ IMA prepreg, which is an interlayer toughened material system. Two kinds of pin materials (T300/ BMI composite and copper) were used at two different volume fractions (0.1% and 0.25%). Different current input areas were designed on the top surface to have a comprehensive understanding. A good consistency of the test result was achieved with a selected test set-up.

Several conclusions could be drawn here:

- The through-thickness resistance was reduced by two orders with Z-pins, due to the fibre crimping in the pin vicinity. The pin itself is not engaged in the current path network, because of the resin pocket and interfacial cracking.
- The in-plane conductivity was improved, not as significantly as the through-thickness direction, but still obvious for some chafing locations, for instance, up to one order at position 7.
- The carbon-fibre pinned samples have smaller resistance compared with the copper pinned ones due to a better manufacturing quality. The resistance decreases with the pining areal density, as more conductive paths were generated.
- When suffering from the same amount of fault current, the temperature of unpinned sample is much higher than Z-pinned ones.
- The heat flow distribution on the outer surfaces of Z-pinned laminates differs from the unpinned ones. The relative position of the pins and chafing areas are the determining factors.

In summary, this work shows that there is a notable enhancement of the electrical conductivity of CFRP laminates with Z-pins inserted, especially in the through-thickness direction. Unlike other conductivity enhancements, such as metal meshes that have only one function and increase the laminate weight, the Z-pins also have a beneficial influence on the laminate's through-thickness mechanical properties. The conductivity improvement reduces the temperature increase due to Joule heating under fault currents.

6 EFFECTS OF Z-PINS ON THE MAGNETIC PROPERTIES OF COMPOSITES

6.1 Introduction

Traditional fibre reinforced polymer (FRP) composites are magnetically inert: they do not show any remnant magnetism and only negligible enhancement of the relative magnetic permeability [110]. The weaker magnetic properties of composites compared to other materials represent an important limitation in several applications (e.g. in electromagnetic machines) [111,112].

For instance, the rotor containment sleeves of a permanent magnet machine are normally made of carbon/glass FRP composites or weak-magnetic metals for load bearing. This generates a large non-magnetic gap between the stator and the magnet, significantly reducing the resulting electromagnetic force. Yon et al. [111] designed a magnetically semi-permeable sleeve to overcome this drawback. Based on an analytical model, they estimated that an optimum relative magnetic permeability (μ_r = 7.2) could increase the fundamental component of the air-gap flux density by 28%. A prototype machine with the sleeve made from cold-rolled

304L stainless steel ($\mu_r \approx 2$) was manufactured and tested. It showed a 20% increment of the electromotive force compared to the magnetically inert material. However, the stainless steel had a low resistivity and needed to be incorporated into a laminated assembly, making the manufacture complex and expensive. With the same purpose, Edwards et al. [112] incorporated magnetic particles into composites by employing epoxy resin film loaded with pure iron particles into laminates. By embedding one film between every adjacent ply (8 plies, 7 films), the predicted relative permeability was improved, whilst the ultimate tensile strength was reduced to 60%.

Besides electromagnetic machines, Etches et al. [113] demonstrated how tailoring the magnetic properties of composites can be potentially used for magnetic actuation of the trailing edge of a morphing aerofoil. Two magnetic materials (barium ferrite and ferrofluids) were separately embedded into hollow glass fibres. Due to the particle size and viscosity, the maximum achievable volume fraction of barium ferrite was only 3%. For ferrofluids, the filler volume fraction reached 30%. The ferrofluids-filled coupon was successfully actuated in an applied magnetic field.

Compared with the methods for improving the magnetic properties of composites reviewed above, Z-pinning offers a relatively wider material selection range, since Z-pins can be in principle made of any material that can be processed into small rods. Similar to the research on electrical and thermal properties of Z-pinned composites in [10,12,16], this chapter also places emphasis on the effects of Z-pins on the global physical properties of composites. Meanwhile, some local meso-scale analyses are also presented to better understand the global effects observed. Specimen preparation and experimental set-up are introduced in Section 6.2 and Section 6.3. The magnetic properties of single Z-pins (not inserted into a composite laminate) are first characterised in Section 6.4. Experimental results for Z-pinned laminate samples are then presented in Section 6.5. The influence of pin misalignment and volume fraction on the magnetic susceptibilities of through-thickness reinforced composites in both the in-plane and out-of-plane directions are discussed in Section 6.6.

6.2 Specimen preparation

Metallic and carbon FRP Z-pins have been widely characterised for their mechanical performance in the literature. Consideringthe targeted functionality of magnetic performance in this chapter, 0.25 mm diameter Ni80/Fe20 permalloy pins (from GoodFellow) and 0.28 mm diameter traditional T300/BMI pins were considered in this study. The Ni80/Fe20 permalloy pin possesses a significantly high magnetic permeability. As a result, it is anticipated that applying these pins within the laminates will lead to noticeable enhancements in their magnetic performance.

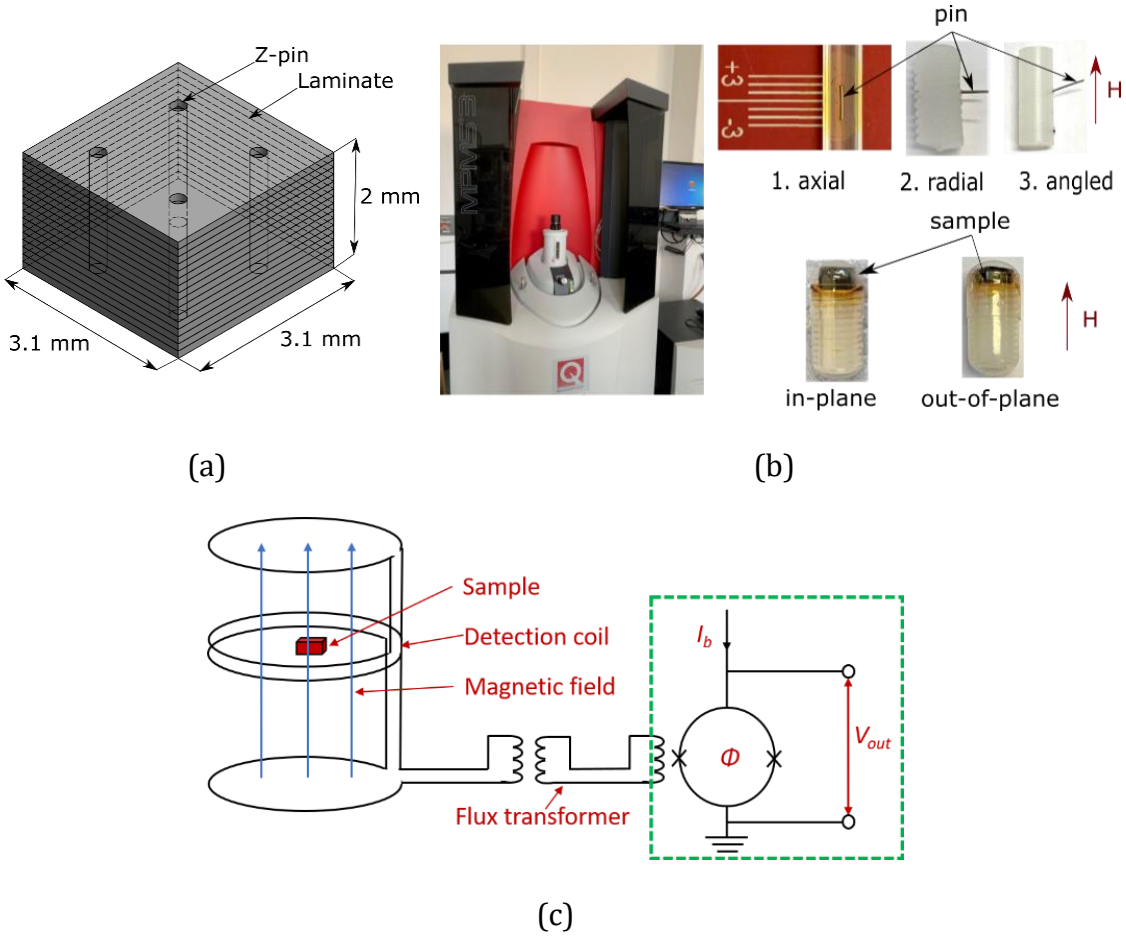

Figure 6.1: a) Nominal 2% Z-pinned coupon configuration, (b) SQUID MPMS3 and sample installations, (c) schematic of the SQUID detecting system diagram.

Z-pinned laminate specimens were manufactured employing 16 plies of Hexcel's IM7/8552 carbon/toughened-epoxy prepreg, with a stacking sequence of $[0°/+45°/90°/-45°]_{2s}$. This QI stacking sequence is a representative configuration for laminates in many structural applications. The maximum sample in-plane diagonal length allowed was 4.8 mm, due to the configuration of the sample holder in the MPMS3 magnetometer. Considering the pin spacing for nominal 0.5%, 2% and 4% volume fractions, the Z-pinned coupons were designed to have the dimensions of 3.1×3.1×2 mm. Figure 6.1(a) shows the configuration of a 2% pinned coupon as an example.

The manufacturing process consisted of four steps. (1) The prepreg was defrosted for 2 hours and laid up to form the laminate, with de-bulking after every four plies. (2) The carbon-fibre pins were cut from a protruded rod stock and the alloy pins were cut from a wire roll with scissors; then both types of Z-pins were manually inserted into the uncured laminate. (3) The Z-pinned laminate was cured in an autoclave, following the cycle recommended by Hexcel [80]. (4) Finally, the coupons were carefully cut from the cured laminate using a water-cooled diamond-coated saw.

6.3 Experimental set-up

A SQUID (Superconducting Quantum Interference Device) magnetometer model MPMS3 manufactured by Quantum Design was used in DC scan mode in this research (Figure 6.1(b)). The SQUID DC mode measures directly the magnetic flux of the sample utilizing the Josephson effect, which employs interference of the wave function around a superconducting loop where the magnetic flux of the sample is coupled in via a flux transformer. Usage of gradiometer coils removes the signal from the applied magnetic field, allowing to detect the magnetic flux from the sample as the sample is moved through the gradiometer. From the measurement of the flux as a function of position in the gradiometer, the magnetic moment of the sample is extracted using the MPMS3 software calibrated on a palladium standard [114,115]. A simplified schematic of the measurement system

is drawn in Figure 6.1(c), with the SQUID highlighted in the dashed green box, in which I_b is the bias current, Φ is the flux threading the SQUID, and V_{out} is the voltage responding to the flux. The magnetic field in the MPMS3 is generated by a superconducting electromagnet.

As shown in Figure 6.1(b), the applied magnetic field was always in the vertical direction. For the axial direction tests, a single z-pin (not inserted into the composite) was glued on a quartz rod with a semicircle cross section and the pin axis was aligned with the magnetic field direction. For the radial and angled pin tests, due to the pin tending to align itself with the applied magnetic field, it was inserted into a fixed nylon holder, to eliminate any rotation. The magnetic field was along the pin radius direction for radial tests, and there was an angle between the magnetic field and pin axis for the angled pin tests.

The Z-pinned laminate coupons were glued onto the nylon support cylinder and put into a capsule. Nylon contributes a negligible background signal as its permeability deviates less than 10^{-5} from that of free space [116], i.e. $1< \mu_r <1+10^{-5}$. The magnetic field was applied along the 0° ply fibre direction (x axis) for the in-plane measurements, whilst the magnetic field was along the specimen thickness direction (z axis) for the out-of-plane measurements.

In order to get a full M-H loop, the applied magnetic field H_0 was increased linearly from zero to a field H_{max} sufficient to observe magnetisation saturation, then decreased to $-H_{max}$, and finally brought back to H_{max}. The total duration of one scan was 1.5 to 2 hours. Each scan was repeated twice to ensure the reliability of data.

6.4 Single pin results

In the experiments, the total magnetic moment of a sample was measured and converted into an effective magnetisation using the measured sample volume. All M-H curves shown below present this effective magnetisation M_{eff} against the external field H_0. Note that the magnetisation is nonuniform inside the sample as we show later in detail in the simulations. The effective magnetic susceptibility χ_0 of the tested samples is extracted from linear fitting in the low-field regime of the

M-H curve. From this point, the low-field relative permeability is calculated as $\mu_r = \chi_0 + 1$.

6.4.1 Carbon-fibre pins

In the DC SQUID option, a resolution of 10^{-9} A·m^2 is achieved by measuring a gel capsule in a straw with the standard setup. For an individual carbon pin with its small volume (diameter: d = 0.28 mm, length: l = 4 mm), however, the magnetic moment is too small to be detected. This is consistent with the expected magnetic moment $m \approx 7 \times 10^{-11}$ A·m^2 in a field of $\mu_0 H_0 = 0.1$ T for a sample of this size containing pure graphite [117].

6.4.2 Ni/Fe pins

6.4.2.1 Susceptibility vs. length

Firstly, the effect of cure on the Ni/Fe Z-pin magnetic properties can be ignored, which was confirmed by testing a pin before and after curing and observing that the resulting M-H curves were the same.

The intrinsic magnetic permeability of Ni80/Fe20 permalloy is quite high [118], however, in a finite size volume, the effects of demagnetisation give rise to a complex variation of magnetisation M across the volume and hence the magnetic moment has a non-linear dependence on magnetic field. In some limited cases, the demagnetizing factor N can be used to obtain the internal field H as $H = H_0 - NM$. As reported [119,120], the demagnetizing factor N of a cylinder is a complex function of the susceptibility and ratio of length to diameter as well as the orientation of the magnetic field. In small magnetic fields, a linear dependence can be approximated using the demagnetizing factor N depending on the sample shape and orientation in magnetic field only [121]. In this work the non-linear regime was also studied, and FE analysis was used to model the behaviour of the samples, as analytical expressions are not available.

Since the Ni/Fe pin has a constant diameter of 0.25 mm, pins with lengths ranging from 1.5 to 4.1 mm in both the axial and radial directions were characterised. The experimental single-pin M-H curves are plotted in Figure 6.2(a, b). The slightly horizontal offset of the M-H curves is most likely due to the remnant field in the superconducting magnet following previous measurements at large magnetic fields.

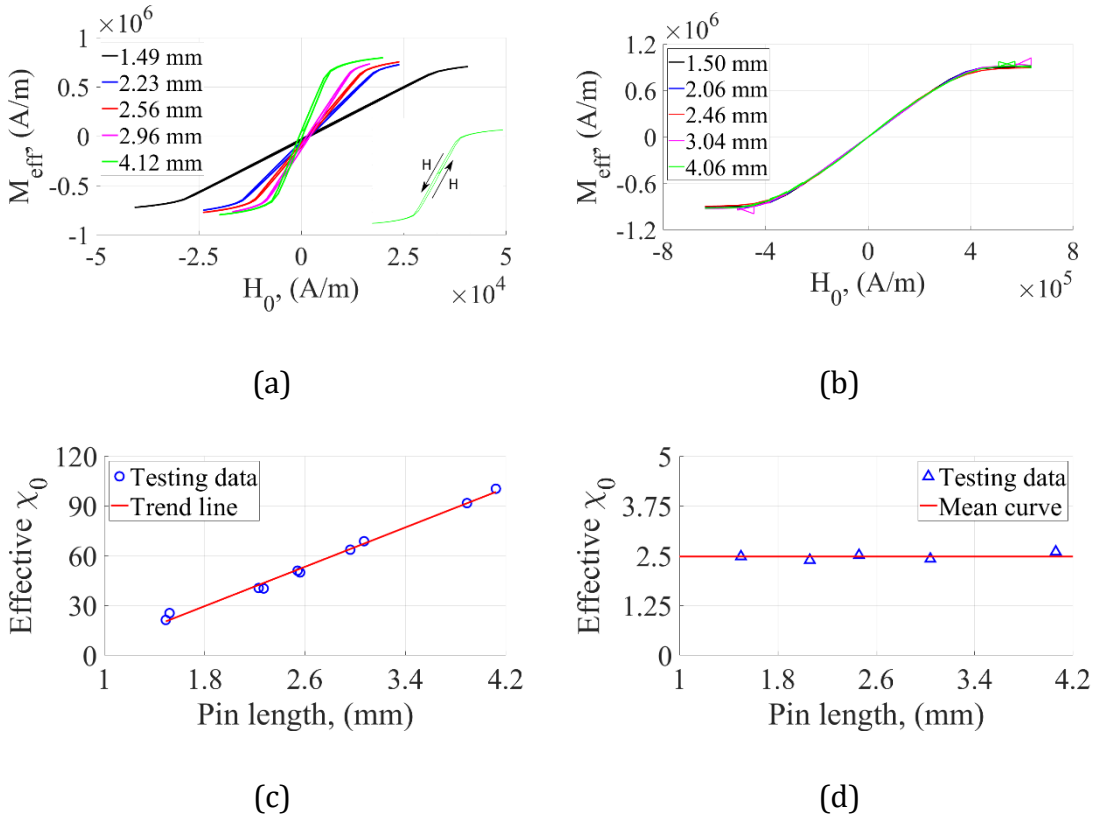

Figure 6.2: Ni/Fe pin experimental results: (a) axial M-H curves, (b) radial M-H curves, (c) axial linear-part effective susceptibility against pin length, (d) radial linear-part effective susceptibility against pin length.

For both directions, the magnetisation initially increases linearly with the applied magnetic field H_0, then, following a nonlinear response stage, it quickly reaches saturation. The curves also reveal the very soft ferromagnetic behaviour of these permalloy pins, as they have narrow hysteresis loops with very small coercive field and remanence [118]. For the axial orientation, the slope of the low-field linear regime is larger for longer samples and the non-linear response is shifted to lower

fields for longer samples, while the radial M-H behaviour is almost coincident for all samples. The saturation magnetisation M_s is independent of pin length for both directions.

For a quantitative analysis, the low-field susceptibilities are plotted against the pin length in Figure 6.2(c, d). This shows that the susceptibility for axial field orientation increases linearly from 21 to 100 with the pin length growing from 1.5 to 4.1 mm. Conversely, the values for radial orientation of the field are much lower, having a mean value of 2.5. In the low-field limit, the magnetic behaviour of the alloy pins can be captured as that of a cylinder in an axial field with a demagnetizing factor, in agreement with the linear M-H curve seen in the measurements at low fields. The demagnetizing factor N_z decreases with the length to diameter ratio in agreement with the increased effective susceptibility found in these measurements [119,120]. At the same time, the demagnetizing factor N_x relating with the radially applied magnetic field is much higher than N_z for a long thin cylinder [122] and relatively independent of the pin length, in agreement with the experimental results.

6.4.2.2 Susceptibility vs. inclination angle

Since pin misalignment is a common and unavoidable manufacturing feature in Z-pinned laminates, the effect of the inclination angle α (the angle between pin axis and magnetic field) is explored. The out-of-plane misalignment angle usually varies between 5° and 20° [96]. A 4.05 mm Ni/Fe pin was tested at pre-defined 0°, 20°, 40°, 60°, 70° and 90° inclination angles with an accuracy of ±2°.

The experimental M-H curves are plotted in Figure 6.3(a). The curves show a decrease of the initial slope and increase of the saturation field as the inclination angle increases, whilst the saturation magnetisation remains independent on the angle. The calculated saturation flux density B_s is around 1.1 T, which is consistent with the data for 80% nickel permalloy from literature [118]. The low-field susceptibilities are extracted and plotted in Figure 6.3(b) as a function of the inclination angle. A nonlinear decrease trend is observed as the inclination angle increases.

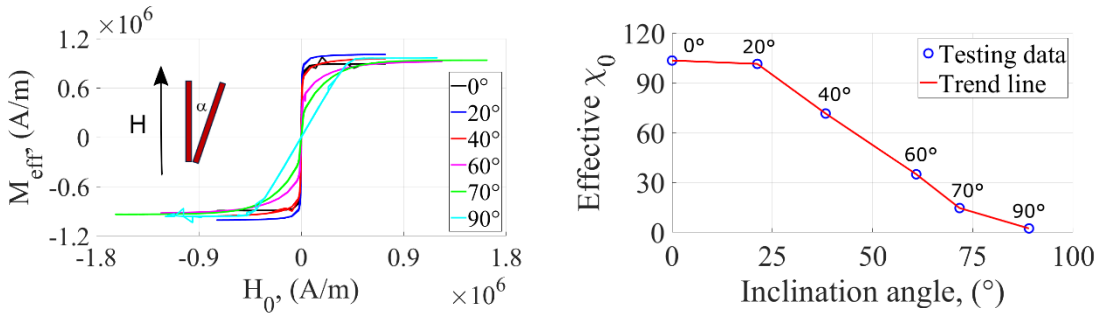

(a) (b)

Figure 6.3: Misaligned Ni/Fe pin experimental results: (a) M-H curves, (b) linear-part effective susceptibility against inclination angle.

6.5 Laminate results

6.5.1 Unpinned laminate

The individual sample dimensions for the unpinned CFRP coupons were 3.2 mm × 3.1mm × 2.0 mm. Since the laminate has a QI stacking sequence, it is expected to exhibit negligible differences in magnetic properties for any arbitrary in-plane direction.

The out-of-plane and in-plane M-H curves of the unpinned specimen are plotted in Figure 6.4(a). They present linear decreasing trends, and no saturation and hysteresis were observed even at much higher H_{max} values than those employed in the characterisation of alloy Z-pins. This confirms that the CFRP considered here is a weakly diamagnetic material [123]. The in-plane and out-of-plane M-H curves almost coincide, with susceptibility values of -5.37×10^{-5} and -5.63×10^{-5}, respectively.

6.5.2 Carbon-fibre Z-pinned laminate

Three carbon-fibre Z-pin pinned coupons with different pin volume fractions were tested. The actual volume fractions were calculated at 0.51%, 2.00% and 4.46%, by accurately measuring the specimen dimensions and the pin length (including the small amount of protruding top and bottom).

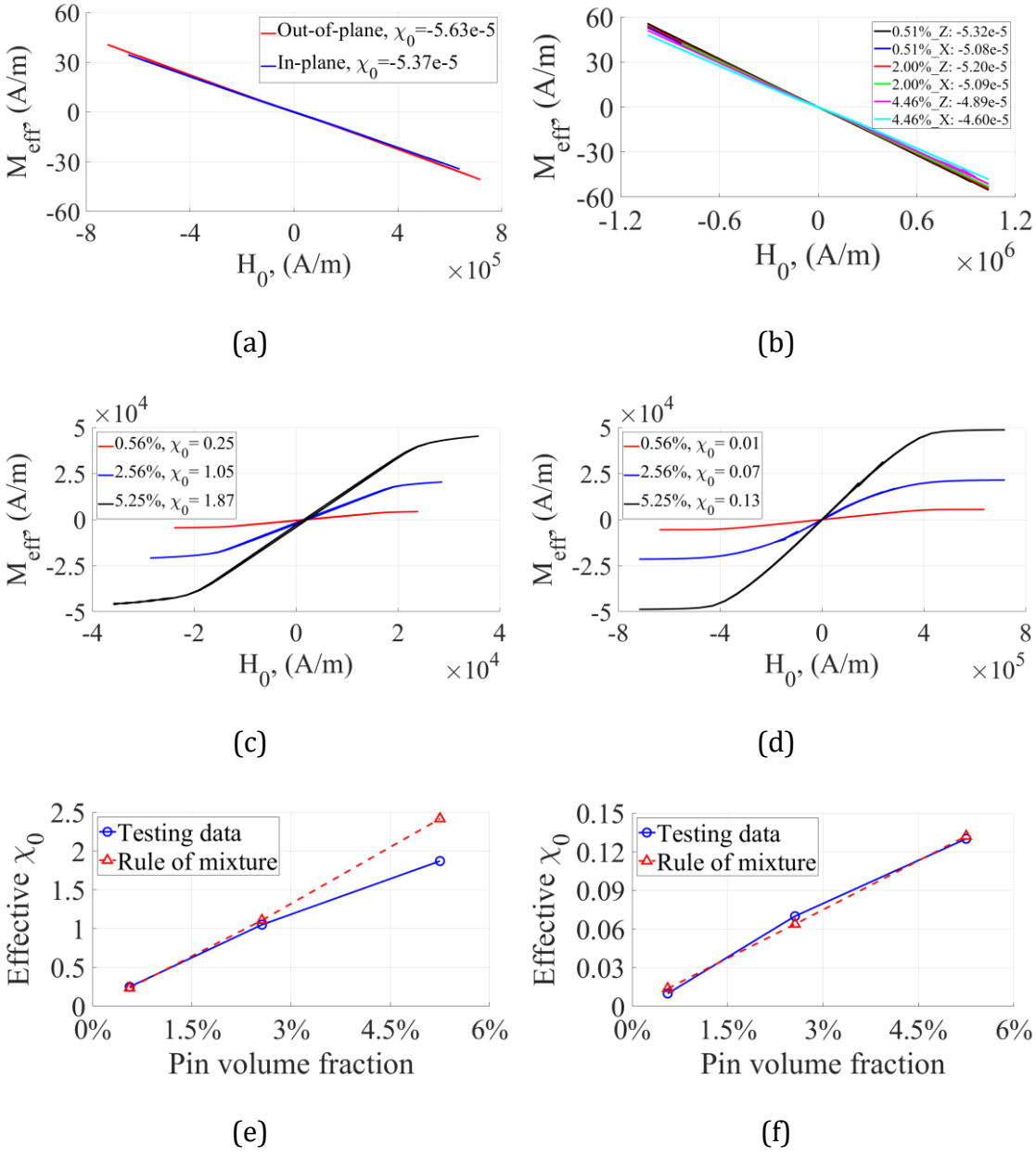

Figure 6.4: (a) M-H curves of the unpinned sample, (b) M-H curves of carbon FRP Z-pinned samples (out-of-plane: Z, in-plane: X); Ni/Fe Z-pinned samples M-H curves: (c) out-of-plane, (d) in-plane; linear-part effective magnetic susceptibility against the Ni/Fe pin volume fraction: (e) out-of-plane, (f) in-plane.

The in-plane and out-of-plane M-H curves are plotted in Figure 6.4(b), with the corresponding susceptibilities χ_0 listed in the legend. Similar to the case of the unpinned CFRP, all curves present small monotonically decreasing trends, which

implies that carbon Z-pinned laminates are also diamagnetic in both in-plane and out-of-plane directions. It appears that the absolute value of the susceptibility decreases with the pin volume fraction for both directions. The out-of-plane susceptibility is quite close to that of the in-plane direction. Compared with unpinned CFRP (i.e., comparing Figure 6.4(a) and (b)), the carbon fibre Z-pin reinforced coupons present effective susceptibilities with the same order of magnitude as for unpinned CFRP. This proves that carbon fibre pins have no large influence on the global magnetic susceptibility of a CFRP laminate.

6.5.3 Ni/Fe Z-pinned laminate

The actual pin volume fractions for the samples reinforced with alloy pins were measured at 0.56%, 2.56% and 5.25%, respectively. The corresponding experimental M-H curves are plotted in Figure 6.4(c, d). The curves have similar trends to those for the single Ni/Fe pin tests. The saturation magnetisation M_s increases with the pin volume fraction for both in-plane and out-of-plane directions. Similar to the results on single alloy pins, M_s is independent from the field direction for a given pin volume fraction (i.e. comparing the same-colour curves in Figure 6.4(c) and (d)).

As shown in the legends of Figure 6.4(c, d), low-field effective susceptibilities in the linear response region for the 0.56%, 2.56%, 5.25% pinned samples are 0.25, 1.05, 1.87 (out-of-plane) and 0.01, 0.07, 0.13 (in-plane), respectively. Compared with the diamagnetic unpinned coupon, the laminate with Ni/Fe Z-pins become strongly paramagnetic, with large susceptibilities. The low-field susceptibilities against pin volume fractions are plotted with solid lines in Figure 6.4(e) and (f). For comparison, the dashed trend lines in Figure 6.4(e) and (f) are given by the rule of mixtures:

$$\chi_{0\_sample} = \left(1 - V_{f\_pin}\right) \cdot \chi_{0\_lam} + V_{f\_pin} \cdot \chi_{0\_pin} \quad (6\text{-}1)$$

where χ_{0_sample}, χ_{0_lam} and χ_{0_pin} are the effective susceptibilities of pinned sample, unpinned laminate, and pin, respectively. V_{f_pin} is the pin volume fraction. Since χ_{0_lam} was measured to be very small for both directions (in the order of 10^{-5}),

χ_{0_sample} is dominated by the pin volume fraction and susceptibility. When considering the in-plane behaviour, the experiments and analytical prediction agree well and only exhibit a slight difference for the 2.56% volume fraction sample. However, the difference is more evident for the out-of-plane direction especially at a higher pin volume fraction, which means that the magnetic susceptibility of the pinned samples does not increase linearly to the volume fraction of the soft-ferromagnetic through-thickness reinforcement. This is potentially due to the pin misalignment and interaction, which will be further investigated in the following section with the aid of finite element analysis (FEA).

6.6 Discussion

Comparing the test results for the unpinned laminate in Section 6.5.1 and the Ni/Fe Z-pinned laminate in Section 6.5.3, it can be concluded that the magnetic properties of a ferromagnetic pinned laminate are dominated by the pins. Since in Section 6.5.2 carbon-fibre pins have been shown to have minor influence on the global magnetic behaviour of composites, only the effects of Ni/Fe pins will be further discussed in this section, considering the effects of pin misalignment, interaction, and volume fraction.

6.6.1 Pin misalignment effect

As illustrated in the experiments, the saturation magnetisation M_s is independent of the inclination angle (Figure 6.3(a)), and pin length (Figure 6.2(a, b)). It has also been demonstrated in Figure 6.4(c) and (d) that M_s increases with pin volume fraction. Thus, M_s will also increase with pin misalignment since the latter leads to a larger pin volume fraction in a fixed thickness laminate with the pins running the full thickness.

The misalignment influences the low-field susceptibility of a Z-pinned laminate in four aspects. Firstly, the effective susceptibility of the laminate will increase due to the increased pin volume fraction caused by misalignment, similar to the saturation magnetisation discussed above. Secondly, the longer pin length due to

misalignment will result in a change of the demagnetizing factor in a different way for in-plane and out-of-plane orientations. The growth of pin length due to misalignment results in an apparent increase of the effective susceptibility χ_0 of a single pin for the out-of-plane direction (Figure 6.2(c)), while no obvious influence for the in-plane property (Figure 6.2(d)). Thirdly, the inclination angle due to pin misalignment has further effects on the demagnetizing factor as shown in Figure 6.3(b). For misalignment angle typically within 20° [96], it shows in Figure 6.3(b) that the segment of 0° to 20° which corresponds to the out-of-plane direction of Z-pinned laminate only slightly decreases, while the part from 90°-70° related with the laminate in-plane direction has an apparent increment. Fourthly, pin misalignment would change the pin-to-pin distance in three dimensions and thus affect the pin interaction via magnetic field. A systematic study on the effect of pin misalignment will be addressed in a separate study by taking the aforementioned aspects into account.

6.6.2 Pin volume fraction effect

6.6.2.1 Numerical modelling

The commercial FEA tool COMSOL Multiphysics® was employed to help explain the influence of pin volume fraction. The magnetic vector potential $\boldsymbol{A}$ is employed as a field variable for the element nodes in the FE models. The following equations are used for the magnetostatics case [124]:

$$\nabla \cdot \boldsymbol{B} = 0 \tag{6-2}$$

$$\boldsymbol{B} = \nabla \times \boldsymbol{A} \tag{6-3}$$

$$\boldsymbol{B} = \mu_0(\boldsymbol{H} + \boldsymbol{M}) \tag{6-4}$$

where μ_0 is the vacuum permeability. The modelling strategy is verified through the alloy pin and pinned laminate tests as presented in Sections 6.4.2 and 6.5.3.

Each of the verification models consisted of the coupon (single pin or pinned laminate) in the middle of a relatively large free-space sphere and a layered infinite

empty domain outside, as shown in Figure 6.5 by taking the 3 by 3 pin embedded laminate as an example.

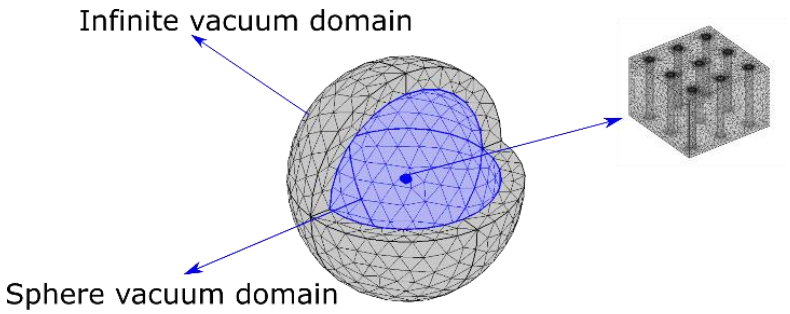

Figure 6.5: FEA model configuration and meshes (A quarter of the model is hidden to make the inner geometry visible).

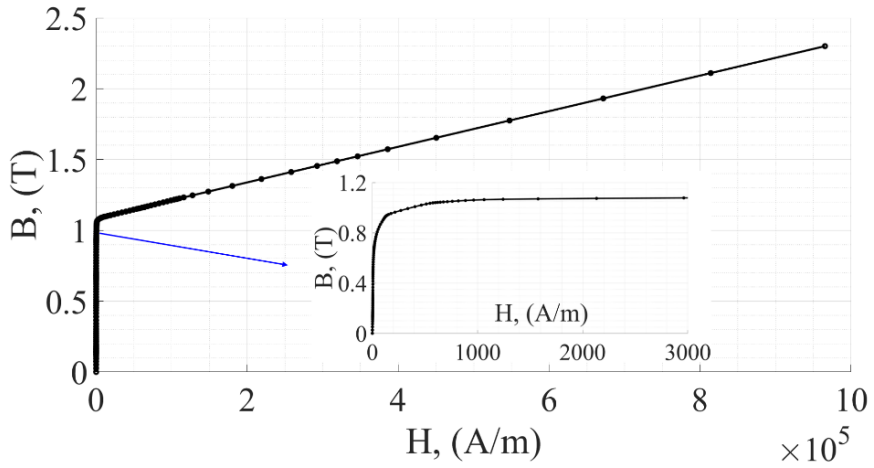

Figure 6.6: Permalloy B-H curve from the COMSOL material library [125,126].

Tetrahedral elements were employed throughout the whole mesh. For all the models presented here, mesh convergence studies have been conducted. There are 32 elements along the top or bottom circle and 16 elements per/mm in the length direction. A uniform background magnetic field was applied, which is consistent with the experimental set-up. The B-H curve of 80% nickel permalloy (Figure 6.6) from the COMSOL nonlinear magnetic material library [126] was used for the pin

in the simulation. The material data in COMSOL originates from the MagWeb database [125].

The modelling verification results are the appendix (Figure 9.8 to Figure 9.10). It shows that good agreement between experimental measurements and modelling predictions is obtained, and minor discrepancies only arise in the transition region for 60° and 70° angled pins. These differences could be attributed to the following factors. Firstly, the pins are modelled as a cylinder, while the real pin end shape is not perfectly flat after being cut with scissors. In addition, during the manufacturing process of wire such as pull-out, the grain texture inside the wire might be changed, which might influence the magnetic anisotropy and anisotropy of domain wall movements. Such magnetic anisotropy was not taken into account in the modelling. However, the overall simulation results are consistent with the experiments, especially for the most interesting linear and plateau regions of the response.

6.6.2.2 Model results discussion

When modelling the tested Ni/Fe Z-pinned coupons, the pin misalignment must be considered since it affects the magnetic properties of composites as discussed in Section 6.6.1. To measure the pin misalignment, the sample top and bottom surfaces were scanned with a microscope, then each pin was located from the scanned photos. Pin misalignment angles were determined by the distance between pin ends and sample edges. For the 1-pinned, 4-pinned and 9-pinned samples, the average misalignment angles are calculated as 9.1°, 8.4°, 6.3° respectively.

By scanning the sample top and bottom surfaces with a microscope, the pin positions were measured from the photos in Figure 6.7. The misalignment angle of each pin was calculated according to these position values. The tested Ni/Fe Z-pinned coupons were therefore modelled. Figure 6.8 shows the flux density distribution inside pins.

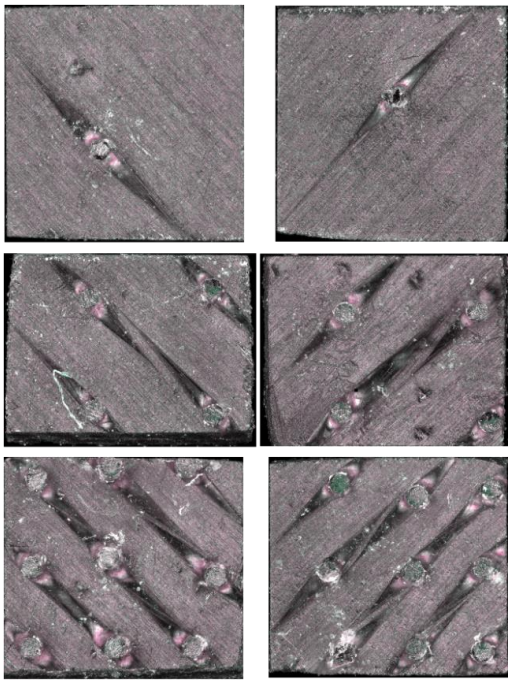

Figure 6.7: Scanning photos of Ni/Fe specimens.

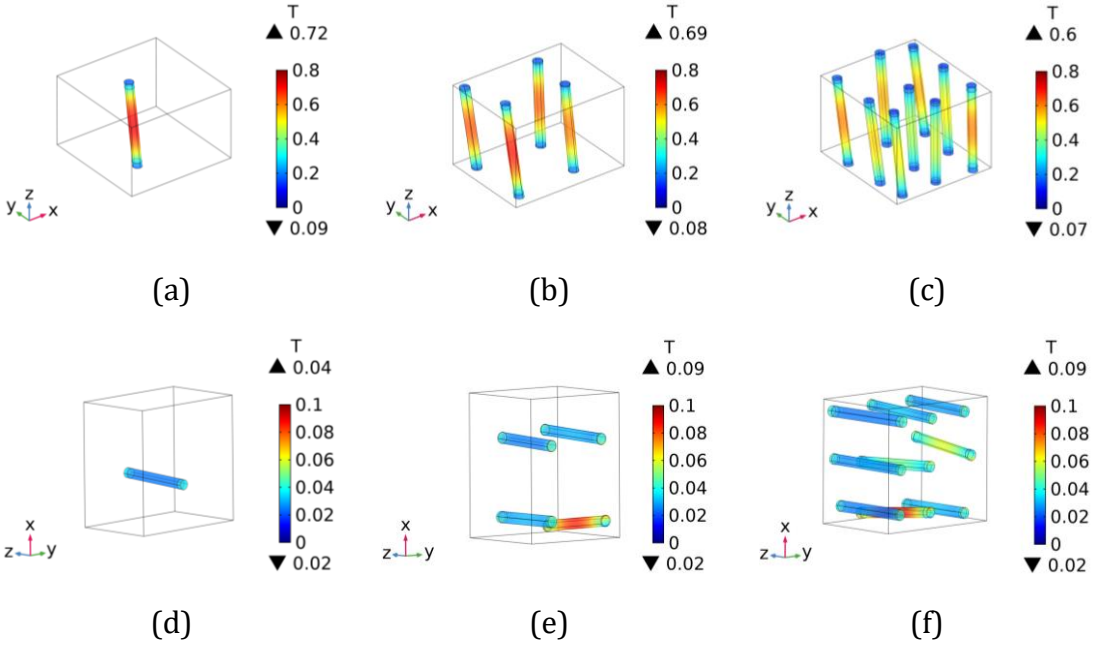

Figure 6.8: Flux density norm of Ni/Fe Z-pinned samples with 10000 A/m magnetic field applied: (a-c) out-of-plane (d-f) in-plane.

In order to study the volume fraction effect, three ideal coupons (all having 3.1 ×3.1 ×2 mm^3 dimensions) respectively comprising 1, 4 and 9 pins were modelled with all the pins perfectly straight, without protruding parts.

The linear-region susceptibility versus pin volume fraction curves of the three models are plotted in Figure 6.9 (a, b). Similar with the experimental findings reported in Figure 6.4(e, f), the out-of-plane curves from the simulations present a clearly nonlinear trend and it does not follow the rule of mixture in Figure 6.9(a). On the other hand, the rule of mixture gives good results for the in-plane curves, as seen in Figure 6.9(b).

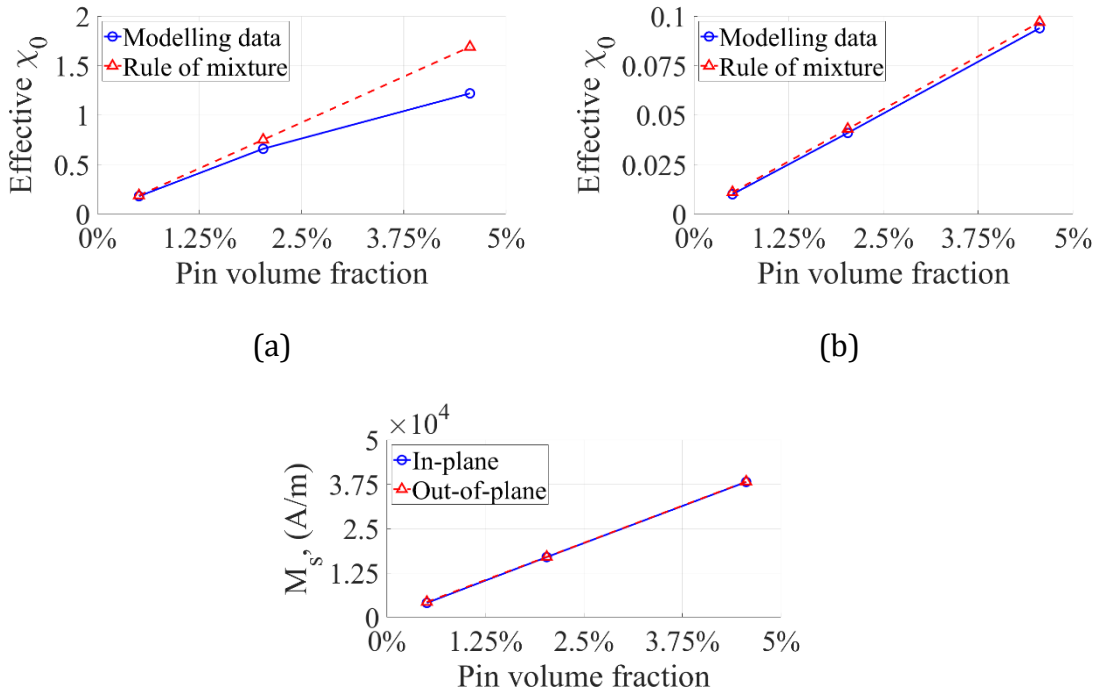

Figure 6.9: Modelling result of ideal Ni/Fe Z-pinned samples: (a) out-of-plane linear-part effective magnetic susceptibility against pin volume fraction, (b) in-plane linear-part effective magnetic susceptibility against pin volume fraction, (c) saturation magnetisation against pin volume fraction.

To understand this, the cross-section flux distribution given in Figure 6.10 must be considered. For easy comparison, the colour bar ranges were set equal for each direction, and the maximum and minimum flux values are listed beside the triangle

symbols in the graphs. For a single pin in the axial direction (out-of-plane), the flux is maximal at the pin centre (Figure 6.10(a)) due to the focusing of flux by the high permeability of the material. In the radial direction, the flux is homogeneous over most of the pin with a small increase at the ends (Figure 6.10(d)).

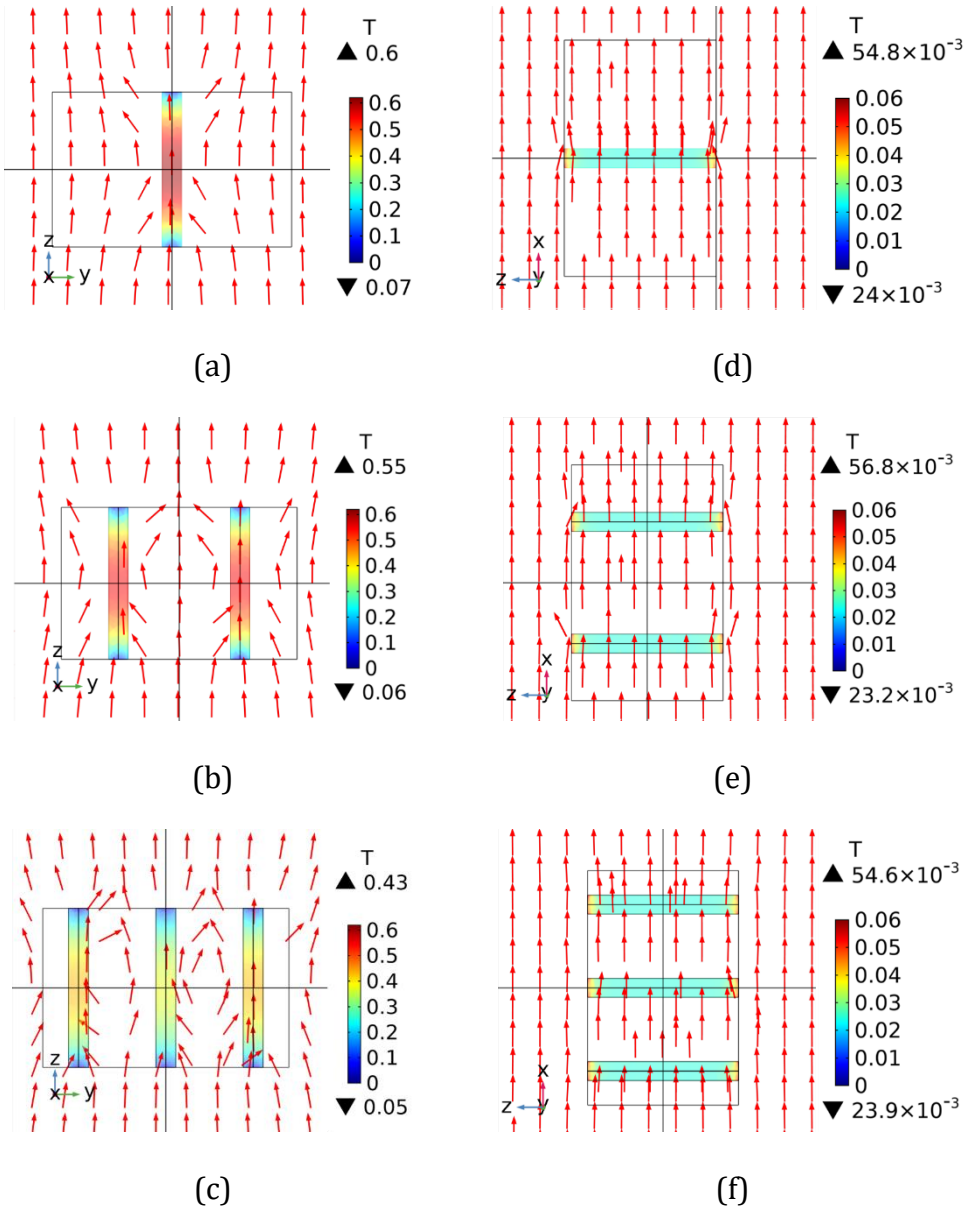

Figure 6.10: Cross section flux density norm of pins and distribution around them (modelling result of three ideal Ni/Fe Z-pinned samples with the 10000 A/m magnetic field applied): (a-c) out-of-plane (d-f) in-plane.

For multiple pins, the flux density from the external field is distributed over several pins and thus limits the enhancement of magnetisation compared to the

case of a single pin. Furthermore, the extent of this flux sharing increases with the pin volume fraction and decreases with the pin spacing (comparing Figure 6.10(b) and (c)). There are no observable interactions between pins when the magnetic field is applied transversely, and the flux density and distribution inside each pin show no significant dependence on pin volume fraction.

The saturation magnetisation M_s as a function of pin volume fraction is plotted in Figure 6.9(c). This shows that the M_s is proportional to volume fraction for both directions and independent from the magnetic field direction, as the in-plane and out-of-plane curves completely coincide. This is simply because the pin volume fraction determines the number of atomic magnetic moments per unit volume. The observation also explains the experimental results for Ni/Fe pinned coupons reported in Section 6.5.3.

6.7 Conclusions

In this chapter, the magnetic properties of Z-pinned CFRP laminates have been investigated experimentally and numerically. A commercial SQUID magnetometer was used to test the magnetic moment of single pins, unpinned and Z-pinned samples. The experiment result shows that:

- The magnetic moment of an individual carbon pin is too small to be detected, even if the SQUID has a resolution of 10^{-9} A·m^2 in the DC option.
- Soft ferromagnetic Ni/Fe Z-pins lead to a much larger magnetic susceptibility in the axial direction than in the radial one.
- Both unpinned and carbon pinned samples are weakly diamagnetic.
- Carbon-fibre Z-pins do not have large influence on the global magnetic properties of composites.
- Ni/Fe pins enhance the laminate out-of-plane and in-plane low-field linear-region effective susceptibilities up to 1.87 and 0.13 at 5.25% volume fraction, respectively.

- The low-field linear-region effective susceptibility of Ni/Fe pinned laminate increases with pin volume fraction nonlinearly, but linearly for the in-plane orientation.

Through the FEA modelling, it was found that the nonlinearity between effective susceptibility and pin volume fraction in the out-of-plane direction was due to pin interactions. There is competition on flux density between pins when an external magnetic field is applied along the pin axial direction, and this competition increases as the pin spacing decreases. The FEA modelling result also confirms that the global saturation magnetisation is only dependent on pin volume fraction and independent from field direction.

In summary, it was found feasible to tailor the magnetic properties of composites through controlling the volume fraction of ferromagnetic pins. Embedding ferromagnetic through-thickness reinforcement in FRP laminates can widen the application range of FRP composites in electromagnetic applications. In the future, it would be worthwhile to apply this kind of Z-pinned laminate to real structures.

7 CONCLUSIONS

7.1 Mechanical behaviour

In contrast to the well-explored crack propagation resisting ability of Z-pinning in flat panels, through the study of Z-pinned curved laminates under four-point bending, it was found that the carbon-fibre pins cause a reduction in the TTS. The diamond particle coated metal pins perform better than carbon-fibre pins. They have a notable enhancement on the first load-drop TTS, while the ultimate TTS is still lower than that of unpinned specimens. And the loss of TTS increases with the Z-pin volume fraction for both pin materials, which is similar to the in-plane strength reductions, as reported in the literature.

The carbon-fibre pins were mostly ruptured during the test without forming a large bridging zone to dissipate the energy, causing Z-pinning not to be effective in this damage initiation case. The reduction of TTS is mainly attributed to the microstructural features brought by the pins, e.g. stress concentrations around the holes, along with through-thickness residual stress, which has been proved by the FE modelling.

In summary, through the experimental and numerical studies, it demonstrated that whilst Z-pinning could have a positive effect for application cases where large propagating cracks need to be controlled, care should be taken in their use for

cases where failure is initiation dominated. In these cases, the use of Z-pins could be detrimental. In the future work, it is interesting to know if the use of ductile or higher-strength composite pins will show different effects on the TTS of composite laminates.

7.2 Electrical performance

The study on the localised fault current response of laminates with carbon-fibre pins and copper pins revealed that the through-thickness resistance reduction by two orders with Z-pins is due to fibre crimping in the pin vicinities. The resin pocket and interfacial cracking arount the pins prevent them from engaging in the current path network. The improvement on the electrical conductivities increases with Z-pin volume fraction, but not related with the pin material. Carbon-fibre pinned samples exhibit smaller resistance compared to copper pinned ones due to superior manufacturing quality and less thermal expansion coefficient mismatch between the pin and host laminate. This improvement can mitigate Joule heating induced temperature increments, keeping the structure in a safer working margin.

However, this study is limited to static small currents. In the future, exploring the behaviour of Z-pinned laminates under other scenarios would be of interest. Electrical models are also preferred to help design and optimise Z-pinned laminates in their electrical applications, as experimental cost is high if a range of parameters are considered.

7.3 Magnetic property

The measurement of magnetic properties of unpinned and Z-pinned specimens revealed that both unpinned and carbon-fibre Z-pinned samples exhibit weak diamagnetic behaviour. The carbon-fibre Z-pins have little influence on the global magnetic properties of composites. Despite the high intrinsic magnetic permeability of Ni/Fe permalloy, the magnetic permeability is significantly reduced when shaped into a finite-size volume due to the demagnetizing factor. When incorporated into a laminate, the Ni/Fe pins improve the laminate's out-of-

plane and in-plane effective susceptibilities up to 1.87 and 0.13, respectively. The effective susceptibility of Ni/Fe pinned laminates increases nonlinearly with pin volume fraction in the through-thickness direction due to pin interactions, as validated by the FE modelling.

One potential application based on this research is non-contact sensing, which has been successfully validated in Ref. [19] for mode I and mode II tests. This sensing function with magnetic pins could be extended to the structural level in the future. Additionally, it might be able to use Z-pinned laminates for the rotor containment sleeves, but as the structure is quite complex, the manufacturing and overall cost needs attention. Moreover, this type of Z-pins could also be used to actuate morphing structures.

8 BIBLIOGRAPHY

[1] D.H.-J.A. Lukaszewicz, C. Ward, K.D. Potter, The engineering aspects of automated prepreg layup: History, present and future, Compos. Part B Eng. 43 (2012) 997–1009. https://doi.org/10.1016/j.compositesb.2011.12.003.

[2] A.P. Mouritz, Review of z-pinned composite laminates, Compos. Part Appl. Sci. Manuf. 38 (2007) 2383–2397. https://doi.org/10.1016/j.compositesa.2007.08.016.

[3] A.P. Mouritz, Review of z-pinned laminates and sandwich composites, Compos. Part Appl. Sci. Manuf. 139 (2020) 106128. https://doi.org/10.1016/j.compositesa.2020.106128.

[4] K. Dransfield, C. Baillie, Y.-W. Mai, Improving the delamination resistance of CFRP by stitching—a review, Compos. Sci. Technol. 50 (1994) 305–317. https://doi.org/10.1016/0266-3538(94)90019-1.

[5] R. Gerlach, C.R. Siviour, J. Wiegand, N. Petrinic, In-plane and through-thickness properties, failure modes, damage and delamination in 3D woven carbon fibre composites subjected to impact loading, Compos. Sci. Technol. 72 (2012) 397–411. https://doi.org/10.1016/j.compscitech.2011.11.032.

[6] G. Dell'Anno, J.W.G. Treiber, I.K. Partridge, Manufacturing of composite parts reinforced through-thickness by tufting, Robot. Comput.-Integr. Manuf. 37 (2016) 262–272. https://doi.org/10.1016/j.rcim.2015.04.004.

[7] J. Cheng, Y. Xu, W. Zhang, W. Liu, A review on the multi-scale simulation of Z-pinned composite laminates, Compos. Struct. 295 (2022) 115834. https://doi.org/10.1016/j.compstruct.2022.115834.

[8] V. Kostopoulos, N. Sarantinos, S. Tsantzalis, Review of Through-the-Thickness Reinforced z-Pinned Composites, J. Compos. Sci. 4 (2020) 31. https://doi.org/10.3390/jcs4010031.

[9] H. Ju, K.-H. Nguyen, S.-S. Chae, J.-H. Kweon, Delamination strength of composite curved beams reinforced by grooved stainless-steel Z-pins, Compos. Struct. 180 (2017) 497–506. https://doi.org/10.1016/j.compstruct.2017.08.018.

[10] B. Zhang, G. Allegri, M. Yasaee, S.R.R. Hallett, I.K.K. Partridge, On the delamination self-sensing function of Z-pinned composite laminates, Compos. Sci. Technol. 128 (2016) 138–146. https://doi.org/10.1016/j.compscitech.2016.03.019.

[11] B. Zhang, G. Allegri, S.R. Hallett, An experimental investigation into multi-functional Z-pinned composite laminates, Mater. Des. 108 (2016) 679–688. https://doi.org/10.1016/j.matdes.2016.07.035.

[12] F. Pegorin, K. Pingkarawat, A.P. Mouritz, Controlling the electrical conductivity of fibre-polymer composites using z-pins, Compos. Sci. Technol. 150 (2017) 167–173. https://doi.org/10.1016/j.compscitech.2017.07.018.

[13] F. Pegorin, K. Pingkarawat, A.P. Mouritz, Electrical-based delamination crack monitoring in composites using z-pins, Compos. Part Appl. Sci. Manuf. 104 (2018) 120–128. https://doi.org/10.1016/j.compositesa.2017.10.025.

[14] F. Pegorin, K. Pingkarawat, A.P. Mouritz, Numerical analysis of the heat transfer properties of z-pinned composites, Compos. Commun. 8 (2018) 14–18. https://doi.org/10.1016/j.coco.2018.03.002.

[15] K. Grigoriou, R.B. Ladani, A.P. Mouritz, Electrical properties of multifunctional Z-pinned sandwich composites, Compos. Sci. Technol. 170 (2019) 60–69. https://doi.org/10.1016/j.compscitech.2018.11.030.

[16] M. Li, Z. Fang, S. Wang, Y. Gu, Y. Li, Z. Zhang, Thermal conductivity enhancement and heat transport mechanism of carbon fiber z-pin graphite

composite structures, Compos. Part B Eng. 172 (2019) 603–611. https://doi.org/10.1016/J.COMPOSITESB.2019.05.092.

[17] M. Kadlec, R. Růžek, P. Bělský, Concurrent use of Z-pins for crack arrest and structural health monitoring in adhesive-bonded composite lap joints, Compos. Sci. Technol. 188 (2020) 107967. https://doi.org/10.1016/J.COMPSCITECH.2019.107967.

[18] M. Li, Z. Fang, S. Wang, Y. Gu, W. Zhang, Thermal conductivity enhancement and synergistic heat transfer of z-pin reinforced graphite sheet and carbon fiber hybrid composite, Int. J. Heat Mass Transf. 171 (2021) 121093. https://doi.org/10.1016/j.ijheatmasstransfer.2021.121093.

[19] B. Zhang, S.R. Hallett, G. Allegri, Sensing delamination in composites reinforced by ferromagnetic Z-pins via electromagnetic induction, Compos. Sci. Technol. 217 (2022) 109113. https://doi.org/10.1016/j.compscitech.2021.109113.

[20] S.L. Huang, E.W. Deska, R.J. Richey, Cross reinforcement in a Gr/Ep laminate, 1978.

[21] G. Freitas, J.S. Boyce, C. Magee, Translaminar reinforcement system for Z-direction reinforcement of a fiber matrix structure, US5466506A, 1995. https://patents.google.com/patent/US5466506/en.

[22] G. Freitas, J.S. Boyce, C. Magee, Translaminar reinforcement system for Z-direction reinforcement of a fiber matrix structure, US5733404A, 1998. https://patents.google.com/patent/US5733404A/en.

[23] I.H. Choi, S.M. Ahn, C.H. Yeom, I.H. Hwang, D.S. Lee, MANUFACTURING OF Z-PINNED COMPOSITE LAMINATES, (n.d.).

[24] J. Toral Vazquez, B. Castanié, J.-J. Barrau, N. Swiergiel, Multi-level analysis of low-cost Z-pinned composite joints: Part 2: Joint behaviour, Compos. Part Appl. Sci. Manuf. 42 (2011) 2082–2092. https://doi.org/10.1016/j.compositesa.2011.09.017.

[25] M. Knaupp, G. Scharr, Manufacturing process and performance of dry carbon fabrics reinforced with rectangular and circular z-pins, J. Compos. Mater. 48 (2014) 2163–2172. https://doi.org/10.1177/0021998313495070.

[26] K.L. James, C. Peter, D. Ben, B. James, B. Michael, Method of manufacturing a composite component, GB2539249A, 2016. https://patents.google.com/patent/GB2539249A/en?inventor=K+Lander+James&sort=old (accessed April 2, 2023).

[27] M. Yasaee, J.K. Lander, G. Allegri, S.R. Hallett, Experimental characterisation of mixed mode traction–displacement relationships for a single carbon composite Z-pin, Compos. Sci. Technol. 94 (2014) 123–131. https://doi.org/10.1016/j.compscitech.2014.02.001.

[28] F. Warzok, Experimental and Numerical Characterisation of Fatigue Damage in Z-pinned Composite Structures, (n.d.).

[29] B. Gong, W. Ouyang, M. Nartey, H. Wang, K.D. Potter, H.-X. Peng, Minimizing the in-plane damage of Z-pinned composite laminates via a pre-hole pin insertion process, Compos. Sci. Technol. 200 (2020) 108413. https://doi.org/10.1016/j.compscitech.2020.108413.

[30] A.P. Mouritz, Compression properties of z-pinned composite laminates, Compos. Sci. Technol. 67 (2007) 3110–3120. https://doi.org/10.1016/j.compscitech.2007.04.017.

[31] A.P. Mouritz, P. Chang, Tension fatigue of fibre-dominated and matrix-dominated laminates reinforced with z-pins, Int. J. Fatigue. 32 (2010) 650–658. https://doi.org/10.1016/j.ijfatigue.2009.09.001.

[32] P. Chang, A.P. Mouritz, B.N. Cox, Flexural properties of z-pinned laminates, Compos. Part Appl. Sci. Manuf. 38 (2007) 244–251. https://doi.org/10.1016/j.compositesa.2006.05.004.

[33] P. Chang, A.P. Mouritz, B.N. Cox, Properties and failure mechanisms of z-pinned laminates in monotonic and cyclic tension, Compos. Part Appl. Sci. Manuf. 37 (2006) 1501–1513. https://doi.org/10.1016/j.compositesa.2005.11.013.

[34] I.K. Partridge, S.R. Hallett, Use of microfasteners to produce damage tolerant composite structures, Philos. Trans. R. Soc. Math. Phys. Eng. Sci. 374 (2016) 20150277. https://doi.org/10.1098/rsta.2015.0277.

[35] B. M'membe, M. Yasaee, S.R. Hallett, I.K. Partridge, Effective use of metallic Z-pins for composites' through-thickness reinforcement, Compos. Sci. Technol. 175 (2019) 77–84. https://doi.org/10.1016/j.compscitech.2019.02.024.

[36] B. M'membe, S. Gannon, M. Yasaee, S.R. Hallett, I.K. Partridge, Mode II delamination resistance of composites reinforced with inclined Z-pins, Mater. Des. 94 (2016) 565–572. https://doi.org/10.1016/j.matdes.2016.01.051.

[37] K. Pingkarawat, A.P. Mouritz, Comparative study of metal and composite z-pins for delamination fracture and fatigue strengthening of composites, Eng. Fract. Mech. 154 (2016) 180–190. https://doi.org/10.1016/j.engfracmech.2016.01.003.

[38] J. Hoffmann, J. Sabban, G. Scharr, Pullout performance of circumferentially notched z-pins in carbon fiber reinforced laminates, Compos. Part Appl. Sci. Manuf. 110 (2018) 197–202. https://doi.org/10.1016/j.compositesa.2018.05.002.

[39] A. Virakthi, S. Kwon, S.W. Lee, M.E. Robeson, Delamination resistance of composite laminated structures reinforced with angled, threaded, and anchored Z-pins, J. Compos. Mater. 53 (2019) 1507–1519. https://doi.org/10.1177/0021998318805201.

[40] A.P. Mouritz, T.M. Koh, Re-evaluation of mode I bridging traction modelling for z-pinned laminates based on experimental analysis, Compos. Part B Eng. 56 (2014) 797–807. https://doi.org/10.1016/j.compositesb.2013.09.016.

[41] E. Santana de Vega, G. Allegri, B. Zhang, I. Hamerton, S.R. Hallett, Improving the delamination bridging performance of Z-pins through the use of a ductile matrix, Compos. Part Appl. Sci. Manuf. 163 (2022) 107241. https://doi.org/10.1016/j.compositesa.2022.107241.

[42] K. Pingkarawat, A.P. Mouritz, Improving the mode I delamination fatigue resistance of composites using z-pins, Compos. Sci. Technol. 92 (2014) 70–76. https://doi.org/10.1016/j.compscitech.2013.12.009.

[43] F. Pegorin, K. Pingkarawat, S. Daynes, A.P. Mouritz, Influence of z-pin length on the delamination fracture toughness and fatigue resistance of pinned

composites, Compos. Part B Eng. 78 (2015) 298–307. https://doi.org/10.1016/j.compositesb.2015.03.093.

[44] H. Sam Huang, A.M. Waas, Quasi-static mode II fracture tests and simulations of Z-pinned woven composites, Eng. Fract. Mech. 126 (2014) 155–165. https://doi.org/10.1016/j.engfracmech.2014.05.002.

[45] F. Pegorin, K. Pingkarawat, S. Daynes, A.P. Mouritz, Mode II interlaminar fatigue properties of z-pinned carbon fibre reinforced epoxy composites, Compos. Part Appl. Sci. Manuf. 67 (2014) 8–15. https://doi.org/10.1016/j.compositesa.2014.08.008.

[46] H. Cui, M. Yasaee, G. Kalwak, A. Pellegrino, I.K. Partridge, S.R. Hallett, G. Allegri, N. Petrinic, Bridging mechanisms of through-thickness reinforcement in dynamic mode I&II delamination, Compos. Part Appl. Sci. Manuf. 99 (2017) 198–207. https://doi.org/10.1016/j.compositesa.2017.04.009.

[47] H. Cui, M. Yasaee, S.R. Hallett, I.K. Partridge, G. Allegri, N. Petrinic, Dynamic bridging mechanisms of through-thickness reinforced composite laminates in mixed mode delamination, Compos. Part Appl. Sci. Manuf. 106 (2018) 24–33. https://doi.org/10.1016/j.compositesa.2017.11.017.

[48] H. Cui, Y. Mahadik, S.R. Hallett, I.K. Partridge, G. Allegri, S.A. Ponnusami, N. Petrinic, Coupon scale Z-pinned IM7/8552 delamination tests under dynamic loading, Compos. Part Appl. Sci. Manuf. 125 (2019) 105565. https://doi.org/10.1016/j.compositesa.2019.105565.

[49] D.D.R. Cartié, G. Dell'Anno, E. Poulin, I.K. Partridge, 3D reinforcement of stiffener-to-skin T-joints by Z-pinning and tufting, Eng. Fract. Mech. 73 (2006) 2532–2540. https://doi.org/10.1016/j.engfracmech.2006.06.012.

[50] M. Li, P. Chen, B. Kong, T. Peng, Z. Yao, X. Qiu, Influences of thickness ratios of flange and skin of composite T-joints on the reinforcement effect of Z-pin, Compos. Part B Eng. 97 (2016) 216–225. https://doi.org/10.1016/j.compositesb.2016.05.007.

[51] M. Li, P. Chen, X. Li, N. Gong, Experimental and numerical study on the tensile properties of T-joints with low Z-pin volume density, Polym. Compos. 41 (2020) 258–270. https://doi.org/10.1002/pc.25366.

[52] J. Hoffmann, G. Scharr, Mechanical properties of composite laminates reinforced with rectangular z-pins in monotonic and cyclic tension, Compos. Part Appl. Sci. Manuf. 109 (2018) 163–170. https://doi.org/10.1016/j.compositesa.2018.03.004.

[53] A.P. Mouritz, Tensile fatigue properties of 3D composites with through-thickness reinforcement, Compos. Sci. Technol. 68 (2008) 2503–2510. https://doi.org/10.1016/j.compscitech.2008.05.003.

[54] C. Li, Y. Yan, P. Wang, D. Qi, Y. Wen, Study on Compressive Properties of Z-pinned Laminates in RTD and Hygrothermal Environment, Chin. J. Aeronaut. 25 (2012) 64–70. https://doi.org/10.1016/S1000-9361(11)60363-4.

[55] J. Hoffmann, G. Scharr, Compression properties of composite laminates reinforced with rectangular z-pins, Compos. Sci. Technol. 167 (2018) 463–469. https://doi.org/10.1016/j.compscitech.2018.08.042.

[56] A.P. Mouritz, B.N. Cox, A mechanistic interpretation of the comparative in-plane mechanical properties of 3D woven, stitched and pinned composites, Compos. Part Appl. Sci. Manuf. 41 (2010) 709–728. https://doi.org/10.1016/j.compositesa.2010.02.001.

[57] F. Bianchi, X. Zhang, A cohesive zone model for predicting delamination suppression in z-pinned laminates, Compos. Sci. Technol. 71 (2011) 1898–1907. https://doi.org/10.1016/j.compscitech.2011.09.004.

[58] F. Bianchi, T.M. Koh, X. Zhang, I.K. Partridge, A.P. Mouritz, Finite element modelling of z-pinned composite T-joints, Compos. Sci. Technol. 73 (2012) 48–56. https://doi.org/10.1016/j.compscitech.2012.09.008.

[59] H. Cui, Y. Li, S. Koussios, L. Zu, A. Beukers, Bridging micromechanisms of Z-pin in mixed mode delamination, Compos. Struct. 93 (2011) 2685–2695. https://doi.org/10.1016/j.compstruct.2011.06.004.

[60] H. Cui, Y. Li, S. Koussios, A. Beukers, Mixed mode cohesive law for Z-pinned composite analyses, Comput. Mater. Sci. 75 (2013) 60–68. https://doi.org/10.1016/j.commatsci.2013.04.006.

[61] F. Bianchi, X. Zhang, Predicting mode-II delamination suppression in z-pinned laminates, Compos. Sci. Technol. 72 (2012) 924–932. https://doi.org/10.1016/j.compscitech.2012.03.003.

[62] G. Allegri, M. Yasaee, I.K. Partridge, S.R. Hallett, A novel model of delamination bridging via Z-pins in composite laminates, Int. J. Solids Struct. 51 (2014) 3314–3332. https://doi.org/10.1016/j.ijsolstr.2014.05.017.

[63] G. Mohamed, G. Allegri, M. Yasaee, S.R. Hallett, Cohesive element formulation for z-pin delamination bridging in fibre reinforced laminates, Int. J. Solids Struct. 132–133 (2018) 232–244. https://doi.org/10.1016/j.ijsolstr.2017.05.037.

[64] A.R. Melro, J. Serra, G. Allegri, S.R. Hallett, An energy-equivalent bridging map formulation for modelling delamination in through-thickness reinforced composite laminates, Int. J. Solids Struct. 202 (2020) 153–165. https://doi.org/10.1016/j.ijsolstr.2020.06.018.

[65] M. Meo, F. Achard, M. Grassi, Finite element modelling of bridging micro-mechanics in through-thickness reinforced composite laminates, Compos. Struct. 71 (2005) 383–387. https://doi.org/10.1016/j.compstruct.2005.09.025.

[66] L.C. Dickinson, G.L. Farley, M.K. Hinders, Prediction of Effective Three-Dimensional Elastic Constants of Translaminar Reinforced Composites, J. Compos. Mater. 33 (1999) 1002–1029. https://doi.org/10.1177/002199839903301104.

[67] B. Zhang, G. Allegri, M. Yasaee, S.R. Hallett, Micro-mechanical finite element analysis of Z-pins under mixed-mode loading, Compos. Part Appl. Sci. Manuf. 78 (2015) 424–435. https://doi.org/10.1016/j.compositesa.2015.07.006.

[68] A.R. Melro, B. Zhang, I.K. Partridge, S.R. Hallett, PARAMETRIC CHARACTERISATION OF Z-PIN REINFORCEMENT USING HIGH-DEFINITION FE MODELLING, ECCM2018 – 18th Eur. Conf. Compos. Mater. Athens Greece. (2018) 8.

[69] M. Li, P. Chen, A new FE model for predicting the bridging micromechanisms of a Z-pin, Compos. Struct. 223 (2019) 110957. https://doi.org/10.1016/j.compstruct.2019.110957.

[70] M. Grassi, X. Zhang, M. Meo, Prediction of stiffness and stresses in z-fibre reinforced composite laminates, Compos. Part Appl. Sci. Manuf. 33 (2002) 1653–1664. https://doi.org/10.1016/S1359-835X(02)00137-9.

[71] V.L. Tagarielli, G. Minisgallo, A.J. McMillan, N. Petrinic, The response of a multi-directional composite laminate to through-thickness loading, Compos. Sci. Technol. 70 (2010) 1950–1957. https://doi.org/10.1016/j.compscitech.2010.07.013.

[72] I.M. Daniel, J.-J. Luo, P.M. Schubel, B.T. Werner, Interfiber/interlaminar failure of composites under multi-axial states of stress, Compos. Sci. Technol. 69 (2009) 764–771. https://doi.org/10.1016/j.compscitech.2008.04.016.

[73] J.-S. Charrier, F. Laurin, N. Carrere, S. Mahdi, Determination of the out-of-plane tensile strength using four-point bending tests on laminated L-angle specimens with different stacking sequences and total thicknesses, Compos. Part Appl. Sci. Manuf. 81 (2016) 243–253. https://doi.org/10.1016/j.compositesa.2015.11.018.

[74] J.M. González-Cantero, E. Graciani, B. López-Romano, F. París, Competing mechanisms in the unfolding failure in composite laminates, Compos. Sci. Technol. 156 (2018) 223–230. https://doi.org/10.1016/j.compscitech.2017.12.022.

[75] D. Ranz, J. Cuartero, A. Miravete, R. Miralbes, Experimental research into interlaminar tensile strength of carbon/epoxy laminated curved beams, Compos. Struct. 164 (2017) 189–197. https://doi.org/10.1016/j.compstruct.2016.12.010.

[76] L.B. Andraju, G. Raju, Continuum and cohesive zone damage models to study intra/inter-laminar failure of curved composite laminates under four-point bending, Compos. Struct. 253 (2020) 112768. https://doi.org/10.1016/j.compstruct.2020.112768.

[77] X. Zou, S. Yan, M. Matveev, J.P. Rouse, I.A. Jones, Experimental and numerical investigation of interface damage in composite L-angle sections under four-point bending, J. Compos. Mater. (2020) 0021998320943659. https://doi.org/10.1177/0021998320943659.

[78] X. Xu, M.I. Jones, H. Ali, M.R. Wisnom, S.R. Hallett, Effect of out-of-plane wrinkles in curved multi-directional carbon/epoxy laminates, Compos. Sci. Technol. 197 (2020) 108282. https://doi.org/10.1016/j.compscitech.2020.108282.

[79] D30 Committee, Test Method for Measuring the Curved Beam Strength of a Fiber-Reinforced Polymer-Matrix Composite, ASTM International, 2013. https://doi.org/10.1520/D6415_D6415M-06AR13.

[80] Prepreg Data Sheet | Hexcel, (2020). https://www.hexcel.com.

[81] S.C. Garcea, Y. Wang, P.J. Withers, X-ray computed tomography of polymer composites, Compos. Sci. Technol. 156 (2018) 305–319. https://doi.org/10.1016/j.compscitech.2017.10.023.

[82] X. Xu, X. Sun, M.R. Wisnom, Initial R-curves for trans-laminar fracture of quasi-isotropic carbon/epoxy laminates from specimens with increasing size, Compos. Sci. Technol. 216 (2021) 109077. https://doi.org/10.1016/j.compscitech.2021.109077.

[83] A. Knopp, G. Scharr, Effect of z-pin surface treatment on delamination and debonding properties of z-pinned composite laminates, J. Mater. Sci. 49 (2014) 1674–1683. https://doi.org/10.1007/s10853-013-7851-2.

[84] M.-G. Ko, J.-H. Kweon, J.-H. Choi, Fatigue characteristics of jagged pin-reinforced composite single-lap joints in hygrothermal environments, Compos. Struct. 119 (2015) 59–66. https://doi.org/10.1016/j.compstruct.2014.08.025.

[85] G. Seon, A. Makeev, J.D. Schaefer, B. Justusson, Measurement of Interlaminar Tensile Strength and Elastic Properties of Composites Using Open-Hole Compression Testing and Digital Image Correlation, Appl. Sci. 9 (2019) 2647. https://doi.org/10.3390/app9132647.

[86] Y.-C. Shin, S.-M. Kim, Enhancement of the Interlaminar Fracture Toughness of a Carbon-Fiber-Reinforced Polymer Using Interleaved Carbon Nanotube Buckypaper, Appl. Sci. 11 (2021) 6821. https://doi.org/10.3390/app11156821.

[87] H. Hong, K.J. Bae, H. Jung, Y. Oh, N.-H. You, J.-C. Lee, J. Yu, Preparation and characterization of carbon fiber reinforced plastics (CFRPs) incorporating through-plane-stitched carbon fibers, Compos. Struct. 284 (2022) 115198. https://doi.org/10.1016/j.compstruct.2022.115198.

[88] S.R. Hallett, B.G. Green, W.G. Jiang, M.R. Wisnom, An experimental and numerical investigation into the damage mechanisms in notched composites, Compos. Part Appl. Sci. Manuf. 40 (2009) 613–624. https://doi.org/10.1016/j.compositesa.2009.02.021.

[89] Abaqus Analysis User's Guide (6.14), (2023). http://130.149.89.49:2080/v6.14/books/usb/default.htm.

[90] S.L. Lemanski, J. Wang, M.P.F. Sutcliffe, K.D. Potter, M.R. Wisnom, Modelling failure of composite specimens with defects under compression loading, Compos. Part Appl. Sci. Manuf. 48 (2013) 26–36. https://doi.org/10.1016/j.compositesa.2012.12.007.

[91] Y. Nikishkov, A. Makeev, G. Seon, Progressive fatigue damage simulation method for composites, Int. J. Fatigue. 48 (2013) 266–279. https://doi.org/10.1016/j.ijfatigue.2012.11.005.

[92] J. Lee, C. Soutis, Measuring the notched compressive strength of composite laminates: Specimen size effects, Compos. Sci. Technol. 68 (2008) 2359–2366. https://doi.org/10.1016/j.compscitech.2007.09.003.

[93] T.A. Fletcher, T. Kim, T.J. Dodwell, R. Butler, R. Scheichl, R. Newley, Resin treatment of free edges to aid certification of through thickness laminate strength, Compos. Struct. 146 (2016) 26–33. https://doi.org/10.1016/j.compstruct.2016.02.074.

[94] W.-G. Jiang, S.R. Hallett, B.G. Green, M.R. Wisnom, A concise interface constitutive law for analysis of delamination and splitting in composite materials and its application to scaled notched tensile specimens, Int. J.

Numer. Methods Eng. 69 (2007) 1982–1995. https://doi.org/10.1002/nme.1842.

[95] J. Selvaraj, L.F. Kawashita, S.R. Hallett, Mesh independent modelling of tensile failure in laminates using mixed-time integration in explicit analysis, Eng. Fract. Mech. 259 (2022) 108113. https://doi.org/10.1016/j.engfracmech.2021.108113.

[96] M. Yasaee, J.K. Lander, G. Allegri, S.R. Hallett, Experimental characterisation of mixed mode traction–displacement relationships for a single carbon composite Z-pin, Compos. Sci. Technol. 94 (2014) 123–131. https://doi.org/10.1016/j.compscitech.2014.02.001.

[97] ASTM A283 Grade D Carbon Steel: MakeItFrom.com, (2023). https://www.makeitfrom.com/material-properties/ASTM-A283-Grade-D-Carbon-Steel.

[98] B. Sarlioglu, C.T. Morris, More Electric Aircraft: Review, Challenges, and Opportunities for Commercial Transport Aircraft, IEEE Trans. Transp. Electrification. 1 (2015) 54–64. https://doi.org/10.1109/TTE.2015.2426499.

[99] E. Karadotcheva, S.N. Nguyen, E.S. Greenhalgh, M.S.P. Shaffer, A.R.J. Kucernak, P. Linde, Structural Power Performance Targets for Future Electric Aircraft, Energies. 14 (2021) 6006. https://doi.org/10.3390/en14196006.

[100] C.E. Jones, P.J. Norman, G.M. Burt, C. Hill, G. Allegri, J. Yon, I. Hamerton, R.S. Trask, A route to sustainable aviation: a roadmap for the realization of aircraft components with electrical and structural multifunctionality, IEEE Trans. Transp. Electrification. 7 (2021) 3032–3049. https://doi.org/10.1109/TTE.2021.3078118.

[101] P. Preeti, C.E. Jones, P.J. Norman, G.M. Burt, Electrical protection solutions enabling integrated electrical power and composite structure systems for aircraft, (2022). https://core.ac.uk/display/512004144?source=2.

[102] C.E. Jones, M. Sztykiel, R. Peña-Alzola, P.J. Norman, G.M. Burt, Grounding topologies for resilient, integrated composite electrical power systems for future aircraft applications, in: 2019 AIAAIEEE Electr. Aircr. Technol. Symp. EATS, 2019: pp. 1–15. https://doi.org/10.2514/6.2019-4402.

[103] A. Piche, D. Andissac, I. Revel, B. Lepetit, Dynamic electrical behaviour of a composite material during a short circuit, in: 10th Int. Symp. Electromagn. Compat., 2011: pp. 128–132.

[104] C.E. Jones, P.J. Norman, M. Sztykiel, R. Pena Alzola, G.M. Burt, S.J. Galloway, L.F. Kawashita, S.R. Hallett, Electrical and Thermal Effects of Fault Currents in Aircraft Electrical Power Systems With Composite Aerostructures, IEEE Trans. Transp. Electrification. 4 (2018) 660–670. https://doi.org/10.1109/TTE.2018.2833838.

[105] HexPly_M21_global_DataSheet.pdf, (2022). https://www.hexcel.com.

[106] R. Sfar Zbed, S. Le Corre, V. Sobotka, Process-induced strains measurements through a multi-axial characterization during the entire curing cycle of an interlayer toughened Carbon/Epoxy prepreg, Compos. Part Appl. Sci. Manuf. 153 (2022) 106689. https://doi.org/10.1016/j.compositesa.2021.106689.

[107] M. Yasaee, I.P. Bond, R.S. Trask, E.S. Greenhalgh, Mode I interfacial toughening through discontinuous interleaves for damage suppression and control, Compos. Part Appl. Sci. Manuf. 43 (2012) 198–207. https://doi.org/10.1016/j.compositesa.2011.10.009.

[108] G. Korb, J. Koráb, G. Groboth, Thermal expansion behaviour of unidirectional carbon-fibre-reinforced copper-matrix composites, Compos. Part Appl. Sci. Manuf. 29 (1998) 1563–1567. https://doi.org/10.1016/S1359-835X(98)00066-9.

[109] C. Hagart-Alexander, Chapter 21 - Temperature Measurement, in: W. Boyes (Ed.), Instrum. Ref. Book Fourth Ed., Butterworth-Heinemann, Boston, 2010: pp. 269–326. https://doi.org/10.1016/B978-0-7506-8308-1.00021-8.

[110] J. Summerscales, Microstructural Characterisation of Fibre-Reinforced Composites, Woodhead Publishing, 1998.

[111] J.M. Yon, P.H. Mellor, R. Wrobel, J.D. Booker, S.G. Burrow, Analysis of semipermeable containment sleeve technology for high-speed permanent magnet machines, IEEE Trans. Energy Convers. 27 (2012) 646–653. https://doi.org/10.1109/TEC.2012.2202232.

[112] L.E. Edwards, J.M. Yon, I.P. Bond, P.H. Mellor, Structural magnetic composites for use in electro-mechanical applications, ICCM Int. Conf. Compos. Mater. 2015-July (2015) 19–24.

[113] J. Etches, I. Bond, P. Mellor, Manufacture and applications of magnetically active fibre reinforced composites, Smart Mater. Struct. 15 (2006) 288–294. https://doi.org/10.1088/0964-1726/15/2/007.

[114] Magnetic Property Measurement System, MPMS 3 User's Manual, (2016).

[115] M. Schmelz, R. Stolz, Superconducting Quantum Interference Device (SQUID) Magnetometers, in: A. Grosz, M.J. Haji-Sheikh, S.C. Mukhopadhyay (Eds.), High Sensit. Magnetometers, Springer International Publishing, Cham, 2017: pp. 279–311. https://doi.org/10.1007/978-3-319-34070-8_10.

[116] S. Hwang, S.-K. Lee, Efficient Experimental Design for Measuring Magnetic Susceptibility of Arbitrarily Shaped Materials by MRI, Investig. Magn. Reson. Imaging. 22 (2018) 141–149. https://doi.org/10.13104/imri.2018.22.3.141.

[117] J. Heremans, C.H. Olk, D.T. Morelli, Magnetic susceptibility of carbon structures, Phys. Rev. B. 49 (1994) 15122–15125. https://doi.org/10.1103/PhysRevB.49.15122.

[118] D. Jiles, Introduction to Magnetism and Magnetic Materials, CRC Press, 2015.

[119] D.-X. Chen, J.A. Brug, R.B. Goldfarb, Demagnetizing factors for cylinders, IEEE Trans. Magn. 27 (1991) 3601–3619. https://doi.org/10.1109/20.102932.

[120] D.-X. Chen, E. Pardo, A. Sanchez, Fluxmetric and magnetometric demagnetizing factors for cylinders, J. Magn. Magn. Mater. 306 (2006) 135–146. https://doi.org/10.1016/j.jmmm.2006.02.235.

[121] X.B. Xu, L. Zeng, Ferromagnetic cylinders in earth's magnetic field—a two-dimentional model of magnetizaion of submarine, (1998) 17.

[122] M. Sato, Y. Ishii, Simple and approximate expressions of demagnetizing factors of uniformly magnetized rectangular rod and cylinder, J. Appl. Phys. 66 (1989) 983–985. https://doi.org/10.1063/1.343481.

[123] A. Galehdar, K.J. Nicholson, P.J. Callus, W.S.T. Rowe, S. John, C.H. Wang, K. Ghorbani, The strong diamagnetic behaviour of unidirectional carbon fiber reinforced polymer laminates, J. Appl. Phys. 112 (2012) 113921. https://doi.org/10.1063/1.4764041.

[124] R. Prozorov, V.G. Kogan, Effective Demagnetizing Factors of Diamagnetic Samples of Various Shapes, Phys. Rev. Appl. 10 (2018) 1. https://doi.org/10.1103/PhysRevApplied.10.014030.

[125] Nickel Steel, MAGWEB. (2021). https://magweb.us/product/nickel-steel/.

[126] Multiphysics Simulations Material Library - Adding Material Properties, (2021). https://www.comsol.com/material-library.

9 Appendices

APPENDIX 1 SUPPLEMENTARY MATERIAL FOR CHAPTER 3

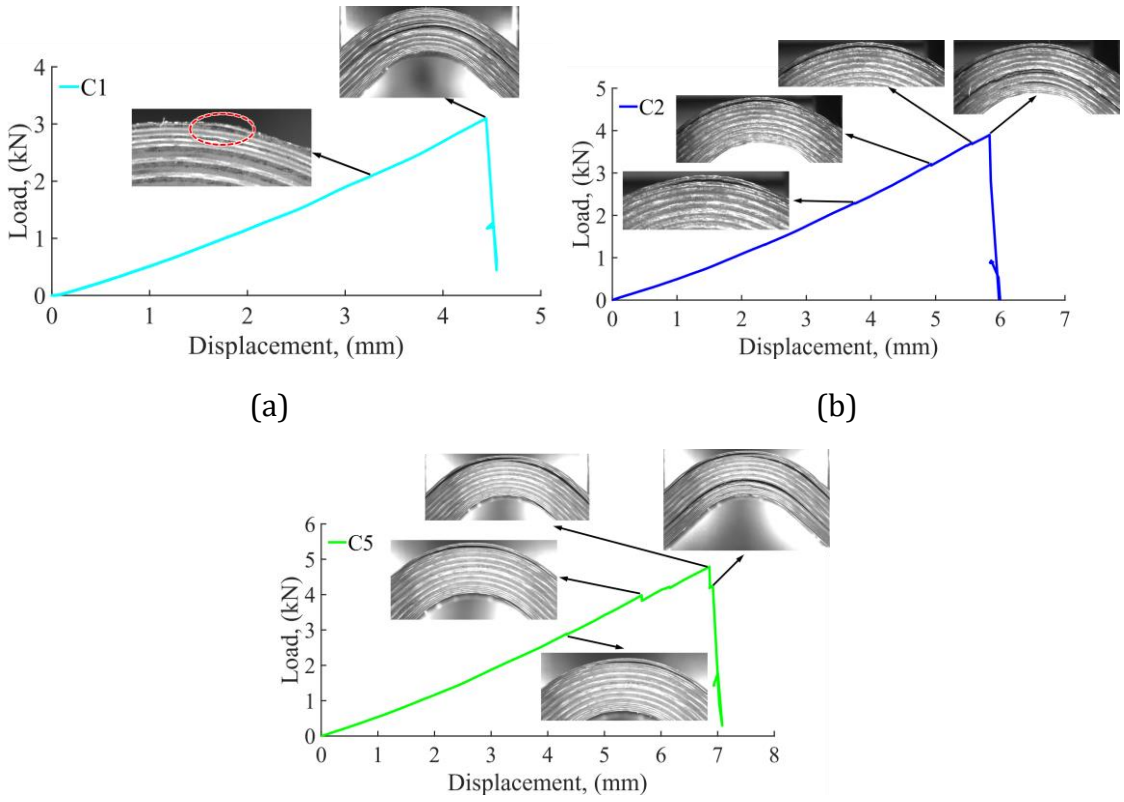

Figure 9.1: Failure mode of unpinned specimens.

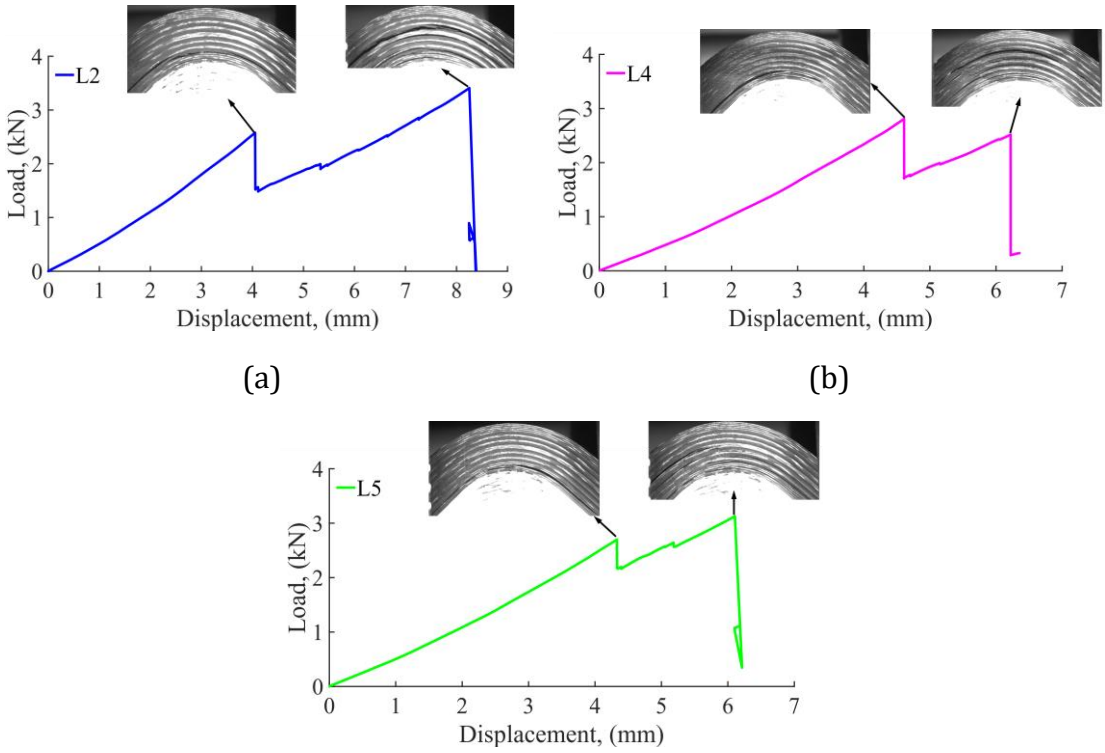

Figure 9.2: Failure mode of 0.27% carbon-fibre Z-pinned specimens.

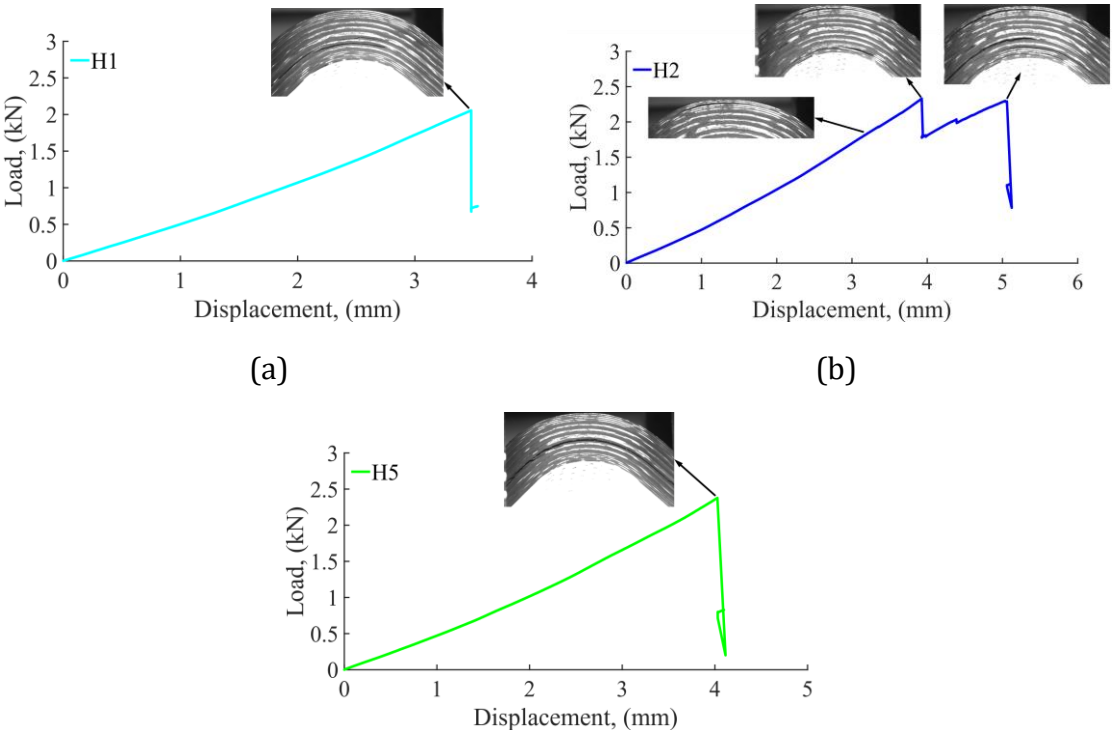

Figure 9.3: Failure mode of 0.54% carbon-fibre Z-pinned specimens.

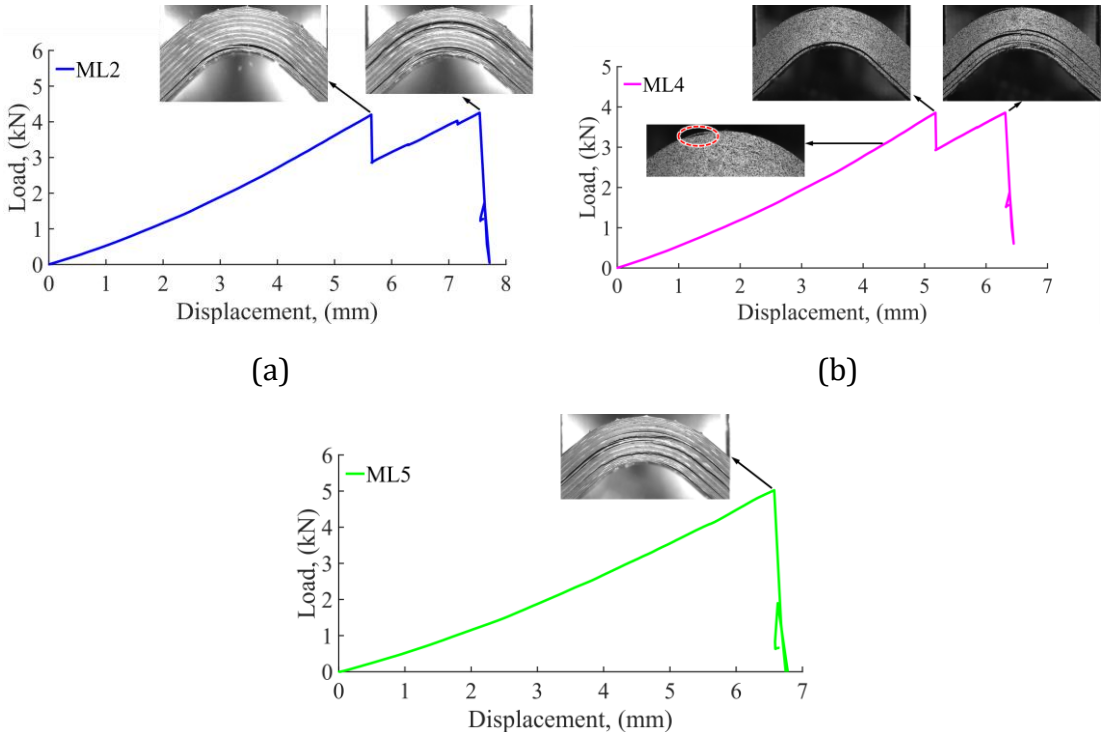

Figure 9.4: Failure mode of 0.27% metal Z-pinned specimens.

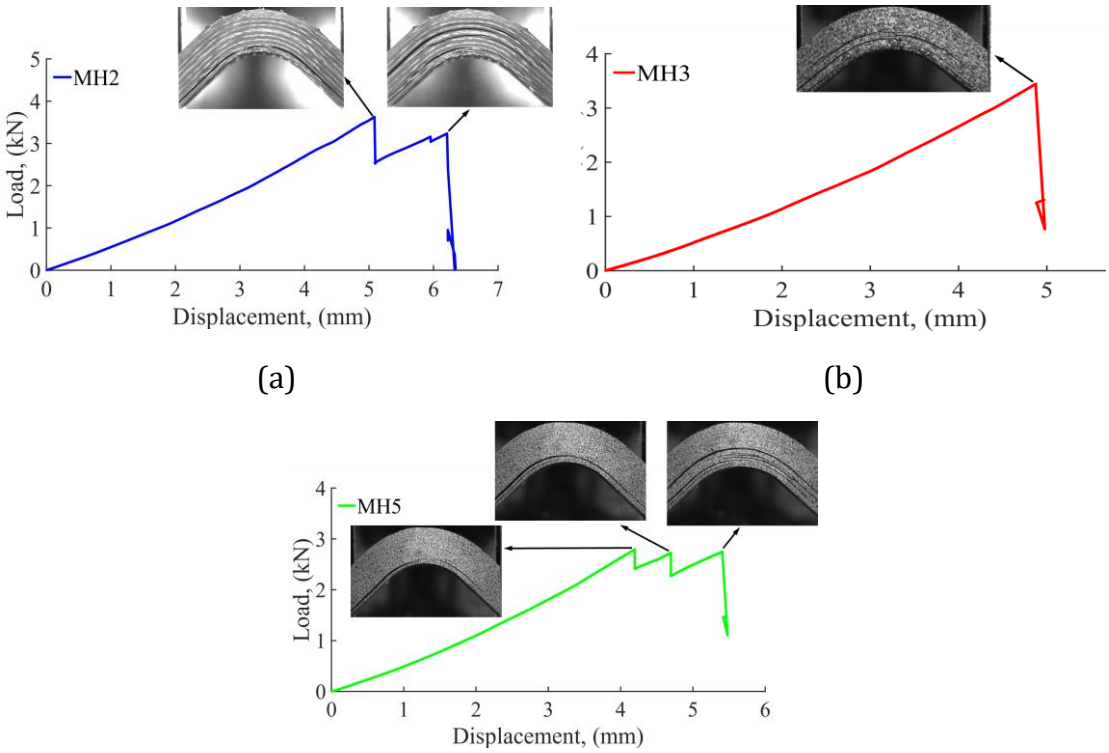

Figure 9.5: Failure mode of 0.54% metal Z-pinned specimens.

APPENDIX 2 SUPPLEMENTARY MATERIAL FOR CHAPTER 5

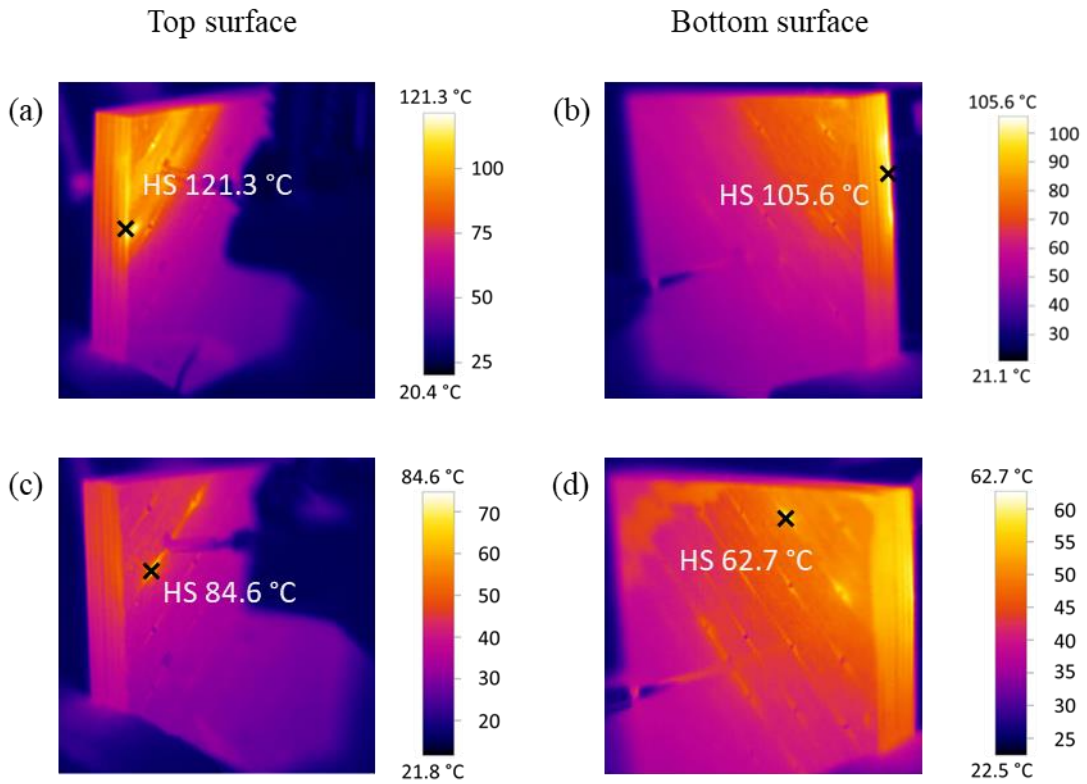

Figure 9.6: Through-thickness thermal images: (a, b) COP-L-0.25 A, (c, d) COP-H-0.25 A.

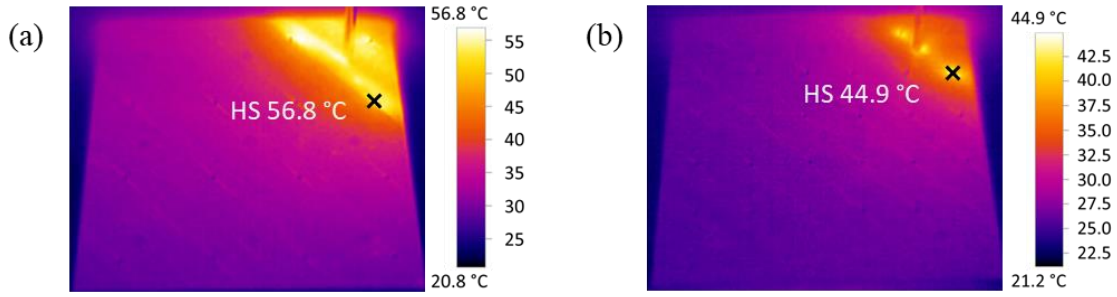

Figure 9.7: In-plane thermal images: (a) COP-L-0.2 A, (b) COP-H-0.2 A.

Table 9.1: Experimental results of the through-thickness resistance for individual samples.

	Resistance (Ω)								
Position	**1**	**2**	**3**	**4**	**5**	**6**	**7**	**8**	**9**
UP-1	2076	2083	2098	2084	2075	2083	2097	2083	2076
UP-2	973	975	1007	974	973	975	1012	973	973
UP-3	2230	2243	2290	2257	2227	2242	2321	2257	2229
AVE	**1760**	**1767**	**1798**	**1772**	**1758**	**1767**	**1810**	**1771**	**1759**
C.V. %	**39.0%**	**39.1%**	**38.5%**	**39.3%**	**38.9%**	**39.1%**	**38.7%**	**39.3%**	**39.0%**
COP-L-1	30.24	36.60	46.84	35.11	30.38	37.55	44.74	36.11	32.20
COP-L-2	36.77	43.46	56.06	36.73	35.65	43.33	58.33	39.36	36.55
COP-L-3	29.77	44.80	69.78	38.93	28.27	48.19	59.94	38.64	29.24
AVE	**32.26**	**41.62**	**57.56**	**36.92**	**31.43**	**43.02**	**54.34**	**38.04**	**32.66**
C.V. %	**12.1%**	**10.6%**	**20.1%**	**5.2%**	**12.1%**	**12.4%**	**15.4%**	**4.5%**	**11.3%**
COP-H-1	22.26	20.45	25.17	24.05	21.25	22.53	28.81	23.86	22.47
COP-H-2	24.33	24.58	36.68	31.71	23.85	29.50	34.67	25.75	26.15
COP-H-3	18.07	20.00	27.11	22.04	16.95	19.38	31.98	20.68	16.78
AVE	**21.55**	**21.68**	**29.65**	**25.93**	**20.68**	**23.80**	**31.82**	**23.43**	**21.80**
C.V. %	**14.8%**	**11.6%**	**20.8%**	**19.7%**	**16.8%**	**21.8%**	**9.2%**	**10.9%**	**21.7%**
CAR-L-1	28.11	30.99	42.89	30.97	27.51	30.47	49.90	30.90	28.32
CAR-L-2	18.61	21.78	26.73	22.92	17.97	21.48	32.51	22.83	20.53
CAR-L-3	22.50	26.33	38.11	26.32	21.76	26.76	37.68	25.10	21.43
AVE	**23.07**	**26.37**	**35.91**	**26.74**	**22.41**	**26.24**	**40.03**	**26.28**	**23.43**
C.V. %	**20.7%**	**17.5%**	**23.1%**	**15.1%**	**21.4%**	**17.2%**	**22.3%**	**15.8%**	**18.2%**
CAR-H-1	15.89	16.90	18.51	16.80	16.54	16.74	19.74	16.65	16.62
CAR-H-2	13.91	14.25	20.75	15.27	14.12	14.51	17.57	15.00	14.54
CAR-H-3	16.90	18.58	22.20	17.47	16.02	18.71	20.60	17.05	16.97
AVE	**15.57**	**16.58**	**20.49**	**16.51**	**15.56**	**16.65**	**19.30**	**16.23**	**16.04**
C.V. %	**9.8%**	**13.2%**	**9.1%**	**6.8%**	**8.2%**	**12.6%**	**8.1%**	**6.7%**	**8.2%**

Table 9.2: Experimental result of the in-plane resistance for individual samples.

	Resistance (Ω)								
Position	**1**	**2**	**3**	**4**	**5**	**6**	**7**	**8**	**9**
UP-1	3.43	2.17	2.67	20.94	2.98	1.58	36.91	20.97	4.10
UP-2	9.88	2.81	3.03	32.58	8.58	2.02	77.98	32.59	9.18
UP-3	13.32	4.16	3.99	47.87	11.53	2.23	113.67	47.87	11.91
AVE	**8.88**	**3.05**	**3.23**	**33.80**	**7.70**	**1.94**	**76.19**	**33.81**	**8.40**
C.V. %	**56.6%**	**33.3%**	**21.1%**	**40.0%**	**56.4%**	**17.1%**	**50.4%**	**39.9%**	**47.2%**
COP-L-1	4.55	3.55	3.04	9.92	4.68	2.95	19.58	11.62	7.22
COP-L-2	4.65	4.30	3.73	7.18	4.47	3.50	28.24	10.66	4.84
COP-L-3	8.84	6.37	2.54	16.81	4.54	5.05	36.57	16.53	4.91
AVE	**6.01**	**4.74**	**3.10**	**11.30**	**4.56**	**3.83**	**28.13**	**12.94**	**5.66**
C.V. %	**40.7%**	**30.8%**	**19.3%**	**43.9%**	**2.3%**	**28.4%**	**30.2%**	**24.3%**	**23.9%**
COP-H-1	4.69	2.45	2.78	8.82	4.52	3.17	12.42	9.24	4.22
COP-H-2	3.30	2.88	2.88	4.66	2.61	1.94	10.57	4.58	2.56
COP-H-3	4.94	3.41	3.93	9.09	3.49	2.26	19.10	7.63	2.82
AVE	**4.31**	**2.91**	**3.20**	**7.52**	**3.54**	**2.46**	**14.03**	**7.15**	**3.20**
C.V. %	**20.5%**	**16.5%**	**19.9%**	**33.0%**	**27.0%**	**26.0%**	**32.0%**	**33.1%**	**27.9%**
CAR-L-1	4.31	4.66	2.22	7.98	3.42	3.67	27.01	7.86	3.63
CAR-L-2	4.42	4.33	1.70	8.66	3.48	3.70	18.80	9.37	3.52
CAR-L-3	4.05	3.70	5.50	8.67	3.80	4.10	20.94	8.26	3.02
AVE	**4.26**	**4.23**	**3.14**	**8.44**	**3.57**	**3.82**	**22.25**	**8.50**	**3.39**
C.V. %	**4.5%**	**11.5%**	**65.6%**	**4.7%**	**5.7%**	**6.3%**	**19.1%**	**9.2%**	**9.6%**
CAR-H-1	3.71	2.60	2.09	4.30	3.42	1.93	7.65	4.57	2.93
CAR-H-2	2.42	2.06	1.94	4.43	2.46	1.75	6.83	4.06	2.89
CAR-H-3	3.68	2.93	2.94	4.41	2.41	2.38	7.51	4.00	2.97
AVE	**3.27**	**2.53**	**2.32**	**4.38**	**2.76**	**2.02**	**7.33**	**4.21**	**2.93**
C.V. %	**22.5%**	**17.4%**	**23.2%**	**1.6%**	**20.6%**	**16.1%**	**6.0%**	**7.4%**	**1.4%**

APPENDIX 3 SUPPLEMENTARY MATERIAL FOR CHAPTER 6

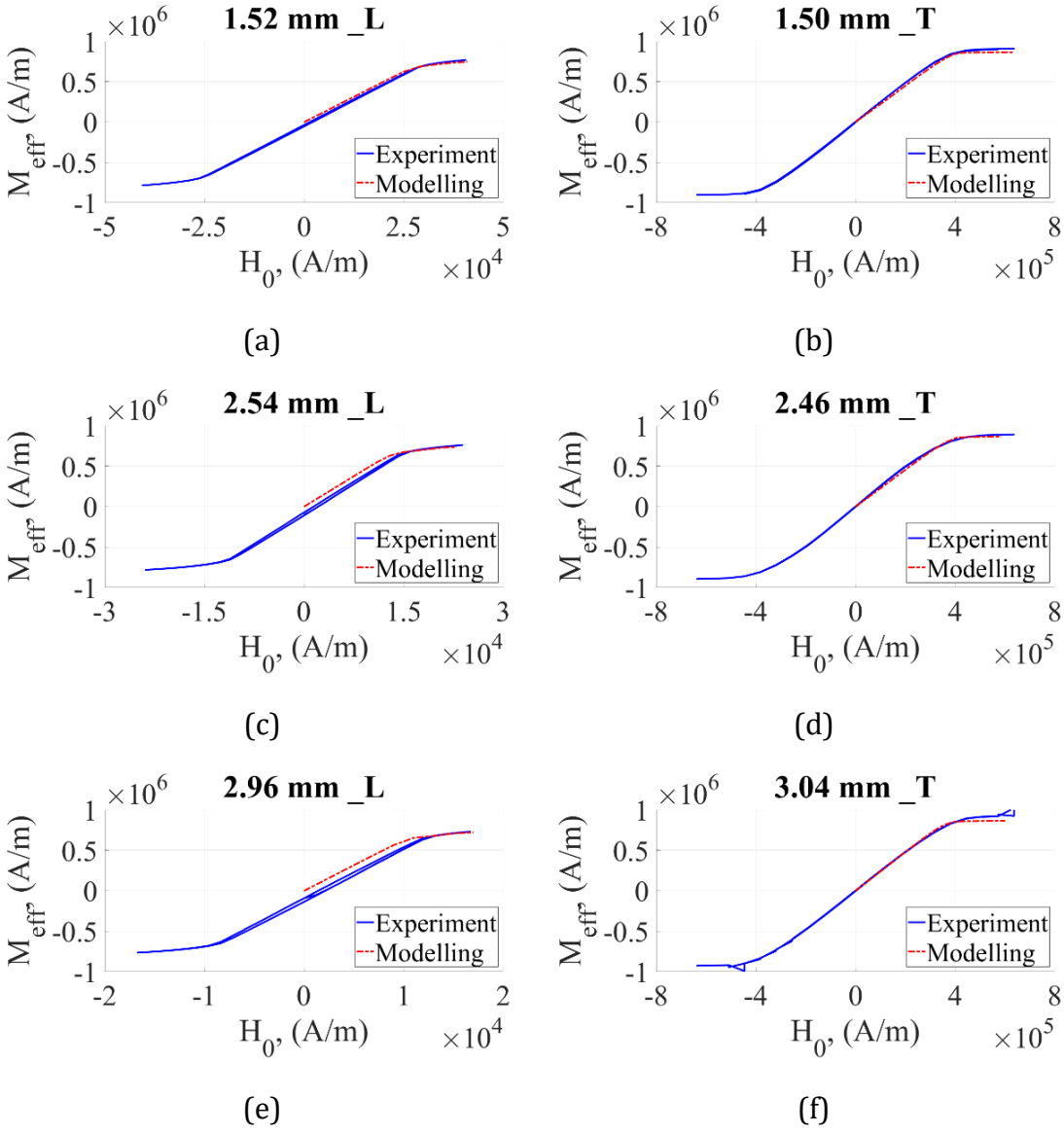

Figure 9.8: Comparison of experimental and modelling M-H curves of Ni/Fe pins with variable lengths (L: longitudinal, T: radial).

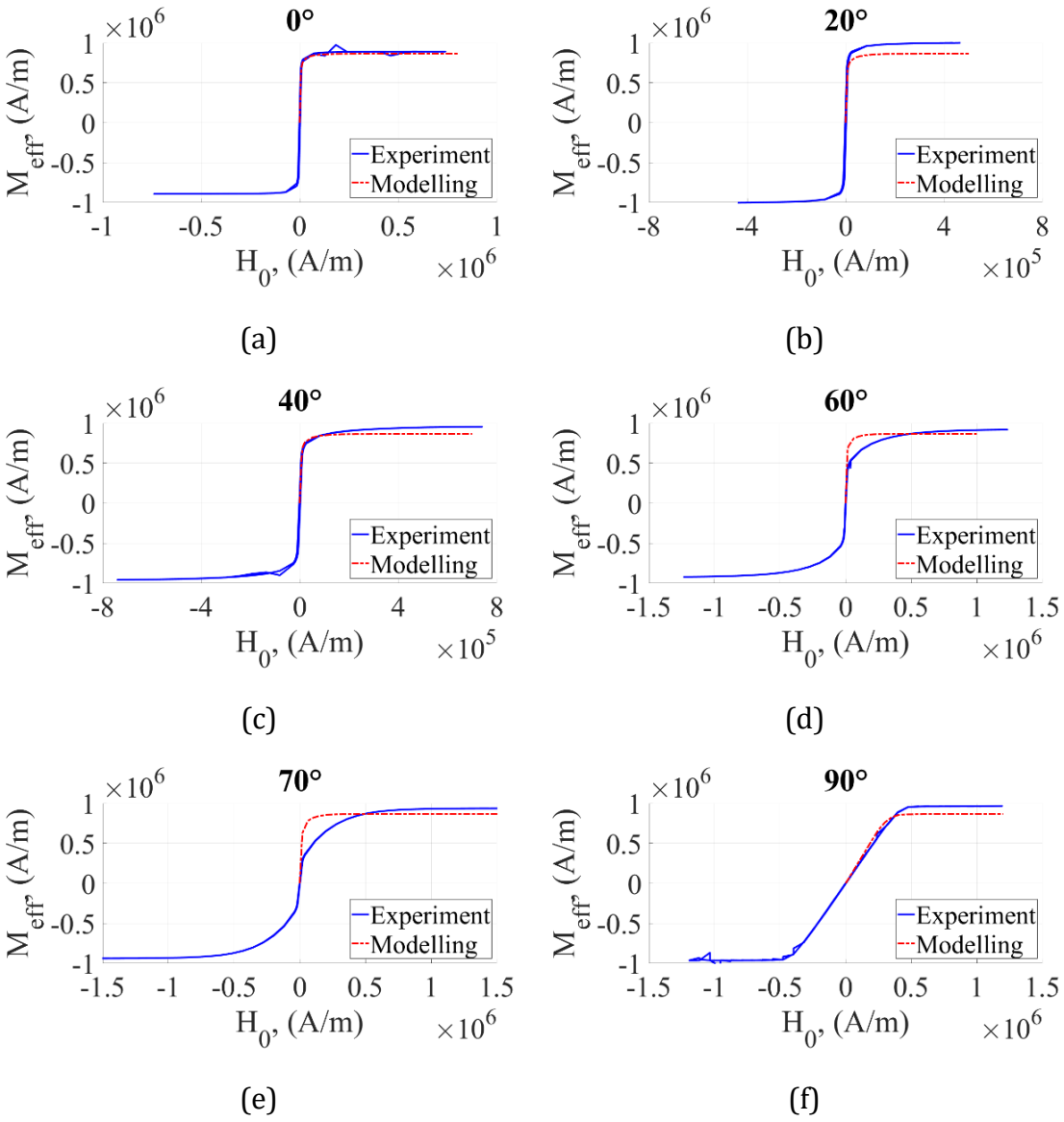

Figure 9.9: Comparison of experimental and modelling M-H curves of the single 4.05 mm long Ni/Fe alloy pin with variable inclination angles.

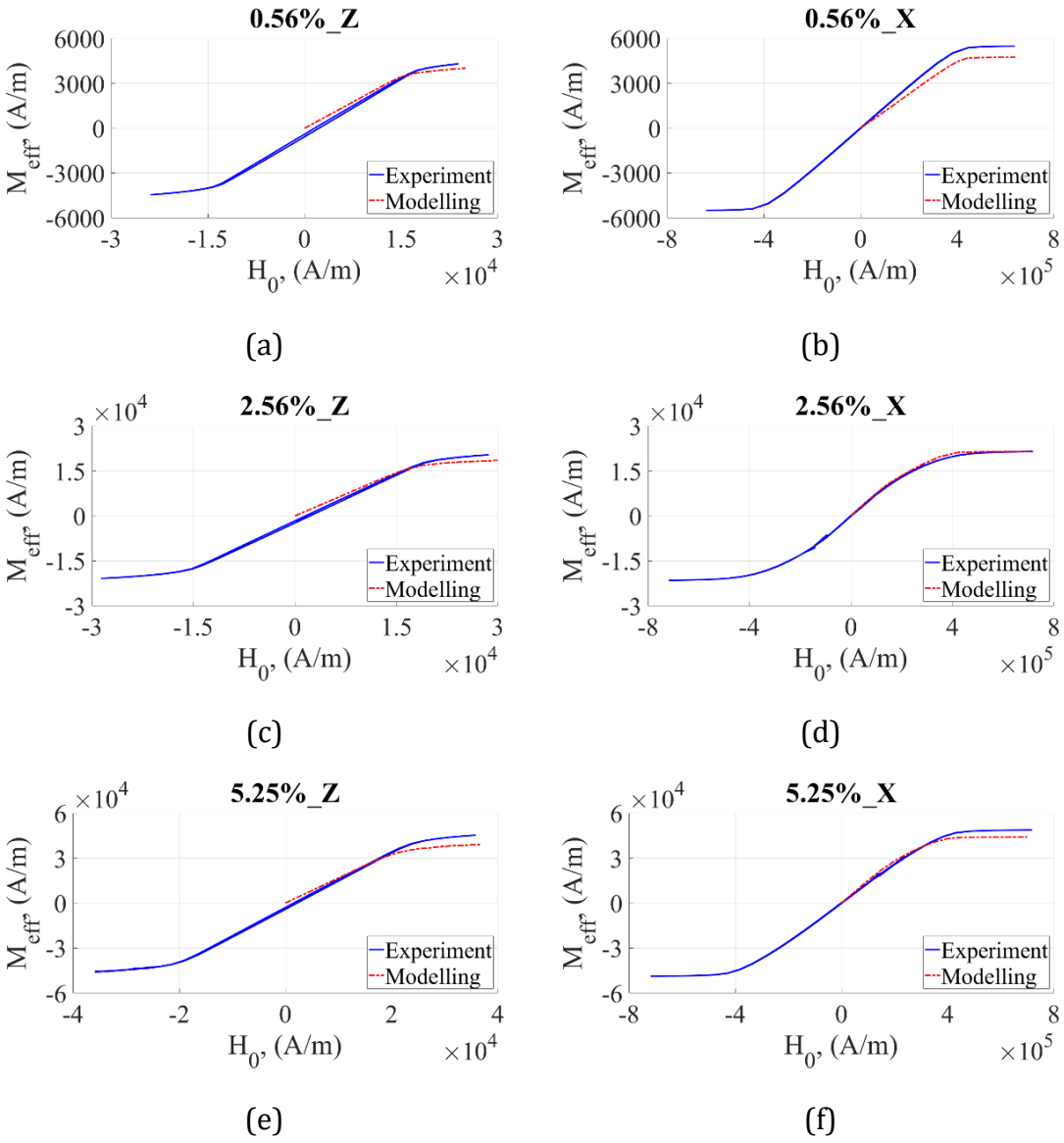

Figure 9.10: Comparison of experimental and modelling M-H curves of Ni/Fe pins reinforced laminate coupons (Z: out-of-plane, X: in-plane).